Dissertation

Relativistic freeze out studies and two-particle Correlations

Steffen Feld

Universität Bielefeld
Fakultät für Physik

supervised by
Prof. Dr. N. Borghini

November 15, 2018

Gedruckt auf alterungsbeständigem Papier ISO 9706

Abstract

In the research field of heavy-ion collisions there are a bunch of interesting questions to be answered. Here we address two of them.

The first is about the transition from a hydrodynamical modelling to a particle-based approach. This transition is a crucial element of the description of ultra-relativistic heavy-ion collisions. By employing kinetic theory within polar Milne coordinates and anisotropic hydrodynamical tools, we show that an anisotropic local phase-space distribution of the emitted particles can smooth such a transition. In addition we derive the so called anisotropy parameter from a kinetic description. We discuss how final state observables – within this new freeze out procedure – depend less on system's quantities at the freeze out surface.

Further we present a way how our procedure of the kinetic freeze out can be further improved, via incorporating the effect of interparticle interactions. Therefore we present the arising equations of motion which were obtained by the computation of the various moments.

The second question we are addressing is dealing with the investigation of two-particle distributions. We present studies which are essential for investigating the azimuthally dependent two-particle distributions. Therefore we continued the concept of one-particle azimuthally distributions to the case of two-particle observables. Afterward we present a model to incorporate the fluctuations of one-particle distributions, in order to not mix up the effect of one-particle fluctuations and two-particle correlations.

Contents

1 Heavy-Ion Collisions

Ultra relativistic heavy-ion collisions (HIC) are an interesting research subject by its own. The key motivation for studying this subject is to investigate matter in a state where the strong interaction is the dominant interaction for the system's dynamics. Whereas in our daily life gravitational and electromagnetic interactions are prevailing, although the strong and the weak force are at play in the background as well. Over the time there were written many reviews and even whole books about all the aspects of the research subject HIC. The introduction is mostly influenced by the books [1], [2] and the reviews [3], [4] and [5].

1.1. What are heavy-ion collisions

In principle the research of ultra relativistic heavy-ion collisions deals with the outcome of the collision of two very high energetic heavy-ions. In order to perform such an experiment fully ionized atoms like gold or lead are accelerated to very high energies and afterwards forced to collide, nowadays most often head on inside a detector. This detector records the resulting particles flowing out of the collision center. The label ultra relativistic refers to the fact that the ions are so highly accelerated, that their kinetic energy is much larger than the energy stored in their rest mass. A first arising characteristic physical parameter is of course the collision energy. In order to compare the collisions of different nuclei in a proper way the collision energies are characterized by $\sqrt{s_{NN}}$, which is the total collision energy of the pair of two nucleons[1] in the center of mass frame. Up to now there were experiments carried out with a $\sqrt{s_{NN}}$ up to 2.76 TeV, 5.02 TeV (Lead-Lead) and 5.44 TeV (Xenon-Xenon). Realizing that the nucleon's mass is of order 1 GeV, it is clear that an ultra relativistic approach is valid. Just to get an impression of the huge achieved energy scales, reference [5] points out that a collision energy $\sqrt{s_{NN}} = 2.76$ TeV corresponds to a $\gamma = 1400$, where γ is the Lorentz factor. Since this factor is so large, the spherical ions are highly contracted in the center of momentum frame – where the detector is working. Therefore often the ions are referred to have the shape of pancakes.

1.2. Why are heavy-ion collisions done

One of the initial key motivations for performing ultra relativistic heavy-ion collisions is to test nuclear matter under extreme conditions i.e. high temperatures and/or high densities.

[1] Located in two different nuclei.

In fact there is clear evidence that during heavy-ion collisions the hottest man made matter is created, whose temperature exceeds even the temperature in the core of our sun by a factor of more than 10^5 [4]. As a remark let us mention that in the above statement there is an assumption hidden. Namely that one identifies the hydrodynamised fields as thermodynamical fields. This assumption is currently under debate.

Under these conditions and the for the experiment relevant time scales, the strong force is maintaining the systems evolution. Explaining the strong force and the underlying quantum field gauge theory, called Quantum-Chromo-Dynamics (QCD), goes beyond the scope of this thesis. This is why here only some main features – which are essential for the HIC research – are very briefly discussed.

Within QCD one can compute the propagation and the probability of interaction between strong interacting particles. From a historical point of view the first step for a systematical investigation of the strong interaction was done by Gell-Mann in 1961 within a procedure called the eight-fold way. In this work all the – up to that time – known hadrons where systematically organized. Applying the mathematical framework of group theory Gell-Mann was able to reproduce the confusing high number of hadrons out of a comparable small number of partons. These partons, which were at that time just group theoretical objects were called quarks. It is assumed that they are the elementary matter particles undergoing strong interactions. The different quarks do have different flavors. At those times there were three different quark flavors known, from which one could build up the group theoretical $SU(3)_f$ flavor group. The known flavors at that time were named up, down and strange. Today it is known and measured that there exist also charm and bottom quarks which build up further hadrons. In addition the top quark is established as well, which results all in all in six flavors.

Since they reproduce the physical measured hadrons, quarks need to have a spin of $1/2$. Therefore they are fermions. Further since they are elementary these objects have to follow the rules of quantum mechanics. The existence of hadrons like the Ω^-, which is build up by three strange valence quarks and has a spin of $3/2$, indicates that quarks have to have an additional quantum number, since otherwise three half-spin objects would share the same quantum mechanical state, which is forbidden by the Pauli principle. This additional quantum number is the color, which is the charge of the QCD. While Quantum-Electro-Dynamics (QED) is generated by one electric charge, in QCD there are three color charge states. A charge neutral and non trivial state – comparable to an electron proton pair in the case of QED – can be built up in QCD by a triplet of three quarks carrying three different colors, which makes the resulting object colorless. Due to the strong interaction it is only possible to observe such colorless states in nature. Such a state of three coupled quarks is called baryon. The most 'prominent' baryons in daily life are the proton and the neutron, which build up the nuclei of atoms. But moreover there exist also anti-quarks, which carry an anti-color. This makes it possible to bound together a quark and an anti-quark in a colorless state. This states are the Meson states. The fact that in nature only colorless states are present is referred to confinement. At the end of the sixties, particle accelerators were able to reach such high energies, that within deep inelastic scattering on protons the mathematical objects became physically measured objects.

For the pioneering work of developing the QCD Gross, Politzer and Wilczek were awarded with the Nobel prize. The QCD describes as mentioned the interaction between quarks, which are the matter particles. Since it is a quantized gauge theory the interactions are transmitted by the strong interaction gauge bosons, the gluons. From a mathematical point of view the QCD is a non abelian gauge theory. This has the physical consequence that the

gluons, which transmit interactions between colored particles, carry color charges as well. Together with the fact that the coupling of the strong force can be very large, this comes along with a bunch of interesting physical consequences.

One consequence and also a key motivation for performing ultra relativistic heavy-ion collisions, is the running coupling of the QCD denoted by α_s. In fact this QCD coupling depends on the energy scale Q at which QCD is tested. Figure 1.1 shows a collection of measurements of the coupling α_s extracted from different experiments, testing different energy scales Q.

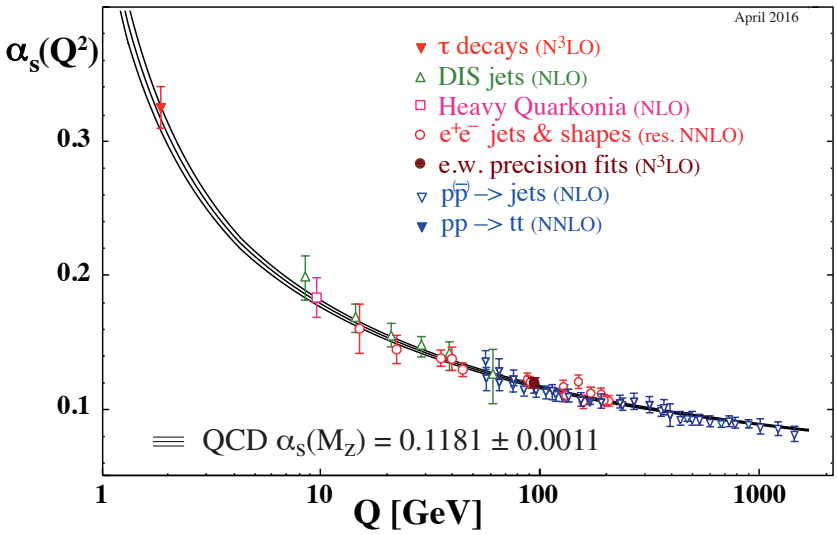

Figure 1.1.: Summary of running coupling measurements plotted over a logarithmic energy scale Q axis. Taken from [6].

As one can see, this coupling is very large for small energy scales. In this regime the quarks are confined. But with increasing energy scale the coupling constant decreases, one can imagine that quarks are asymptotically ($Q \to \infty$) free. Precisely this asymptotic behavior impelled scientists to create systems with very high energy densities in order to investigate the small α_s regime of QCD. One experimental way to investigate such systems of nearly liberated quarks and gluons is the heavy-ion collision.

The basic idea behind the experiment is that due to the high collision energies one creates a hot and dense system right after the collision in which the quarks and gluons can move nearly freely. This system is called Quark Gluon Plasma (QGP).

1.3. What is seen in such experiments

One characteristic and challenging feature of heavy-ion collisions is that scientists are only able to get information about the ions before they are accelerated, about their collision energy and about particles that reach the detector long time[2] after the collision. However in the field of heavy-ion research scientists were very active in extracting various information out of the particle spectrum in order to build models for the different theoretical stages of the evolution

[2] in terms of QCD time scales

of the system, which is called fireball as well. In the following we will shortly present the current state of the understanding of the fireball's evolution, with all the established stages.

Figure 1.2 shows the established spacetime diagram, including the main stages the system runs through during an ultra relativistic heavy-ion collision.

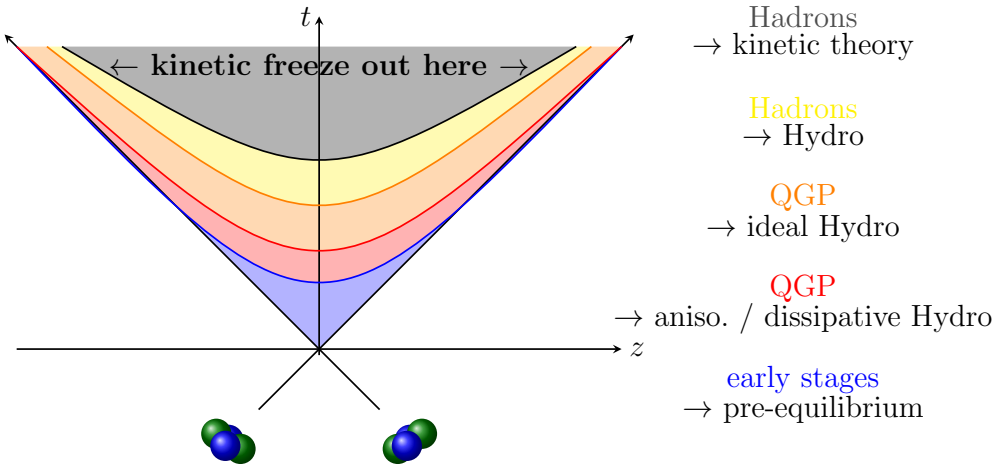

Figure 1.2.: Spacetime diagram of a central element in an ultra relativistic heavy-ion collision in its local rest frame. The lines indicate surfaces of constant proper time.

Starting from the bottom of figure 1.2 and following the time axis the collision process begins with two highly Lorentz contracted nuclei approaching each other. After they traversed each other a high amount of entropy is produced. In fact at this stage most of the fireball's entropy is produced right after the collision. The produced entropy is highly related to the number of particles in the very end of the collision process. Since in the experiment one can not adjust the impact parameter at which the nuclei collide – and therefore the overlap size – in different collisions there is a different amount of total entropy produced, which in turn results in different numbers of produced particles. The participants, which are nucleons that undergo at least one collision with another nucleon, lose in the LHC setup about 85 % of their energy. During the first[3] 1 fm$\approx 10^{-23}$ s this deposited energy and quantum numbers are following the pre-equilibrium evolution in such a way, that afterwards a hydrodynamical description is applicable.

At the end of the blue shaded area in figure 1.2 the system is hydrodynamized, which means that all the gradients are smooth enough in order to apply either anisotropic hydrodynamics, dissipative hydrodynamics or viscous anisotropic hydrodynamics. These hydrodynamical tools will be introduced and discussed in section 2.6. During the hydrodynamical expansion the gradients will be furthermore smoothed out in such a way that the system asymptotically approaches the ideal hydrodynamical stage. At least at this time the system is thought to be thermalized. Due to this fact heavy-ion collisions are said to test the thermodynamical phase diagram of QCD at relatively small baryon chemical potential. This phase, where color charged degrees of freedom are evolving in a collective expansion, is called Quark Gluon Plasma. Throughout the system's expansion, while all the relevant quantum numbers are preserved, it has to dilute further. At a temperature of around 156 MeV [7] lattice computations for a static equilibrium QCD system indicate a cross over, where the hadronization of the deconfined medium takes place. From this point on the effective degrees of freedom

[3] As the keen reader notices, we will use the natural units in which $c = \hbar = k_B = 1$ throughout this thesis.

are color neutral charged. In a local rest frame the lifetime of the QGP is roughly about 10 fm in modern facilities.

In the theoretical description of the ongoing expansion the system cools down to a temperature region where the particle yields freeze out. This region is called the chemical freeze out. Later on the particle' s momenta freeze out as well, which results in a free streaming of the hadrons after the kinetic freeze out. From now on the hadrons are assumed to fly freely towards the detector. To model the process of kinetic freeze out in a better way than it is usually done, is the subject of chapter 2. Therefore the physical models will be discussed in detail in that chapter. The typical duration of the nontrivial evolution lasts about 100 fm in a local rest frame.

Please note that labels like cross over temperature or chemical freeze out temperature have to be taken with a huge grain of salt, since first the fireball's expansion is highly non static and secondly the processes do not take place at a sharp temperature but is lasting over a temperature intervall. Further the freeze out processes, especially the chemical ones, depend on the particle species. In addition the chemical freeze out will cause non equilibriumness in the corresponding chemical potentials. There are also coming up approaches to describe several observables of heavy-ion collisions without the assumption that the system reaches an equilibrium state at all, but stays "far from equilibrium". A review can be found in [8].

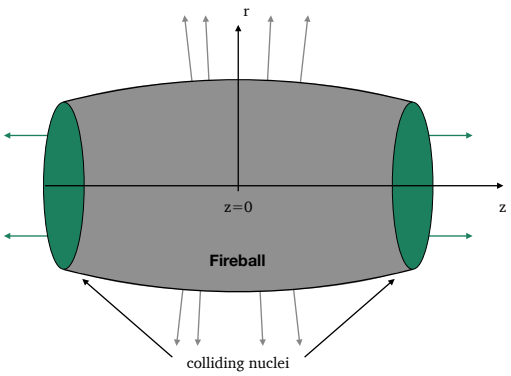

Figure 1.3.: Cartoon of the system's expansion symmetry in the lab frame's position space.

Figure 1.3 shows the geometry of the fireball's expansion in the lab frame's position space. Since initially the nuclei are flying through each other, the medium has a symmetry around the collision point $z = \eta = 0$. Further, since the highly Lorentz contracted nuclei have no real longitudinal structure, the resulting medium is assumed to have no nontrivial structure with respect to the beam line as well. Therefore the system can be modeled via a one dimensional Hubble flow in beam direction, which is called two dimensional Bjorken flow [9], since it relates the time component and the longitudinal direction by the following ansatz.

$$v_z = \frac{z}{t} \tag{1.3.1}$$

Basically the medium is thought to move freely along the beam axis in a boost invariant

manner. As a remark let us mention that in this epoch not the particles are moving freely, but the fluid cells are assumed to move without further interaction along the beam line. How this flow profile is mathematical implemented is discussed in detail in section 2.2. One important remark is that around the point $z = 0$ the flow profile is approximately invariant under shifts in z.

In the plane transverse to the beam line the system is almond shaped. The exact form depends of course on the impact parameter. Figure 1.3 is a sketch of the polar Milne position space geometry of the created fireball. Note that in chapter 2.9.3 we will discuss the transverse plane and its influence on observables in detail.

In contrast to the medium's expansion, often the evolution of partons is investigated, which originate from an initial hard nucleon-nucleon scattering process. The outcome of such a process can be very massive particles like quarkonia, or very high momentum partons, which are by themselves the origin of medium traversing jets. The symmetry of such events does not exhibit the above discussed characteristics.

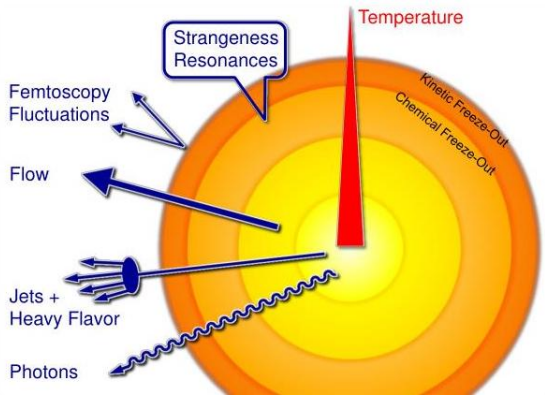

Figure 1.4.: Cartoon of the origin of some HIC observables. Taken from [10].

Of course the above sketch of the heavy-ion collision process is based on several observables. Figure 1.4 illustrates roughly the origin of the most important observables, which we will discuss in the following, starting from the center. The already mentioned jets, which are produced at the very beginning of the collision and afterward traversing the medium are color charged. Due to their path through the entire expansion, they give rise to a time integrated information about the medium. The same holds for heavy flavor partons. Since the quarks carry an electric charge as well, over the entire lifetime of the fireball there are photons produced either from the partons, or from the hadrons. Therefore in the photon spectrum there is much information about the fireball encoded. However it is experimental very challenging to detect these photons.

One of the most interesting observables for the studies done in the following is the flow. Therefore this observable is discussed in one of the following chapters 2.9.3 in detail. In principle a non vanishing anisotropic flow v_n can be a signature of interactions between the effective degrees of freedom in the collective phase. In chapter 4 the concept of this observable will be further developed.

The last main observable is governed by the femtoscopy. One is able to measure the size of the kinetic freeze out volume with this observable.

1.4. Where are heavy-ion collisions performed

At the moment there are two acceleration facilities, which frequently inject heavy-ions in order to perform ultra relativistic heavy-ion collisions.

- The RHIC (Relativistic Heavy Ion Collider) is operating since the year 2000. Most often the injected ions are gold, but there where also measurements with several other ions as well, like uranium or copper. It is located at the Brookhaven National Laboratory (BNL) in New York. Around the 3.8 km large circular accelerator, which is able to accelerate gold ions up to $\sqrt{s_{NN}} = 200$ GeV, there are right now two operating experiments/detectors. One is PHENIX (Pioneering High Energy Nuclear Interactions eXperiment) and the other one is STAR (Solenoidal Tracker At RHIC). Nowadays RHIC concentrates on the Beam Energy Scan (BES) I and BES II, where collisions at lower energies are performed in order to feed in baryons from the ions, which could result in a higher baryon chemical potential of the system.

- The LHC (Large Hadron Collider) is the most powerful accelerator. It is operating since 2010 on the border between France and Switzerland, near Geneva. Mainly it is concentrating on particle physics, i.e. search for "new" particles and measuring parameters of the standard model to highest precision. However frequently lead ions (Pb) are injected into the 27 km long circular accelerator in order to perform collisions at energies up to $\sqrt{s_{NN}} = 5.02$ TeV. Around the LHC there are four experiments, which are investigating several aspects of the QGP. The experiments are ATLAS (A Toroidal LHC ApparatuS), ALICE (A Large Ion Collider Experiment), which is by design in both detector and employees a designated heavy-ion experiment, CMS (Compact-Muon-Solenoid-Experiment) and LHCb (Large Hadron Collider beauty). Due to the fact that in this collider one can collide ions on ions (A + A collisions) as well as lead on proton (p + A collision) and proton on proton (p + p collision) at the same energies, one can study in detail whether an A + A collision is "more" than just a bunch of p + p collisions.

  For the completeness it has to be mentioned that there are further facilities constructed or planned right now. Here are two of these projects, which are expected to influence the future heavy-ion collision research field.

- At GSI Helmholtzzentrum für Schwerionenforschung in Darmstadt the construction of FAIR (Facility for Antiproton and Ion Research) is running. At this experiment, which will also deal with nuclear physics, it will be possible to work in a region with a high net baryon number in the system. This baryon numbers will be even higher than the achieved density in the BES II program.

- There is a project in the USA planned, which is called EIC (Electron Ion Collider). As indicated by the name it is planned to collide point-like electrons with protons or ions. With this experiment people want to investigate the initial shape and the structure of protons and nuclei. Up to today it is not clear whether this experiment will be built at BNL, where already an ion and proton accelerator exists, or at the Jefferson Labs in Virginia, where an electron accelerator is operating.

1.5. What are the recent questions

In September 2012 scientists performed collisions of lead ions and protons at LHC. After analyzing the gathered data of this collisions 2014 people realized that although the system is small, several observables indicate a signal which is believed to reflect collective behavior. Against this background some scientists looked at the even smaller colliding system of two protons for "collectivity signals". They found that in an extremely tiny fraction of p-p collisions – namely highest multiplicity events – some signals could indicate a collective behavior as well. Since then people are more interested in the theories, which they before just used as tools. Two typical questions are how small must a system be in order to be not describable by hydrodynamics or does a working hydrodynamical description imply thermodynamical equilibrium.

These and several more questions are investigated in the field of collectivity in small systems. The observable and the corresponding studies presented in chapter 4 can hopefully at some point contribute to further systematical investigations of the small systems. In addition the in chapter 2 elaborated free streaming – which can be understood to be the opposite of collective behavior – solution can be used to perform studies which sets a lower bound. In such studies, which are currently performed by our group it is investigated how much interactions are needed in order to create signals which are understood to indicate collectivity. The presented studies in chapter 3 can be used to "turn on" a small number of interactions.

A second upcoming field is the study of systems with non vanishing chemical potential. Creating such systems is the aim of the above mentioned beam energy scan at RHIC. In order to describe the transport in such systems properly one needs to establish hydrodynamical theories including baryon sources.

The crucial question which was motivating the studies presented in chapter 2 and 3 is, how can the transitions between the different above sketched and well established stages of a heavy-ion collision be improved in order to achieve a smooth overlap of the different jigsaw pieces.

2 Relativistic Boltzmann equation in polar Milne coordinates for modeling kinetic freeze out

2.1. Motivation

In chapter 2 we will present the investigations we did on the search for a smoother kinetic freeze out procedure for the description of heavy-ion collisions. Basically we started this studies already during my Masters project. In the first publication [11] we examined the question if anisotropic hydrodynamics (see [12] and [13] for a very detailed derivation of the formalism) can be able to smoothen the transition between a fluid and particles.

At that time the anisotropic hydrodynamic formalism was just established by two groups [14], [12]. Figure 2.1 shows their main physical motivation. In the heavy-ion community's "traditional picture" it was/is assumed, that the hydro-stage starts at the latest after a proper time of about 1 fm/c. As we can see in the sketch at τ_{hydro} there still exists a huge pressure anisotropy, which means that the longitudinal[1] pressure is much smaller than the transverse pressure. This is due to the fact that the colliding nucleons travel along the z-axis with almost the speed of light away from the collision region. To start viscous hydrodynamics, which is an expansion around an isotropic equilibrium state is a too drastic assumption on the system. Therefore they treat the longitudinal pressure and the transverse pressure as two different quantities, which eventually will converge. Actually the group of Michael Strickland has built up a code from that idea, within which many observables measured in the experiment are reproduced [15].

The implementation of the kinetic freeze out is necessary, because as the medium created after the nucleons collision expands in spacetime, while all its quantum-numbers which are relevant on that time scales are conserved, it has to dilute. The hydrodynamical description of the fireball works well, if the effective degrees of freedom are interacting very often, so that they can achieve a local equilibrium state. A well established quantity measuring the interaction strength is the Knudsen number Kn. This is defined as the ratio of the mean free path (l_{mfp}) and a typical length scale L, which is the relevant scale where the description shall work, i.e. $Kn = {}^{l_{mfp}}/_{L}$. Here the l_{mfp} can be understood as two particle's average distance in the system. As the l_{mfp} increases, due to the system dilution, the effective degrees will undergo fewer interactions. So the application of hydrodynamics becomes at some point improper, since the small number of microscopical collisions is not able to keep the system in local equilibrium. Let us emphasize that the Knudsen number is a transport

[1] Pressure pointing along the beam axis, which is traditionally chosen to be the z-axis.

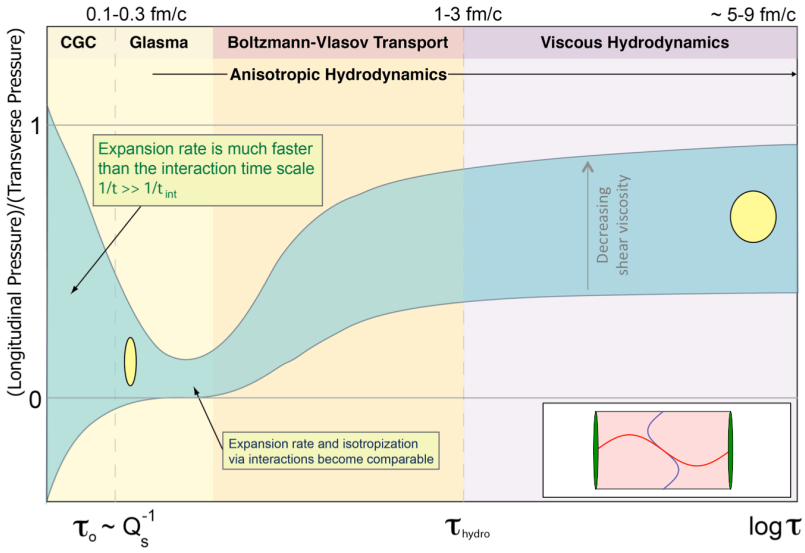

Figure 2.1.: Cartoon that shows the evolution of the pressure anisotropy as a function of τ in a LHC heavy-ion collision scenario. The blue shaded area represents the path of different initializations of the system. As one can see at the starting time of hydrodynamics τ_{hydro} the system is still not isotropic, since the ratio of the pressures is not equal to one. Picture taken from [13].

theoretical number, strictly speaking it is no hydrodynamical quantity. However sometimes people refer to the Knudsen number while working in a hydrodynamical framework. What is meant by such a statement is that the underlying kinetic system has a proper – which means small – Knudsen number in order to perform hydrodynamics.

At the very end of a heavy-ion collision particles are detected by a detector, which is $\approx 10^{14}$ times larger than the initial system size. It is clear that the detected particles can not interact with themselves any more, since they are that much diluted. In this high Kn-regime there exists a proper description as well, which is kinetic theory. In the limit of no interactions it is often called free streaming. Therefore physicists who want to describe the evolution of the medium have to switch their tools during the expansion. This is done via the Cooper-Frye freeze out formula [16]. The basic idea is that the medium description changes suddenly from a fluid-dynamical to a kinetic one as the medium is passing through a hypersurface Σ. From this point on, the particles decouple from the fluid and, assuming the emitted particles are then free, their momenta are frozen. The hypersurface Σ has to be a closed three-dimensional surface in spacetime in order to eventually transform the whole fluid.

This transition seems – not only to us – as a crucial point in the description of the fireball created in a heavy-ion collision. For the appropriate application of the Cooper Frye formula one needs to specify what is the criterion of switching from hydrodynamics to kinetic theory. In other words one needs first to pin down a special dynamical quantity like Kn, temperature, energy density, particle density or proper time and second one needs to specify a critical value for the chosen parameter, which I will label as freeze out parameter from now on. This has to be done in order to define Σ, which is just the surface made out of the points where the hydrodynamical fields reach the critical value. The main motivation to improve this freeze out formalism is the fact that computed final state observables depend on the initially chosen freeze out parameter. Since this parameter is not associated with a phase transition, there

is no reason why a final state observable should depend on the point where a theoretical physicist did change her/his "tool " to describe the medium. Accordingly, one should rather expect that nature performs a smooth transition between the two asymptotic models valid at small or large Knudsen numbers Kn.

However in the mentioned publication we showed that one is able to almost suppress completely the dependence of physical final state observables on the freeze out parameter, by dealing with anisotropic hydrodynamics [11], [17]. One of the innovative aspects of this work was, that we used an anisotropy pointing along the radial direction, in which the particles will fly freely after kinetic freeze out. As mentioned above, up to that time people used anisotropic hydrodynamics only with the anisotropy displaying the global, longitudinal direction. Whereas our direction of anisotropy is locally changing, since the radial direction points in different directions at different regions in the fireball. But while doing so, we had to introduce an anisotropy parameter ξ, which was up to that point a free parameter, which adjusts our degree of local anisotropy.

In the present study we searched for a physical interpretation of the anisotropy parameter ξ. To fill this object with a physical meaning we looked at the freeze out process "from the outside". Which means that we approach the transition from the kinetic regime. In other words we approached the kinetic freeze out "backwards" in order to justify the anisotropy parameter ξ in the hydro stage, via the later free streaming stage.

This chapter 2 is organized as follows: In section 2.3.1 we will present how one translates the geometry of the assumed Bjorken flow into Christoffel symbols, which are needed for the derivatives of the Boltzmann equation. Subsequent we present shortly how the integration measure is affected by the geometry. In the following section 2.4.1 we present the Boltzmann equation with respect to the Milne coordinates. This equation is important for the whole part 2. Afterwards in section 2.4.5 we will show, how this equation acts on the Jüttner distribution, which is the relativistic equivalent to the classical Maxwell-Boltzmann distribution.

2.2. Geometry

As a first step for describing transport phenomena in heavy-ion collisions we have to incorporate the geometry of the system and introduce proper variables. To realize the latter it will be very helpful to work with expressions for the velocity which are additive. It is clear that in special relativity's high energy regime the usual velocities are not additive since one needs to multiply them by a γ-factor. Due to the fact that we want to describe a medium which is created by two ultra relativistic nucleons we have to work with the rapidity instead of the classical velocity. It is common to chose the direction of the nucleon beams as z- or longitudinal axis[2]. The (longitudinal) rapidity y in momentum space is defined as follows.

$$y = \frac{1}{2} \ln \left(\frac{E + p_z}{E - p_z} \right) \tag{2.2.1}$$

In the above definition p_z is denoting the longitudinal momentum and E the relativistic energy which contains also the rest mass. Using this definition one can easily build the following expression.

[2] As it is also done in Figure 1.3.

$$\cosh(y) = \frac{e^y + e^{-y}}{2} = \frac{E}{\sqrt{E^2 - p_z^2}} \tag{2.2.2}$$

Taking the advantage of the transverse mass' definition $m_t^2 = m^2 + \vec{p_t}^2$, where $\vec{p}_t$ denotes the momentum in the plane transverse to the beam axis, we are able to reformulate the energy in dependence of the rapidity y.

$$E = m_t \cosh(y) \tag{2.2.3}$$

In the same way one can construct $\sinh(y)$. This gives an expression for the longitudinal momentum.

$$p_z = m_t \sinh(y) \tag{2.2.4}$$

While introducing polar coordinates in the transverse plane, we are able to formulate the momentum 4-vector.

$$p' = \begin{pmatrix} E \\ p_x \\ p_y \\ p_z \end{pmatrix} = \begin{pmatrix} m_t \ \cosh(y) \\ p_t \ \cos(\Phi) \\ p_t \ \sin(\Phi) \\ m_t \ \sinh(y) \end{pmatrix} \tag{2.2.5}$$

Here p_t denotes the modulus of the momentum pointing in the transverse plane. However in experiments it is hard to measure the particle's energy and the momentum at once. Therefore it is common to use the concept of the pseudorapidity η which is defined in the next expression.

$$\eta = \frac{1}{2} \ \ln\left(\frac{|\vec{p}| + p_z}{|\vec{p}| - p_z}\right) = -\ln\left(\tan\left(\frac{\theta}{2}\right)\right) \tag{2.2.6}$$

In this formula θ is denoting the angle between the emitted particle and the beam axis. Figure 2.2 shows a sketch of the geometrical meaning of the quantities introduced in equation (2.2.6). Similar to the above mentioned procedure one can deduce the subsequent two expressions.

$$|\vec{p}| = p_t \ \cosh(\eta) \tag{2.2.7}$$

$$p_z = p_t \ \sinh(\eta) \tag{2.2.8}$$

Note that one can relate the two momentum variables y and η to each other. This is for example done in [1]. For the particle spectra[3] in the midrapidity region the following statement holds.

[3] Number of particles per momentum bin.

$$\left.\frac{dN}{d\eta\ d^2p_t}\right|_{\eta=0} = \frac{p_t}{m_t}\left.\frac{dN}{dy\ d^2p_t}\right|_{y=0} \tag{2.2.9}$$

Now we have established all variables describing the momentum space, but since we want to describe transport of matter we have to deal with the position space as well. Based on the above calculation it is common to introduce a rapidity like variable in the position space as well. This variable is called spatial rapidity η_s.

$$\eta_s = \frac{1}{2}\ln\left(\frac{t+z}{t-z}\right) \tag{2.2.10}$$

Again one can extract from formula (2.2.10) expressions for the t- and the z-component of the position space by building $\cosh(\eta_s)$ and $\sinh(\eta_s)$. In addition we want to implement a circular symmetry in the transverse plane. All in all we get for the position space 4-vector the following formula.

$$x' = \begin{pmatrix} t \\ x \\ y \\ z \end{pmatrix} = \begin{pmatrix} \tau\ \cosh(\eta_s) \\ r\ \cos(\phi) \\ r\ \sin(\phi) \\ \tau\ \sinh(\eta_s) \end{pmatrix} \tag{2.2.11}$$

The angle ϕ is denoting the polar angle in the x-y-plane and r is the modulus of the transverse vector. In addition one needs to remember that in one-dimensional expansion the proper time follows the subsequent dependence.

$$\tau = \sqrt{t^2 - z^2} \tag{2.2.12}$$

All in all the relevant variables in the position space are therefore

$$\tau, \eta_s, r, \phi \tag{2.2.13}$$

We shall refer to these set as polar Milne coordinates. From now on the Greek indices, as μ or ν denote the components of the 4-vector in polar Milne curved space i.e.

$$\mu \in \{\tau, \eta_s, r, \phi\} \tag{2.2.14}$$

Furthermore we will denote 4-vectors in this curved basis without the prime. In general we indicate the partial derivation as follows.

$$\partial_\mu := \frac{\partial}{\partial x^\mu} \tag{2.2.15}$$

For the unit vectors in momentum space which are associated with the curved position space basis, one needs to employ the following formula.

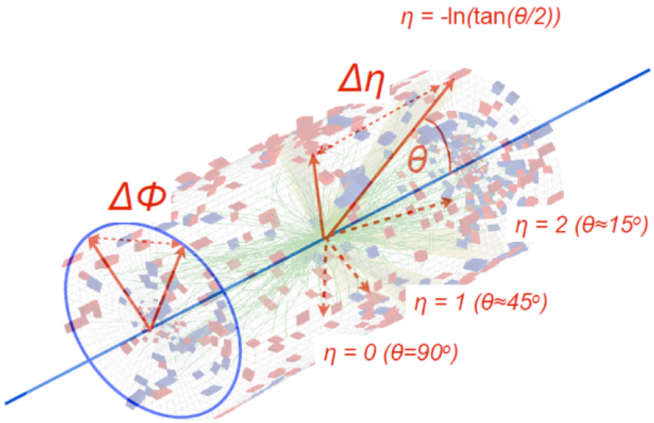

Figure 2.2.: Sketch which shows the meaning of the pseudorapidity η and the angle θ. Taken from [18].

$$p'^{\mu} = \frac{\partial x'^{\mu}}{\partial x^{\nu}} p^{\nu} \tag{2.2.16}$$

Inserting the appropriate vectors, one can relate the components of the momentum vector to the spacetime components in the following manner.

$$p^{r} = p_t \cos(\Phi - \phi) \tag{2.2.17}$$
$$p^{\phi} = \frac{p_t}{r} \sin(\Phi - \phi) \tag{2.2.18}$$
$$p^{\eta_s} = \frac{m_t}{\tau} \sinh(y - \eta_s) \tag{2.2.19}$$
$$p^{\tau} = m_t \cosh(y - \eta_s) \tag{2.2.20}$$

where the momentum space variables, as mentioned before are:

$$m_t, y, p_t, \Phi \tag{2.2.21}$$

Note that we choose the "offset" of the two polar angles origin ϕ and Φ to be zero. So we can forget about the ϕ-expression in the cos, respective sin-term.

For the case of massless particles one can simplify further.

$$m_t = \sqrt{m^2 + p_t^2} = p_t \tag{2.2.22}$$

Please note that we will often work just in two dimensions in position and momentum space. This is due to the fact that for ultra relativistic heavy-ion collisions the created system is nearly independent of the longitudinal direction[4] as we can see in the sketch of figure 2.3.

[4] At least in the most central region

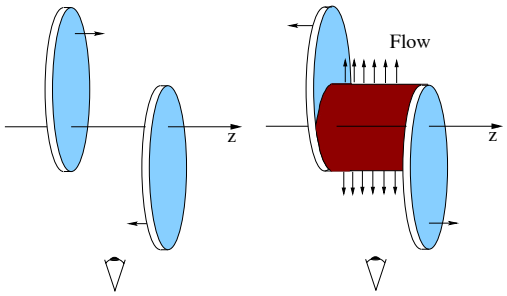

Figure 2.3.: Cartoon of the collision process from outside the system. Taken from [18].

Of course it is more reliable to have a justification by a measurement, than just a sketch. Therefore figure 2.4 shows data taken from LHC and RHIC heavy-ion collisions at various collision energies, which justify the already above mentioned geometry. As one can see the number of detected (charged) particles shows a plateau at mid-rapidity around $\eta = 0$. Hence the two dimensional approach is convenient as long as we are not aiming at physics "in the tail". As a remark let us mention that one can extract the total number of detected particles from 2.4 as well, which shows to be[5] ≈ 25000.

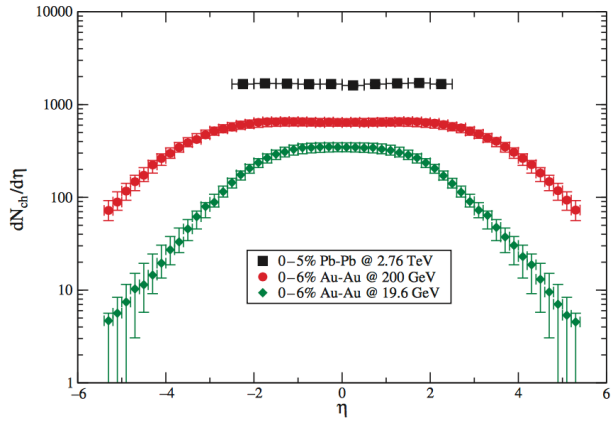

Figure 2.4.: Plot of the detected charged particle number over pseudorapidity η. Taken from [18].

2.3. Preparation

2.3.1. Christoffel symbols for Milne coordinates

In this section we need to elaborate how the choice of the spacetime components (2.2.13) affects the dynamics. Since we want to employ the above mentioned spacetime symmetry, which features a curvature, we have to rewrite several derivatives in order to work out a dynamical evolution equation. In order to do so we need to start with computing Christoffel symbols.

The general definition for the Christoffel symbols is the following.

[5] Number taken from [18] as well.

$$\Gamma^{\rho}_{\mu\nu} = \frac{1}{2} g^{\rho\alpha}(\partial_\mu g_{\nu\alpha} + \partial_\nu g_{\mu\alpha} - \partial_\alpha g_{\mu\nu}) \tag{2.3.1}$$

While taking a short look at formula (2.3.1) the following statement can be checked.

$$\Gamma^{\rho}_{\mu\nu} = \Gamma^{\rho}_{\nu\mu} \tag{2.3.2}$$

The metric we will use from now on, due to the mentioned Milne coordinates and polar symmetry has the following structure.

$$g_{\mu\nu} = \begin{array}{c} \\ \tau \\ \eta_s \\ r \\ \phi \end{array} \begin{array}{c} \begin{array}{cccc} \tau & \eta_s & r & \phi \end{array} \\ \begin{pmatrix} 1 & 0 & 0 & 0 \\ 0 & -\tau^2 & 0 & 0 \\ 0 & 0 & -1 & 0 \\ 0 & 0 & 0 & -r^2 \end{pmatrix} \end{array} \tag{2.3.3}$$

As can be seen easily we work in the mostly minus signature throughout this thesis. Based on the fact that the following statement holds, where δ^{μ}_{σ} denotes the Kronecker-Delta symbol, we can construct the inverse metric.

$$g^{\mu\nu} g_{\nu\sigma} = g^{\mu}{}_{\sigma} \stackrel{!}{=} \delta^{\mu}{}_{\sigma} \tag{2.3.4}$$

The inverse metric has the below form.

$$g^{\mu\nu} = \begin{array}{c} \\ \tau \\ \eta_s \\ r \\ \phi \end{array} \begin{array}{c} \begin{array}{cccc} \tau & \eta_s & r & \phi \end{array} \\ \begin{pmatrix} 1 & 0 & 0 & 0 \\ 0 & -\frac{1}{\tau^2} & 0 & 0 \\ 0 & 0 & -1 & 0 \\ 0 & 0 & 0 & -\frac{1}{r^2} \end{pmatrix} \end{array} \tag{2.3.5}$$

To calculate the non-vanishing Christoffel symbols, it is time saving to recognize that there are only the following two non-vanishing derivatives of $g_{\mu\nu}$.

$$\partial_\tau \; g_{\eta_s \eta_s} \tag{2.3.6}$$

as well as

$$\partial_r \; g_{\phi\phi} \tag{2.3.7}$$

This gives us for the terms in the bracket of the sum in (2.3.1) the following non-vanishing contributions.

1^{st} term of the sum:

$$\partial_\tau \; g_{\eta_s \eta_s} \quad \widehat{=} \quad \Gamma^{X}_{\tau \eta_s} \tag{2.3.8}$$

$$\partial_r \; g_{\phi\phi} \quad \widehat{=} \quad \Gamma^{X}_{r\phi} \tag{2.3.9}$$

2^{nd} term of the sum:

$$\partial_\tau \; g_{\eta_s\eta_s} \quad \widehat{=} \quad \Gamma^X_{\eta_s\tau} \tag{2.3.10}$$
$$\partial_r \; g_{\phi\phi} \quad \widehat{=} \quad \Gamma^X_{\phi r} \tag{2.3.11}$$

This summand reflects the symmetric behavior shown in equation (2.3.2).
3^{rd} term of the sum:

$$\partial_\tau \; g_{\eta_s\eta_s} \quad \widehat{=} \quad \Gamma^X_{\eta_s\eta_s} \tag{2.3.12}$$
$$\partial_r \; g_{\phi\phi} \quad \widehat{=} \quad \Gamma^X_{\phi\phi} \tag{2.3.13}$$

The next step is to determine the still indetermined index, which is up to here labeled with the capital X in the above formulas (2.3.8) – (2.3.13). Benefiting from the diagonality of both $g_{\mu\nu}$ and $g^{\mu\nu}$, which have to be multiplied due to definition (2.3.1), one can deduce the only non-vanishing parts of the different terms. These are presented in the following.
1^{st} term of the sum:

$$g^{\rho\eta_s} \; \partial_\tau \; g_{\eta_s\eta_s} \neq 0 \quad \Leftrightarrow \quad \rho = \eta_s \Rightarrow \Gamma^{\eta_s}_{\tau\eta_s} \tag{2.3.14}$$
$$g^{\rho\phi} \; \partial_r \; g_{\phi\phi} \neq 0 \quad \Leftrightarrow \quad \rho = \phi \Rightarrow \Gamma^{\phi}_{r\phi} \tag{2.3.15}$$

2^{nd} term of the sum:

$$g^{\rho\eta_s} \; \partial_\tau \; g_{\eta_s\eta_s} \neq 0 \quad \Leftrightarrow \quad \rho = \eta_s \Rightarrow \Gamma^{\eta_s}_{\eta_s\tau} \tag{2.3.16}$$
$$g^{\rho\phi} \; \partial_r \; g_{\phi\phi} \neq 0 \quad \Leftrightarrow \quad \rho = \phi \Rightarrow \Gamma^{\phi}_{\phi r} \tag{2.3.17}$$

3^{rd} term of the sum:

$$g^{\rho\tau} \; \partial_\tau \; g_{\eta_s\eta_s} \neq 0 \quad \Leftrightarrow \quad \rho = \tau \Rightarrow \Gamma^{\tau}_{\eta_s\eta_s} \tag{2.3.18}$$
$$g^{\rho r} \; \partial_r \; g_{\phi\phi} \neq 0 \quad \Leftrightarrow \quad \rho = r \Rightarrow \Gamma^{r}_{\phi\phi} \tag{2.3.19}$$

All in all we get the following expressions for the non-vanishing Christoffel symbols.
1^{st} term of the sum:

$$\Gamma^{\eta_s}_{\tau\eta_s} \quad = \quad \frac{1}{2} \; g^{\eta_s\eta_s}(\partial_\tau g_{\eta_s\eta_s} + 0 - 0) = \frac{1}{\tau} \tag{2.3.20}$$
$$\Gamma^{\phi}_{r\phi} \quad = \quad \frac{1}{2} \; g^{\phi\phi}(\partial_r g_{\phi\phi} + 0 - 0) = \frac{1}{r} \tag{2.3.21}$$

2^{nd} term of the sum:

$$\Gamma^{\eta_s}_{\eta_s\tau} \quad = \quad \frac{1}{2} \; g^{\eta_s\eta_s}(0 + \partial_\tau g_{\eta_s\eta_s} - 0) = \frac{1}{\tau} \tag{2.3.22}$$
$$\Gamma^{\phi}_{\phi r} \quad = \quad \frac{1}{2} \; g^{\phi\phi}(0 + \partial_r g_{\phi\phi} - 0) = \frac{1}{r} \tag{2.3.23}$$

3^{rd} term of the sum:

$$\Gamma^{\tau}_{\eta_s\eta_s} \quad = \quad \frac{1}{2} \; g^{\tau\tau}(0 + 0 - \partial_\tau g_{\eta_s\eta_s}) = \tau \tag{2.3.24}$$
$$\Gamma^{r}_{\phi\phi} \quad = \quad \frac{1}{2} \; g^{rr}(0 + 0 - \partial_r g_{\phi\phi}) = -r \tag{2.3.25}$$

With the above equations (2.3.20) up to (2.3.25) we computed all non-vanishing Christoffel symbols for the Milne-coordinates. As a cross-check one can realize that they are in accordance with the symmetry presented in equation (2.3.2).

2.3.2. The integration measure for the Milne geometry

First it is our task, to translate the integration measure, which can be found for example in [19][6] into our symmetry. In general the integration measure is constructed as follows.

$$\int d^4p\ \Theta(p^0)\ \frac{\delta(p^2-m^2)}{\sqrt{-det(g)}}$$

Here δ is the one-dimensional Dirac-Delta distribution. This Delta distribution is assuring the mass-shell condition, which has to be fulfilled by physically measurable particles. The denominator is build up by the square root of the metric's determinant.

$$\begin{aligned}&\int d^4p\ \Theta(p^0)\ \frac{\delta(p^2-m^2)}{\sqrt{-det(g)}}\\ =\ &\int \frac{d^4p}{\sqrt{-det(g)}}\ \Theta(p^\tau)\ \delta\left((p^\tau)^2-(p^r)^2-\tau^2(p^{\eta_s})^2-r^2(p^\phi)^2-m^2\right)\end{aligned}$$

For the Dirac-Delta distribution depending on a function $f(x)$ it is known one can reformulate the distribution with respect to the function's argument.

$$\delta(f(x))=\sum_{i=1}^{N}\frac{\delta(x-x_i)}{|f'(x_i)|}$$

In the upper formula the sum runs over all zeroes of $f(x)$, which are denoted by x_i. The prime indicates the first derivative of the function with respect to x. We use this relation in order to solve the p^τ integral.

$$\begin{aligned}&\Theta(p^\tau)\ \delta\left((p^\tau)^2-(p^r)^2-\tau^2(p^{\eta_s})^2-r^2(p^\phi)^2-m^2\right)\\ =\ &\Theta(p^\tau)\\ &\left(\frac{\delta(p^\tau-\sqrt{(p^r)^2+\tau^2(p^{\eta_s})^2+r^2(p^\phi)^2+m^2})}{2|p_\tau|}\right.\\ &\left.+\frac{\delta(p^\tau+\sqrt{(p^r)^2+\tau^2(p^{\eta_s})^2+r^2(p^\phi)^2+m^2})}{2|p_\tau|}\right)\\ =\ &\Theta(p^\tau)\left(\frac{\delta(p^\tau-\sqrt{(p^r)^2+\tau^2(p^{\eta_s})^2+r^2(p^\phi)^2+m^2})}{2|p_\tau|}\right)\end{aligned}$$

Because of the stepfunction $\Theta(p^\tau)$ the second Delta-distribution will never give a contribution. Now we are able to perform the p^τ-integral. Finally we end up with an expression for the integration measure.

[6] Section A.3

$$\int \frac{d^4p}{\sqrt{-det(g)}}\ \Theta(p^0)\ \delta(p^2-m^2) = \int \frac{d^3p}{2\sqrt{-det(g)}\ p_\tau}, \tag{2.3.26}$$

where p_τ is given by the corresponding mass-shell condition.

$$p_\tau = g_{\tau\tau}p^\tau = g_{\tau\tau}\sqrt{(p^r)^2+\tau^2(p^{\eta_s})^2+r^2(p^\phi)^2+m^2}.$$

At this point we have to insert the determinant of the metric (2.3.3) in order to have the translated momentum integral measure for our spacetime symmetry.

$$\frac{d^3p}{2p_\tau\sqrt{-det(g)}} = \frac{d^3p}{2(\tau r)p_\tau}$$

Note that in the above metric (2.3.3) the $\tau\tau$-component is equal to 1. Therefore we will be sloppy and write p^τ instead of p_τ. With the unit-vectors (2.2.17) up to (2.2.20) one can modify the integration measure to the final expression.

$$\begin{aligned}\int \frac{d^3p}{2(\tau r)p^\tau} &= \int_{-\infty}^{\infty} dp^r \int_{-\infty}^{\infty} r\ dp^\phi \int_{-\infty}^{\infty} \tau\ dp^{\eta_s}\ \frac{1}{2(\tau r)p^\tau} \\ &= \int_{-\infty}^{\infty} dp^r \int_{-\infty}^{\infty} dp^\phi \int_{-\infty}^{\infty} dp^{\eta_s}\ \frac{1}{2p^\tau}\end{aligned} \tag{2.3.27}$$

2.4. Relativistic Boltzmann equation in polar Milne coordinates

In this section we want to derive the relativistic Boltzmann equation in polar Milne coordinates (2.2.13) for one particle species. Please note that we are presenting more a phenomenological motivated approach instead of a strict mathematical derivation. We are only looking for the effect of the curved spacetime on the resulting dynamics of the system. Therefore we will not include external forces, which could for example arise from an electric field.

The Boltzmann equation in general is the classical evolution equation of the on-shell single particle distribution function in phase space $f(x^\mu, p^i)$. Since we want to work in a setup where the particle number is fixed, we can normalize the single-particle phase space distribution to the total particle number in the system N, as it is usually done, i.e.

$$\int \frac{d^3p\ d^3x}{(2\pi)^3} f(x^\mu, p^i) = N(t) = N$$

With this normalization for $f(x^\mu, p^i)$, we can interpret the distribution function to be a number density of particles in the phase space around the point (x^μ, p^i). This function is contravariant in momentum-space as pointed out in [19] and [20]. It depends only on seven fields, because of the mass-shell condition[7] for the particles which are described by $f(x^\mu, p^i)$. Note that we have to work within this statistical approach – dealing with densities – since the number of effective degrees of freedom is too high[8] in order to apply a deterministic

[7] see chapter 2.3.2

[8] See for example figure 2.4.

framework.

2.4.1. Relativistic drift term in polar Milne coordinates

The purely streaming behavior of a many-particle system is described by the left hand side of the Boltzmann equation, which is called drift term. Within this section we are deriving an expression for the drift term respecting our phase space symmetries. The beginning of the following derivation of the drift term is inspired by [21] (page 331 et sqq.)[9].

For particles with rest mass m their 4-momentum is defined by the following formula.

$$p^\mu = m\frac{dx^\mu}{d\tilde{\tau}} \tag{2.4.1}$$

Whereas the proper time τ in the Milne coordinates is with respect to momentum along the beam axis p^z, here the proper time $\tilde{\tau}$ is with respect to the whole three-dimensional momentum $\vec{p}$. Furthermore for the derivative of the momentum components p^i with respect to the proper time $\tilde{\tau}$ holds the statement.

$$\frac{dp^i}{d\tilde{\tau}} = m\ \frac{d^2x^i}{d\tilde{\tau}^2} \tag{2.4.2}$$

The motion on a geodesic line – which is the motion of a free particle through a curved space – is given by the following formula.

$$\begin{aligned} 0 &= \frac{du^\mu}{d\tilde{\tau}} = \frac{d^2x^\mu}{d\tilde{\tau}^2} + \Gamma^\mu_{\sigma\nu}\frac{dx^\sigma}{d\tilde{\tau}}\ \frac{dx^\nu}{d\tilde{\tau}} \\ \Leftrightarrow \frac{dp^i}{d\tilde{\tau}} &= -m\ \Gamma^i_{\mu\nu}\frac{dx^\mu}{d\tilde{\tau}}\ \frac{dx^\nu}{d\tilde{\tau}} \end{aligned} \tag{2.4.3}$$

With the above, we elaborated all ingredients to derive the Boltzmann equation's drift term. We just need to take the total derivative of the distribution function $f(x^\mu, p^i)$ with respect to proper time. After performing the chain rule one has to insert the expressions (2.4.1) and (2.4.3) in order to gain an expression for the drift term.

$$\begin{aligned} m\frac{df(x^\mu,p^i)}{d\tilde{\tau}} &= m\frac{\partial f}{\partial x^\mu}\frac{dx^\mu}{d\tilde{\tau}} + m\frac{\partial f}{\partial p^i}\frac{dp^i}{d\tilde{\tau}} \\ &= p^\mu\frac{\partial f}{\partial x^\mu} - m^2\ \Gamma^i_{\mu\nu}\frac{dx^\mu}{d\tilde{\tau}}\frac{dx^\nu}{d\tilde{\tau}}\frac{\partial f}{\partial p^i} \\ &= p^\mu\frac{\partial f}{\partial x^\mu} -\ \Gamma^i_{\mu\nu}\ p^\mu p^\nu\frac{\partial f}{\partial p^i} \end{aligned} \tag{2.4.4}$$

Note that here we did an important assumption. Namely we assumed the absence of external forces in the system. In general such forces could be existent for example via external gravitational, electric or magnetic fields. If they are present, they would contribute via Newton's second axiom to a change in the momentum space. In our setup a "change in

[9] Please note that this book is written in order „to present the theory and applications of the relativistic Boltzmann equation in a self-containing manner "(Preface). If the reader prefers to read original publications, as for example [22] one can search for the cited articles within the book [21].

momentum space" just happens due to the curvature, but particles do not get accelerated as one can already see in the first line of (2.4.3).

Equation (2.4.4) builds the left-hand side of the Boltzmann equation and is often called drift term. It describes the phase space densities – and therefore the system – dynamics in position and momentum space over time due to the corresponding gradients. As one can see the non trivial evolution will stop, when all the gradients are vanishing.

For the proper symmetries of our system we have to insert the computed Christoffel symbols for the polar Milne coordinates from chapter 2.3.1 into equation (2.4.4). Therefore the drift term for our spacetime symmetries finally reads.

$$\left[p^\tau \partial_\tau + p^{\eta_s} \partial_{\eta_s} + p^\phi \partial_\phi + p^r \partial_r - \frac{2}{\tau} p^\tau p^{\eta_s} \frac{\partial}{\partial p^{\eta_s}} - \frac{2}{r} p^r p^\phi \frac{\partial}{\partial p^\phi} + r p^\phi p^\phi \frac{\partial}{\partial p^r}\right] f(x^\mu, p^i) \quad (2.4.5)$$

2.4.2. Free streaming

Up to now we only implemented a more or less trivial setup, where the effective degrees of freedom just move on a geodesic line. Figure 2.5 is a sketch to illustrate the emerging dynamics. In fact it shows the particle's trajectories projected on the position space (left) and the velocity space (right) as a function of time. Note that the velocity space and the momentum space for particles with finite mass m are up to a factor m equivalent.

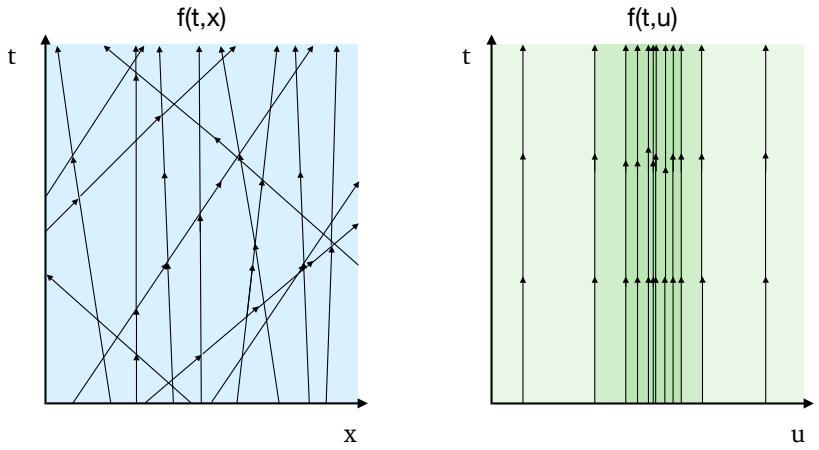

Figure 2.5.: Sketch of the dynamics of the system in position (left) space and in momentum (right) space. Inspired by [23]. Please note that this picture sketches the Cartesian case.

As one can see on the right hand side, there is no change in particle momentum or velocity over time. The background shade displays the density, the more paths are present in a region, the higher the density is. The crucial point is displayed on the left hand side of the figure. When two particle trajectories are crossing in position space, nothing happens, due to the fact that no interparticle interactions are implemented so far. So as long as particle trajectories are not crossing, the system's evolution is just driven by the drift term. This is for example the case in a system, where the microscopic mean free path or the Knudsen number Kn is infinite. In the heavy-ion collision process this is the case, as mentioned in the chapter 2.1, in the very last stage before the particle's detection.

For investigating the multiparticle system's evolution at the very end of the fireball's expansion we can assume that the system's dynamics is described by the drift term only. Therefore in this epoch we can describe the system via the relativistic, free streaming Boltzmann equation.

$$\Big[p^\tau \partial_\tau + p^{\eta_s}\partial_{\eta_s} + p^\phi \partial_\phi + p^r \partial_r \\ -\frac{2}{\tau}p^\tau p^{\eta_s}\frac{\partial}{\partial p^{\eta_s}} - \frac{2}{r}p^r p^\phi \frac{\partial}{\partial p^\phi} + r p^\phi p^\phi \frac{\partial}{\partial p^r}\Big] f(x^\mu, p^i) = 0 \tag{2.4.6}$$

From a mathematical point of view, equation (2.4.6) is a homogeneous partial differential equation.

2.4.3. Balance equations or Collision integrals

As the system's Knudsen number Kn becomes finite instead of infinite one can not ignore the interaction of the degrees of freedom anymore, because the microscopic interactions will play an increasing role for the systems evolution. For implementing, at least in a phenomenological way, the effect of collisions, there are some well established models. In the present and following sections two of these models are presented shortly. Basically these approximations are implemented at the right hand side of the Boltzmann equation.

$$\Big[p^\tau \partial_\tau + p^{\eta_s}\partial_{\eta_s} + p^\phi \partial_\phi + p^r \partial_r \\ -\frac{2}{\tau}p^\tau p^{\eta_s}\frac{\partial}{\partial p^{\eta_s}} - \frac{2}{r}p^r p^\phi \frac{\partial}{\partial p^\phi} + r p^\phi p^\phi \frac{\partial}{\partial p^r}\Big] f(x^\mu, p^i) = E_p \left(\frac{df}{dt}\right)_{Coll} \tag{2.4.7}$$

From a microscopical point of view the best justified Ansatz for the right hand side of the Boltzmann equation is based on a balance approach. The basic idea is that microscopical collisions can in principle induce two consequences: either a collision can scatter a particle inside a certain phase space element (gain-term), or it can scatter a particle out of a certain phase space element (loss-term). Under the assumption that a collision happens only local and instantaneous one can model the so called collision term $\left(\frac{df}{dt}\right)_{Coll}$. Note that here another scale separation is hidden, since we demand the local scatterings to act on such small scales, that they are – compared to the phase space elements under investigation (x^μ, p^i) – point like. Therefore one has to coarse grain the phase space in order to circumvent the quantum mechanical scattering procedure.

The collision term $\left(\frac{df}{dt}\right)_{Coll}$ is modeled as follows.

$$\left(\frac{df}{dt}\right)_{Coll} = \sum_k \frac{g_k\left(1-\frac{\delta_{ik}}{2}\right)}{(2\pi)^3}\int d^3\vec{p_k}\; d\Theta\; v_{rel_{ik}} \\ \left[f(x^\mu, \vec{p_i}')f_k(x^\mu, \vec{p_k}') - f(x^\mu, \vec{p_i})f_k(x^\mu, \vec{p_k})\right]\frac{d\sigma_{ik}}{d\Theta} \tag{2.4.8}$$

Here the sum is running over all the relevant particle species in the system. The factor g_k is the corresponding degeneracy factor and f_k is the respective distribution function for particles of kind k. The integral runs over all the momenta of the participating particles in a collision

where one particle with momentum $\vec{p_i}$ is entering/leaving the phase space element under investigation. Due to this fact one term is positive in order to gain a particle, whereas the other term involving $f(t, x, \vec{p_i})$ comes with a negative sign. This justifies the denomination balance equation. The angle Θ is the solid scattering angle and $v_{rel_{ik}}$ is the relative velocity between the two colliding particles. An important ingredient is the differential cross section $\frac{d\sigma_{ik}}{d\Theta}$ for processes involving particle species i and k. In principle here one can incorporate computed differential cross sections for example from quantum field theory or one can extract the measured total cross sections from [6][10]. Since in our setup there is only one particle species at play, the sum running over particle species k can be omitted.

An often used extension in order to describe the particles quantum statistics well, is to incorporate Pauli-blocking or Bose-enhancement via involving the densities of the states after/before the collision.

$$\begin{aligned}\left(\frac{df}{dt}\right)_{Coll} = & \sum_k \frac{g_k\left(1-\frac{\delta_{ik}}{2}\right)}{(2\pi)^3}\int d^3\vec{p_k}\; d\Theta\; v_{rel_{ik}} \\ & \Big[f(x^\mu,\vec{p_i}')f_k(x^\mu,\vec{p_k}')(1\pm f(x^\mu,\vec{p_i}))(1\pm f_k(x^\mu,\vec{p_k})) \\ & -f(x^\mu,\vec{p_i})f_k(x^\mu,\vec{p_k})(1\pm f(x^\mu,\vec{p^i}'))(1\pm f_k(x^\mu,\vec{p^k}'))\Big]\,\frac{d\sigma_{ik}}{d\Theta}\end{aligned}$$

In the above formula the minus sign generates the fermionic repulsion in case the phase space element is already occupied and the plus resembles the attractive force for bosons in case of an occupied phase space element.

Another feature which is used sometimes is a phenomenological extension to two-to-three particle collisions or decays.

Compared to the free streaming case described in section 2.4.2, figure 2.6 illustrates the change in the system's dynamics induced by the collision term $\left(\frac{df}{dt}\right)_{Coll}$.

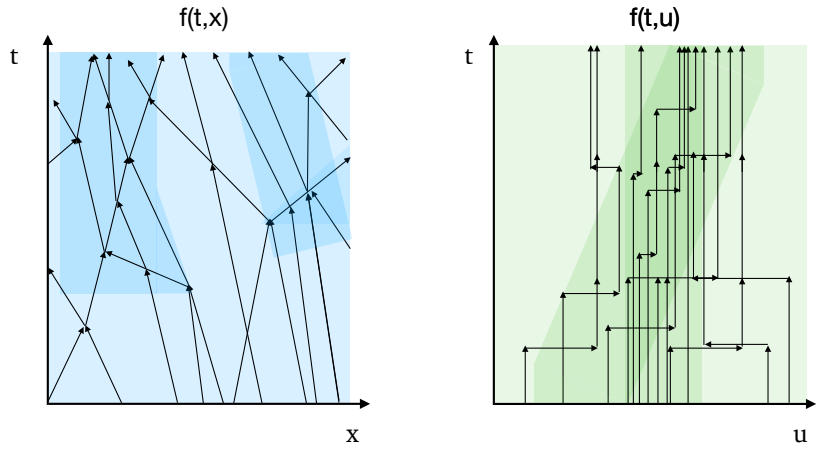

Figure 2.6.: Sketch of the dynamic of the system in position (left) space and in momentum (right) space. Inspired by [23]. Please note that this picture sketches the Cartesian case.

[10]Note that especially for heavy-ion transport there is often an additional 'in-medium rescaling' used, which takes the effect of the surrounding medium into account.

Again on the left hand side the particle's trajectories projected on the position space are sketched, whereas on the right hand side one can see the projection on the velocity space. Whenever two paths in position space are crossing, a collision takes place. This collision induces a non trivial behavior in the velocity or momentum space, since after a collision the particle velocity changes. As it is indicated by the shaded area the result is a non trivial evolution of the density function in both, position and momentum spaces. This can be seen by comparing the shaded areas of figure (2.6) to the shaded areas in figure (2.5).

As a mathematical remark it is very important to know, that while inserting (2.4.8) into the Boltzmann equation 2.4.7, one needs to solve an integro-differential equation, which is quadratic in the desired distribution function $f(x^\mu, p^i)$. To solve such an equation is very complex and challenging mathematicians since a long time. In addition one should keep in mind, that these equations in general are in addition coupled through the different particle species i and k.

Nevertheless the ansatz for describing a system of many interacting particles is commonly used, although it is quite expensive in terms of computation time. Often the system described by the Boltzmann equation is rather simulated, than actually solving the mathematical integro-differetial equation by computer codes. For a recent overview of state of the art computer codes working with this collision integral see for example all the so-called BUU[11] codes in [24].

Studies with this ansatz for the collision term – really computing the Collision integral, instead of just simulating the underlying particle dynamics – done by our group are [25] and [26].

The last remark of this section is on the cases where the collision integral $\left(\frac{df}{dt}\right)_{Coll}$ is vanishing. This can be the case in two situations, which are from a physical point of view very far away from each other[12]. Either the collision integral can vanish due to the fact that all distribution functions are the local equilibrium functions. If this is the case, the difference in the brackets of equation (2.4.8) is zero. Physically this is interpreted in such a way that the microscopical interactions drive the system to a local equilibrium state $f_{eq}(x^\mu, p^i)$ on a rather small time scale. Once such a state is achieved, the effect of further interactions do not contribute to the system's dynamics anymore. To say it in other words, there exist distribution functions $f_{eq}(x^\mu, p^i)$, which can cancel the collision integral. These solutions are called local equilibrium solutions. Please keep in mind, that they are not automatically a solution to the whole Boltzmann equation, since it could be the case that they are not a solution to the drift term or left hand side of the Boltzmann equation.

The collision integral is also vanishing in the case of vanishing cross sections σ_{ik}. This is referred as the free streaming limit and was already mentioned above. In that setup interactions play no role in the system's dynamics. Therefore the system is not able to evolve to an equilibrium state. This is why this limit is sometimes called far from equilibrium limit.

So please keep in mind that in the case of infinitely many and in the case of no interactions the evolution equations look the same, although the microscopical situation is completely different.

2.4.4. Relaxation time approximation

The relaxation time approximation (RTA) is an approximation, which tries to phenomenologically mimic the effect of the collision integral in the proximity of a local equilibrium state

[11] BUU stands for Boltzmann-Uehling-Uhlenbeck.

[12] In principle they are as far away from each other as possible.

$f_{eq}(x^\mu, p^i)$. Since in the subsequent parts we will work on the relaxation time approximation, here we will just shortly present the main idea. As already mentioned this ansatz is valid in the vicinity of a local equilibrium state. The basic idea is that the distribution function $f(x^\mu, p^i)$ will locally relax to such an equilibrium distribution over a time scale τ_{rel}, which is called the relaxation time. It is obvious that this timescale has to be longer than the time between two microscopical collisions. With this model one circumvents the computationally challenging part of the individual collisions and distribution functions. In addition one linearizes the right hand side of the Boltzmann equation in the distribution function $f(x^\mu, p^i)$. With this ansatz one circumvents two mathematical challenging features of the Boltzmann equation (2.4.7). Namely one only has to deal with a partial differential equation instead of an intergro-differential one, and secondly one bypasses the nonlinearity of the collision kernel, which can be seen in equation (2.4.8).

In equation form the RTA ansatz for the Boltzmann equation's right hand side looks like the following.

$$-\frac{p^\mu u_\mu}{\tau_{rel}} \left(f(x^\mu, p^i) - f_{eq}(x^\mu, p^i) \right) \tag{2.4.9}$$

In expression (2.4.9) τ_{rel} has no dependence on the momentum, which means that the distribution function is relaxing on all momentum scales in the same way. Of course one can also deal with a momentum dependent relaxation time, this would reflect that particles with different momenta relax on different time scales to equilibrium. Often this ansatz is also called 1^{st} - linearization.

This model for the right hand side of the Boltzmann equation is often used, for example by [27], [28] or by another group [29].

If one further assumes that the system is locally near to a local equilibrium state $f_{eq}(x^\mu, p^i)$ – which will be approached during the system's evolution, due to the first linearization – one can linearize a second time. This time one linearizes the distribution function $f(x^\mu, p^i)$ with respect to its displacement $\delta f(x^\mu, p^i)$ to the local equilibrium state. Written in a formula the second linearization reads like the subsequent formula.

$$f(x^\mu, p^i) = f_{eq}(x^\mu, p^i) + \delta f(x^\mu, p^i) \tag{2.4.10}$$

Plugging (2.4.10) into (2.4.9) leads to the – compared to the full collision integral expression – handy expression for the right hand side of the Boltzmann equation after two linearizations.

$$-\frac{p^\mu u_\mu}{\tau_{rel}} \delta f(x^\mu, p^i) \tag{2.4.11}$$

Inserting these two linearizations one ends up with the phenomenological Boltzmann equation in Minkowski space.

$$p^\mu \partial_\mu \left(f_{eq}(x^\mu, p^i) + \delta f(x^\mu, p^i) \right) = -\frac{p^\mu u_\mu}{\tau_{rel}} \delta f(x^\mu, p^i) \tag{2.4.12}$$

2.4.5. Role of the Jüttner distribution

In this section we want to investigate how the free streaming Boltzmann equation (2.4.6), which we elaborated above, acts on the Jüttner-distribution[13] in the case of vanishing chemical potential, which is defined as the following.

$$f_{\text{Jüt}} \equiv C\ e^{-\frac{p^\mu u_\mu}{T}} \overset{\text{LRF}}{=} C\ e^{-\frac{p^\tau}{T}} \tag{2.4.13}$$

Where C is a normalization constant. This Jüttner distribution is the relativistic equivalent to the Maxwell-Boltzmann distribution, which is a solution to the classical Boltzmann equation when there are no quantum statistical effects. From a thermodynamical point of view this distribution function is describing a thermalized ideal gas. We boosted the distribution function into the local rest frame (LRF), where the only non vanishing component of the flow velocity field is the τ-component. As a first step we assume the temperature T to be constant in position space. We make this assumption in order to check whether this Jüttner distribution can solve the free streaming Boltzmann equation, which we elaborated above. Thus

$$p^\mu \frac{\partial\left(e^{-\frac{p^\tau}{T}}\right)}{\partial x^\mu} - \Gamma^i_{\mu\nu}\ p^\mu p^\nu \frac{\partial\left(e^{-\frac{p^\tau}{T}}\right)}{\partial p^i} \overset{?}{=} 0 \tag{2.4.14}$$

After a short look at equation (2.4.14) one realizes immediately that if p^τ would be independent of all the other p^i and x^μ components, the equation would be solved.

But of course this is not the case, since we need to implement the mass-shell condition.

$$\begin{aligned} m^2 &= p^\mu p_\mu = g_{\mu\nu}\ p^\mu p^\nu \\ &\Leftrightarrow\ p^\tau p^\tau \overset{(2.3.3)}{=} m^2 + \tau^2\ p^{\eta_s} p^{\eta_s} + p^r p^r + r^2\ p^\phi p^\phi \\ &\Leftrightarrow\ p^\tau = \sqrt{m^2 + \tau^2\ p^{\eta_s} p^{\eta_s} + p^r p^r + r^2\ p^\phi p^\phi} \end{aligned} \tag{2.4.15}$$

If we do so and use in addition the following.

$$\left(\frac{\partial}{\partial p^\mu}\right) p^2 = 2p_\mu$$

With all the above, we are able to rewrite the exponent of the Jüttner distribution in terms of the phase space components x^μ and p^i. Thus inserting expression (2.4.15) into the distribution (2.4.13) and further inserting this into the free streaming Boltzmann equation (2.4.6), while making use of the above shown rule for derivatives, we work out the following computation.

[13] Sometimes this distribution function is called Jüttner-Maxwell-Boltzmann distribution.

$$
\begin{aligned}
0 \quad &\overset{?}{=} \quad \left[p^\mu \frac{\partial}{\partial x^\mu} - \Gamma^i_{\mu\nu}\, p^\mu p^\nu \frac{\partial}{\partial p^i}\right] C e^{-\frac{p^\tau}{T}} \\
&\overset{(2.4.15)}{=} \quad C\left[p^\mu \frac{\partial}{\partial x^\mu} - \Gamma^i_{\mu\nu}\, p^\mu p^\nu \frac{\partial}{\partial p^i}\right] e^{-\frac{1}{T}\sqrt{m^2+\tau^2 p^{\eta_s} p^{\eta_s}+p^r p^r+r^2 p^\phi p^\phi}} \\
&= \quad C\left[p^\tau \partial_\tau + p^{\eta_s}\partial_{\eta_s} + p^\phi \partial_\phi + p^r \partial_r - \frac{2}{\tau} p^\tau p^{\eta_s} \frac{\partial}{\partial p^{\eta_s}} - \frac{2}{r} p^r p^\phi \frac{\partial}{\partial p^\phi} + r p^\phi p^\phi \frac{\partial}{\partial p^r}\right] \\
&\quad\; e^{-\frac{1}{T}\sqrt{m^2+\tau^2 p^{\eta_s} p^{\eta_s}+p^r p^r+r^2 p^\phi p^\phi}} \\
&= \quad -\frac{C}{T}\left[p^\tau \frac{1}{2p^\tau}\, 2\, \tau p^{\eta_s} p^{\eta_s} + p^r \frac{1}{2p^\tau} 2\, r\, p^\phi p^\phi\right] e^{-\frac{1}{T}\sqrt{m^2+\tau^2 p^{\eta_s} p^{\eta_s}+p^r p^r+r^2 p^\phi p^\phi}} \\
&\quad\; + \frac{C}{T}\left[\frac{2}{\tau}\frac{p^\tau p^{\eta_s}}{2p^\tau}\tau^2\, 2\, p^{\eta_s} + \frac{2}{r}\frac{p^r p^\phi}{2p^\tau} r^2\, 2\, p^\phi - r\frac{p^\phi p^\phi}{2p^\tau} 2p^r\right] \\
&\quad\; e^{-\frac{1}{T}\sqrt{m^2+\tau^2 p^{\eta_s} p^{\eta_s}+p^r p^r+r^2 p^\phi p^\phi}} \\
&= \quad \frac{-C}{T\, p^\tau}\left[\tau\, p^\tau p^{\eta_s} p^{\eta_s} + r\, p^r p^\phi p^\phi - 2\, \tau\, p^\tau p^{\eta_s} p^{\eta_s} - 2\, r\, p^r p^\phi p^\phi + r\, p^r p^\phi p^\phi\right] \\
&\quad\; e^{-\frac{1}{T}\sqrt{m^2+\tau^2 p^{\eta_s} p^{\eta_s}+p^r p^r+r^2 p^\phi p^\phi}} \\
&\overset{(2.4.15)}{=} \quad \frac{C}{T\, p^\tau}\left[\tau\, p^\tau p^{\eta_s} p^{\eta_s}\right] e^{-\frac{p^\tau}{T}} \\
\Leftrightarrow 0 \quad &= \quad \frac{C}{T}\left[\tau\, p^{\eta_s} p^{\eta_s}\right] e^{-\frac{p^\tau}{T}} \qquad (2.4.16)
\end{aligned}
$$

Equation (2.4.16) shows how the free streaming Boltzmann equation in our curved basis acts on the Jüttner distribution $f_{\text{Jüt}}$. After taking a short glimpse at this expression it seems that the Jüttner distribution (2.4.13) is no solution to our free streaming Boltzmann equation.

What we found so long, is the fact that the expansion in the η_s-direction pulls the system away from equilibrium. In a spacetime setup where a component expands with time, it is impossible to find a solution which is time independent. The system, which is initially a thermodynamic one, is not able to reach equilibrium, in the sence of a time independent state, when the space is always changing.[14] This is comparable with a statement made in [21](page 336). Also from a physical point of view the above result is reasonable. Since we implemented the Bjorken flow in the longitudinal component, this component has to exhibit such a non trivial flow, which is reflected by the non vanishing drift term in equation (2.4.16).

But one has to mention that the mid-rapidity constraint $p^{\eta_s} = 0$ is often used while analyzing heavy-ion collision geometries. If we assume the mid rapidity assumption here as well, the Jüttner distribution, which is describing thermal equilibrium, is a solution to our setup. But of course one should keep in mind that we are only able to make statements for the dynamics of the mid rapidity region. Therefore our computations will not be valid "at the longitudinal edges" of the fireball. Comparing with figure 2.4 the mid rapidity description is valid roughly up to the region $|\eta| = 1.5$ for the green data set and up to $|\eta| = 3$ for the top RHIC energies (red data set). For LHC data one can not make a trustworthy statement from this plot.

Therefore we can assume that a system initialized in a state, which is described by the Jüttner distribution, will stay – at least in the mid rapidity region – in such a thermodynamic

[14] For an interesting discussion see [30] where they found, "for a particular initial condition this set can be solved exactly, yielding the first analytical solution of the Boltzmann equation for an expanding system."

equilibrium state during the whole free streaming evolution, because neither the expansion nor interactions are able to remove the system from equilibrium.

Note that the Jüttner-distribution is also in the cylindrical symmetric (with additional mid-rapidity: $p^{\eta_s} = 0$ assumption) case an equilibrium distribution, since the ∂_ϕ and ∂_{η_s} derivatives give no additional contribution.

2.4.6. Closing remark

At this point one should ask what is left to do. Since we know a solution – namely – the Jüttner solution, which is solving the drift term and – what I did not present explicitly but should be clear – the collision integral (2.4.8).

First I can imagine that some people would be very disappointed, if the thesis would be already over at this point, but an even more important second reason for our further investigations can be seen if we take a look at the microscopic scales that are involved in the description.

As we mentioned at the beginning for applying kinetic theory it is good to have a separation of the microscopic scale to the macroscopic scale. The characteristic quantity for such a scale separation is the Knudsen number Kn. Therefore let us take a look at the Knudsen number in the setup. It is clear that the microscopic scale is hidden in the collision term (2.4.8). To see this let us divide the collision integral by a typical scale f_c for the distribution function.

$$\begin{aligned}\frac{1}{f_c}\left(\frac{df}{dt}\right)_{Coll} &= \sum_k \frac{g_k\left(1-\frac{\delta_{ik}}{2}\right)}{(2\pi)^3}\underbrace{\int d^3p_k}_{\propto p^3}\underbrace{v_{rel_{ik}}}_{\propto\frac{r}{\tau}}\underbrace{\frac{d\sigma_{ik}}{d\Theta}\,d\Theta}_{\propto r^2} \\ &\quad \underbrace{\frac{1}{f_c}}_{\propto r^3p^3}\underbrace{\left[f(t,x,p_{i'})f_k(t,x,p_{k'})-f(t,x,p_i)f_k(t,x,p_k)\right]}_{\propto(r^{-3}p^{-3})^2} \propto \frac{1}{\tau}\end{aligned}$$

Let us denote the characteristic time scale of the collision term by $\tau = \tau_{coll}$. This is the typical time scale on which the microscopical interactions influence the systems dynamics. With the degree of freedom's typical velocity v_s one can relate τ_{coll} and l_{mfp} via

$$l_{mfp} \approx v_s\ \tau_{coll}. \tag{2.4.17}$$

The macroscopic length L, is basically characterized by the inverse of the typical size of the gradients in position space of the drift term (2.4.4).

When we look at the ideal hydrodynamical limit, where many particle interactions are at play,[15] the Knudsen number Kn is very small, if the gradients in the drift term are small enough. In the $Kn = 0$ limit there are very many interactions, but the collision term does not contribute to the dynamics, since it lives on too small time scales. Starting from this small Kn-setup one can perform a systematic expansion in the small Kn in order to get corrections due to the finiteness of τ_{coll}. This was done in an extremly systematic way, including another expansion parameter called Reynolds number, which basically is a number characterizing hydrodynamical flow, in the so-called DNMR-formalism[16] [31].

[15] Be aware that the Boltzmann ansatz is pushed to a limit where one should get trouble with the concept, since interactions are not rare anymore.

[16] DNMR stands for Denicol, Niemi, Molnar and Rischke, who are the authors of the cited publication.

Another ansatz which tries somehow to re-sum the corrections in the Knudsen number arising from anisotropies is the anisotropic hydrodynamics. Within this formalism we performed our previous studies [11], as mentioned in section 2.1.

At the other limit, where particles are free streaming, the mean free path is infinite. To expand in a meaningful way in a small parameter, it is advised to expand in inverse Knudsen number Kn^{-1}. But up to now we are not aware of such a procedure carried out in the systematics of the DNMR-formalism. Although [26] can be understood as being a first step into this direction. Due to the lack of such a formalism, we come back to the formalism of the anisotropic hydrodynamics and look how this formalism is translated throughout the evolution from small to infinite Knudsen number.

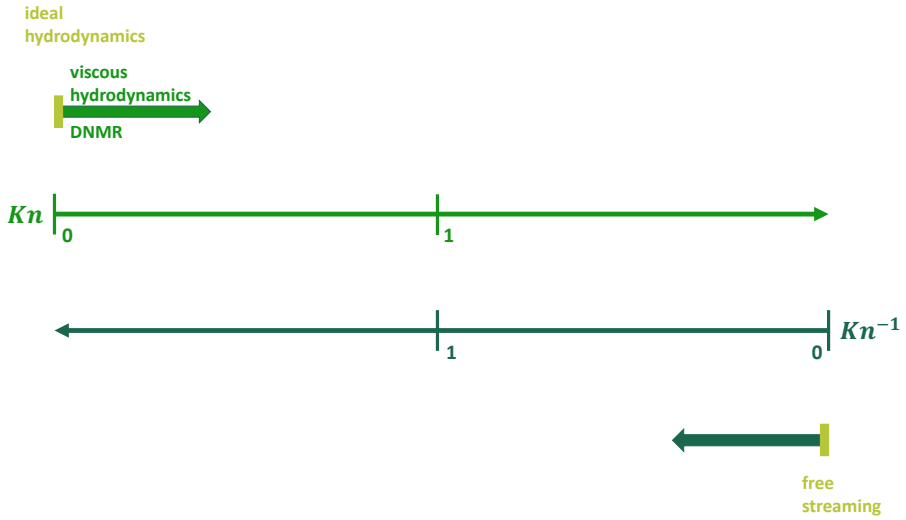

Figure 2.7.: Sketch of the approaches for describing transport in the different Knudsen number regimes Kn.

Figure 2.7 illustrates the different Knudsen number regimes and the corresponding suitable theoretical tools for describing transport in the regimes. It is important to note that right now there exists no systematic expansion for the $Kn^{-1} \gtrapprox 0$ regime. That is why the dark green arrow is not labeled.

2.5. The steady state free streaming solution

In this section we are presenting the free streaming solution to the steady version of the free streaming Boltzmann equation (2.4.6), which features anisotropies. Therefore our setup is a system whose evolution is not affected by particle interaction and in addition that has no time dependence. In some sense we are approaching the freeze out process from the infinite Knudsen number side with a tool that worked well in the "not small anymore"– Kn regime.

2.5.1. Derivation

In principle we describe a gas of non-interacting particles, which are permanently emitted by a "source" sitting at $r = 0$ in order to guarantee the time independence of the system's evolution. Figure 2.8 illustrates the flow pattern. The blue dot represents a continuously

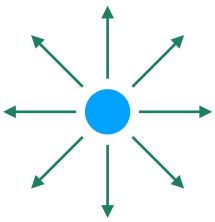

Figure 2.8.: Sketch of the dynamical set up.

particle emitting source. Of course one has to improve this simplification if one thinks of the freeze out process. But leaving aside 'turn on' and 'turn off' effects of the freeze out process, due to the non stationary nature of the experiment, we can study the kinetic freezeout's main time interval.

To do so we need the central element of the anisotropic hydrodynamic formalism, which is namely the Romatschke-Strickland distribution [32]. The most general mid-rapidity ansatz for this distribution reads as the following.

$$\begin{aligned} f_{RS}(x^\mu, p^i) &= Ce^{-\sqrt{\frac{m^2}{\Lambda^2}+\frac{p^r p^r}{\Lambda^2}(1+\xi^r)+\frac{r^2 p^\phi p^\phi}{\Lambda^2}\left(1+\xi^\phi\right)+\frac{\tau^2 p^{\eta_s} p^{\eta_s}}{\Lambda^2}(1+\xi^{\eta_s})}} \\ &\overset{p^{\eta_s}=0}{=} Ce^{-\sqrt{\frac{m^2}{\Lambda^2}+\frac{p^r p^r}{\Lambda^2}(1+\xi^r)+\frac{r^2 p^\phi p^\phi}{\Lambda^2}\left(1+\xi^\phi\right)}} \end{aligned} \tag{2.5.1}$$

Where C is a constant, Λ is the anisotropic temperature, m represents the particle's mass and the ξ^r and ξ^ϕ are anisotropy parameters. They ensure that the different momentum components are weighted in a different way. With their inclusion one is able to tune the anisotropy in momentum space.

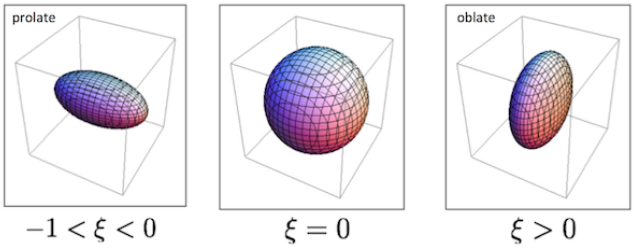

Figure 2.9.: Sketch of the effect of the anisotropy Parameter ξ. The shaded area indicates the surface of equal density in momentum space. Taken from [13].

Figure 2.9 is a plot, which indicates the impact of one anisotropy parameter ξ through plotting the surface of equal density in momentum space. As one can see for ξ equal to zero the system is isotropic in momentum space. In this case the distribution function (2.5.1) has the same form as the Jüttner distribution (2.4.13). Further one can identify the "anisotropic temperature" to be the thermodynamical temperature T. This fact clarifies the label anisotropic temperature for Λ, since the parameter plays in the presence of anisotropy the role that a temperature plays in case of a thermalized (isotropic) medium.

For $\xi > 0$ the associated direction becomes compressed compared to the other momentum components, whereas for $-1 < \xi < 0$ the anisotropic momentum component becomes

elongated. After a short glimpse at formula (2.5.1) it is clear that ξ^i can not be less than -1, since the distribution function would become a complex number. But in order to be a distribution function it has to be a real function for all (physical) momenta.

Note that we do not incorporate quantum statistic effects like Bose enhancement or Pauli blocking into the distribution function (2.5.1). Further we assume the anisotropy parameter to be spacetime dependent ($\xi^i = \xi^i(x^\mu)$).

In principle one can now compute the moments of the distribution function (2.5.1) in order to compute the consequential hydrodynamic evolution. As well one can insert this ansatz in the Cooper-Frye integral and compute particle spectra. This – and a little bit more – was all done in [11]. But for all these computations ξ was just a free parameter. We are now applying the – in the heavy-ion process – subsequent kinetic evolution in order to fill this parameter with a kinetic meaning. Eventually this procedure will govern a much smoother transition of both theories and in addition it diminishes the number of free parameters in the description.

In order to achieve this, we insert the Romatschke-Strickland distribution (2.5.1) into the free streaming Boltzmann equation (2.4.6) for mid-rapidity under the assumption of time independence. Performing the derivatives – under the assumption that the anisotropic temperature Λ is constant – leads to the following computation[17].

$$0 \stackrel{!}{=} \left[p^r\partial_r + p^\phi\partial_\phi - \frac{2}{r}p^r p^\phi\frac{\partial}{\partial p^\phi} + r p^\phi p^\phi\frac{\partial}{\partial p^r}\right] C e^{-\sqrt{\frac{m^2}{\Lambda^2}+\frac{p^r p^r(1+\xi^r)}{\Lambda^2}+\frac{r^2 p^\phi p^\phi(1+\xi^\phi)}{\Lambda^2}}}$$

Performing the derivatives leads to the following.

$$\begin{aligned}
= \quad & \left[p^r\left(-\frac{2rp^\phi p^\phi(1+\xi^\phi)+r^2p^\phi p^\phi(\partial_r\xi^\phi)+p^r p^r(\partial_r\xi^r)}{2\Lambda^2\sqrt{\frac{m^2}{\Lambda^2}+\frac{p^r p^r(1+\xi^r)}{\Lambda^2}+\frac{r^2p^\phi p^\phi(1+\xi^\phi)}{\Lambda^2}}}\right)\right. \\
& +p^\phi\left(-\frac{r^2p^\phi p^\phi(\partial_\phi\xi^\phi)+p^r p^r(\partial_\phi\xi^r)}{2\Lambda^2\sqrt{\frac{m^2}{\Lambda^2}+\frac{p^r p^r(1+\xi^r)}{\Lambda^2}+\frac{r^2p^\phi p^\phi(1+\xi^\phi)}{\Lambda^2}}}\right) \\
& -\frac{2}{r}p^r p^\phi\left(-\frac{2r^2p^\phi(1+\xi^\phi)}{2\Lambda^2\sqrt{\frac{m^2}{\Lambda^2}+\frac{p^r p^r(1+\xi^r)}{\Lambda^2}+\frac{2r^2p^\phi p^\phi(1+\xi^\phi)}{\Lambda^2}}}\right) \\
& \left.+rp^\phi p^\phi\left(-\frac{2p^r(1+\xi^r)}{2\Lambda^2\sqrt{\frac{m^2}{\Lambda^2}+\frac{p^r p^r(1+\xi^r)}{\Lambda^2}+\frac{r^2p^\phi p^\phi(1+\xi^\phi)}{\Lambda^2}}}\right)\right] f_{RS}(x^\mu,p^i)
\end{aligned}$$

Under the assumption that the distribution function f_{RS} does not vanish we have to deal with the expression:

$$\begin{aligned}
\overset{f_{RS}\neq 0}{\Leftrightarrow} 0 \quad = \quad & \Big[-2rp^r p^\phi p^\phi(1+\xi^\phi) - r^2p^r p^\phi p^\phi(\partial_r\xi^\phi) - p^r p^r p^r(\partial_r\xi^r) - r^2p^\phi p^\phi p^\phi(\partial_\phi\xi^\phi) \\
& -p^r p^r p^\phi(\partial_\phi\xi^r) + 4rp^r p^\phi p^\phi(1+\xi^\phi) - 2rp^r p^\phi p^\phi(1+\xi^r)\Big]
\end{aligned}$$

[17] The author apologizes for interchanging the traditional left hand side and the right hand side.

Here we can reorganize the terms in the following manner.

$$\begin{aligned} \Leftrightarrow 0 &= -\Big[rp^r p^\phi p^\phi \Big(r(\partial_r \xi^\phi) + 2(\xi^r - \xi^\phi)\Big) + p^r p^r p^r (\partial_r \xi^r) \\ &\quad + r^2 p^\phi p^\phi p^\phi (\partial_\phi \xi^\phi) + p^r p^r p^\phi (\partial_\phi \xi^r)\Big] \end{aligned} \tag{2.5.2}$$

Since we want to identify the "radial temperature" as the temperature of the radial particle spectrum, we choose $\xi^r = 0$. In addition we simplify the equation (2.5.2) by demanding $\xi^\phi = \xi^\phi(r)$. Which means that the anisotropy parameter depends only on the radial distance, not on the polar angle ϕ. We do this since we want to keep the symmetry with respect to the polar angle. Implementing the two above assumptions equation (2.5.2) converts into the following differential equation.

$$\begin{aligned} 0 &= -rp^r p^\phi p^\phi \Big(r(\partial_r \xi^\phi) - 2\xi^\phi\Big) \\ \Leftrightarrow r\partial_r \xi^\phi &= 2\xi^\phi \\ \Leftrightarrow \quad \xi^\phi &= \alpha r^2 \end{aligned} \tag{2.5.3}$$

This is the solution for the anisotropy parameter under the above assumptions. Where α denotes a constant, due to the fact that we solved a differential equation. For physical reasons let us choose α in equation (2.5.3) to be proportional to the inverse value of a typical length R squared, therefore the anisotropy parameter ξ^ϕ is a dimensionless parameter. With this we get a final expression for the anisotropy parameter ξ^ϕ.

$$\xi^\phi = \frac{r^2}{R^2} \tag{2.5.4}$$

2.5.2. Phenomenology of the anisotropic free streaming solution

Now we insert the computed anisotropy parameter (2.5.4) and $\xi^r = 0$ into the Romatschke-Strickland ansatz of the distribution function (2.5.1). Further we rename the parameter Λ by T, but we have to keep in mind that this is only a thermodynamical temperature in the case of isotropy. All in all our elaborated free streaming solution in the transverse plane at mid rapidity looks as follows.

$$F_{fs}(x^\mu, p^i) = Ce^{-\sqrt{\frac{m^2}{T^2} + \frac{p^r p^r}{T^2} + \left(1 + \frac{r^2}{R^2}\right) \frac{r^2 p^\phi p^\phi}{T^2}}} \tag{2.5.5}$$

In equation (2.5.5) one can identify the so called "effective anisotropic temperature" for the ϕ-direction T_ϕ as:

$$\frac{T}{\sqrt{1 + \frac{r^2}{R^2}}} = T_\phi \tag{2.5.6}$$

This is motivated by the fact that T_ϕ is the factor multiplying the p^ϕ-component in the same way as the "normal temperature" does in an isotropic system. Therefore one can

deduce that in the heavy-ion collision scenario the radial temperature freezes out and can be measured as the temperature of the particle spectrum[18]. Typically this temperature can be extracted from the inverse slope parameter of measured particle spectra. But as r/R increases along the radial expansion, the effective temperature for the ϕ-component decreases with distance to the starting point of this kinetic model in a smooth way.

Please keep in mind, that up to now our scenario is the following: First we assume the system to be in equilibrium, so that the right hand side of the Boltzmann equation vanishes. As one can see in the case where $r \ll R$ the distribution function is the (isotropic) Jüttner distribution. Then - more or less suddenly - we want the system to expand in a way, that the drift term (left hand side) of the Boltzmann equation is solved. We are now able to perform a transition from the equilibrium Jüttner solution to a radially free streaming solution under the condition that the collision term keeps vanishing during this transition. This transition is realized in a smooth way during the radial expansion.

Of course it would be interesting to see how the free streaming solution F_{fs} would be affected by a collision term. But we do this later. First we are going to investigate physical observables that emerge from the solution F_{fs} (2.5.5).

[18]This is due to the assumption on ξ^r we did between equation (2.5.2) and equation (2.5.3).

2.6. Interlude Hydrodynamics

Hydrodynamics is already for a long time a central element in the modeling of heavy-ion collisions. Over the years there were plenty of new concepts included to optimize the description of heavy-ion collisions via hydrodynamics. Hydrodynamics by itself is an effective field theory, which describes the system evolution on the basis of a few effective fields, instead of tracing all particles trajectories. Therefore this theory is still applicable, when a microscopical theory is no longer appropriate. This is due to the fact that one does not need to know the effective degrees of freedom nor the too high amount of particles. In this short summary we will concentrate on the relativistic formulation of hydrodynamics. For an almost complete classical hydrodynamical textbook the reader is referred to [33]. For a detailed introduction in relativistic hydrodynamics we recommend [34]. For a review for applying hydrodynamics in heavy-ion collisions we refer to [35].

Basically hydrodynamics consists of a field formulation of particle and energy-momentum conservation. Thus it has a very wide range of applicability ranging from geotectonics up to the movement of a bacteria. In order to work within the framework of hydrodynamics one has first to define a volume – called the fluid cell –, which sets the smallest scale limit of the description. This has to be chosen in a way that the element is big enough in order that the quantity's value inside the volume, like particle number, does not fluctuate too much. But the scale can not be chosen too big since one wants the gradients over several fluid cells to be smooth. This smallest scale sets the limit of the description and has to be of course much bigger than the microscopical mean free path l_{mfp}. From now on all local quantities like for example the particle number density $n(t, \vec{x})$ are meant to be the quantity in the fluid cell located at $\vec{x}$. In addition the derivatives do have to respect this smallest scales, which means that they are comparing the adjacent fluid cells.

As already mentioned above hydrodynamics is a field theory, therefore throughout this chapter every variable has a dependence on the position space and time. However for the sake of clarity we will leave aside the notation of the spacetime dependence. The central equations of motion, which reflect the particle number conservation and the energy-momentum conservation are listed in the following five formulas[19].

$$d_\mu N_i^\mu = 0 \tag{2.6.1}$$
$$d_\mu T^{\mu\nu} = 0^\nu \tag{2.6.2}$$

In the above equations the vector N_i^μ denotes the particle four-current for particles of type i, whereas $T^{\mu\nu}$ symbolizes the energy momentum tensor, which is symmetric in the indexes μ and ν. By the notation of the second equation it is stressed, that – if only one particle sort is present – these are five equations. In the case that there are b kinds of conserved particles in a system, one has to deal with $4+b$ equations. After counting the number of components, which have to be determined in (2.6.1) and (2.6.2) one realizes that this number is high. Namely there are $4 \cdot b$ - components from the particle currents and 10 components from the symmetric energy momentum tensor. Since it is impossible to solve a system of five equations for 14 variables, we have to search for further justifiable assumptions and equations.

A common way to decompose the hydrodynamical objects is shown in detail in the following.

[19] Note that formula (2.6.1) is one equation and expression (2.6.2) are four equations, since ν runs from 0 to 3.

$$N_i^\mu = n_i u^\mu + \nu_i^\mu \tag{2.6.3}$$
$$T^{\mu\nu} = \epsilon u^\mu u^\nu - (\mathcal{P} + \Pi)\,\Delta^{\mu\nu} + q^\mu u^\nu + q^\nu u^\mu + \varpi^{\mu\nu} \tag{2.6.4}$$

These equations have to be supplemented by the following equations for the various fields.

$$u_\mu u^\mu = 1 \tag{2.6.5}$$
$$\Delta^{\mu\nu} = (u^\mu u^\nu + g^{\mu\nu}) \tag{2.6.6}$$
$$u^\mu \nu_\mu = 0 \tag{2.6.7}$$
$$u^\mu q_\mu = 0 \tag{2.6.8}$$
$$\varpi^{\mu\nu} = \varpi^{\nu\mu} \tag{2.6.9}$$
$$g_{\mu\nu}\varpi^{\mu\nu} = 0 \tag{2.6.10}$$

Here a lot of new objects are arising, which can be attached to physical quantities. To do so we restrict the description of the system to the assumption that the fluid element is described in its local rest frame (LRF). This LRF is a reference frame, where the fluid cell under investigation is at rest. Due to the fact that in relativistic hydrodynamics all (vector)-fields are constructed in such a way, that they transform properly under Lorentz boosts, equations are formulated in the LRF and afterwards boosted into the experimental relevant reference frame. The same procedure is applied the other way round, when one wants to solve the hydrodynamical equations. In this case its local velocity field reads due to (2.6.5) like:

$$u_{LRF} = \begin{pmatrix} 1 \\ 0 \\ 0 \\ 0 \end{pmatrix} \tag{2.6.11}$$

In this frame one can identify a couple of thermodynamical quantities in the system. The n_i in formula (2.6.3) is meant to be the particle density in the fluid element, whereas the four-vector ν_i^μ is the so called particle flux, which is the number of particles escaping in that instant from the considered fluid cell. The vector u^μ, which is normalized due to (2.6.5), is denoting the fluid four velocity. This vector field indicates the local fluid cell's velocity with respect to some reference frame. For simplicity let us from now on assume that there is at most only one particle species in the system, like we did already while dealing with the Boltzmann equation.

Let us count the number of independent components in this case. For the flow velocity there are only 3 independent components due to the normalization. The same holds for the flux field ν^μ. In addition we have to consider the orthogonality between the flow velocity and the particle flux, which is denoted in formula (2.6.7).

The scalar field ϵ in equation (2.6.4) is the local energy density. $\mathcal{P}$ can be interpreted as the thermodynamic pressure, which is imposed by the fluid cell to its neighboring cells. The second term in the brackets, namely the Π is the dissipative pressure, which is a scalar dissipative quantity. In contrast q^μ is a rank 1 dissipative quantity. It can be interpreted as the dissipating energy flowing out from the local fluid cell. Therefore q^μ is called the

energy flux. The rank 2 dissipative tensor $\varpi^{\mu\nu}$ mimics dissipative effects, which for example contains the – in heavy-ion research highly investigated – shear viscous term. This term models the effect of flow in a direction becomes dissipated in another direction. The second rank tensor $\varpi^{\mu\nu}$ has to be symmetric in it's indices, since the energy momentum tensor is symmetric. Throughout the introduction of Π, this tensor can be constructed with a vanishing trace as well (2.6.10). In addition the product of $\varpi^{\mu\nu}$ with the flow velocity u^μ gives the energy flux. All in all there are 5 independent components in $\varpi^{\mu\nu}$ and q^μ. Adding the other independent components for ϵ, $\mathcal{P}+\Pi$ and u^μ one ends up with $5+1+1+3=10$ independent components again.

It can be checked that $\Delta^{\mu\nu}$ is a projector, which projects onto the 'volume' orthogonal to the flow velocity u^μ. Therefore the above decompositions (2.6.3) and (2.6.4) did not change the number of components, which have to be determined.

Note that equations (2.6.7) to (2.6.10) are requirements on the dissipative fields. In the case that there are no dissipative effects in the system, the fields ν^μ, Π, q^μ and $\varpi^{\mu\nu}$ vanish.

A crucial point is the choice of the reference frame. There are two choices which simplify the hydrodynamical formulas. One option is to demand that u^μ describes the flow of particles. In this case the rank 1 dissipative tensor ν^μ in (2.6.3) is vanishing by definition. This reference frame is called Eckart–frame [36]. Written in a formula the flow velocity in the Eckart–frame has the following definition.

$$u^\mu_{Eckart} = \frac{N^\mu}{\sqrt{N^\alpha N_\alpha}}$$

The other choice for the fluid velocity is the flow of energy. Consequently in this case, called Landau–frame, the q^μ factors vanish [33]. Since the flow velocity follows the flow of energy, it is the eigenvector of the energy momentum tensor $T^{\mu\nu}$:

$$\epsilon\, u^\mu_{Landau} = T^\mu_{\ \nu} u^\nu_{Landau}$$

Note that these two frames differ, due to the fact that in a relativistic theory energy can be transported for example via heat, but also via particles. In the case of no dissipative effects the frames are equivalent.

2.6.1. Moments of the distribution function

Assuming that one knows the microscopical degrees of freedom, their phase space distribution $f(x^\mu, p^i)$ as well as all relevant cross sections, or in other words one has a kinetic microscopical model at hand, it is possible to construct all the above mentioned objects out of this. In principle this should be possible since the hydrodynamical description is per definition an averaging theory. Technically this is done by computing the so called moments of the Boltzmann equation. In the absence of external fields this construction works like the following.

For the particle conservation one forms the so called 0^{th} -moment of the Boltzmann equation via integrating the Boltzmann equation over the on shell momentum space measure, which we elaborated in formula (2.3.26).

$$\begin{aligned}
\int \frac{d^3\vec{p}}{2\tau r p^\tau} p^\mu \partial_\mu f(x^\mu, p^i) &= \int \frac{d^3\vec{p}}{2\tau r p^\tau} \left(\frac{df}{dt}\right)_{Coll} \\
\int \frac{dp^r r dp^\phi \tau dp^{\eta_s}}{2\tau r p^\tau} p^\mu \partial_\mu f(x^\mu, p^i) &= 0 \\
\Leftrightarrow \partial_\mu \int \frac{d^3\vec{p}}{2\tau r p^\tau} p^\mu f(x^\mu, p^i) &= 0 \\
\Leftrightarrow \partial_\mu N^\mu &= 0
\end{aligned} \tag{2.6.12}$$

Note that we used the fact, that the collision term should conserve the particle number. Out of formula (2.6.12) one can extract the particle four current N^μ to be:

$$N^\mu = \int \frac{d^3\vec{p}}{2\tau r p^\tau} p^\mu f(x^\mu, p^i) \tag{2.6.13}$$

Similarly one computes the 1^{st}-moment of the Boltzmann equation in order to obtain the energy momentum conservation:

$$\begin{aligned}
\left(\int \frac{d^3\vec{p}}{2\tau r p^\tau} p^\nu\right) p^\mu \partial_\mu f(x^\mu, p^i) &= \int \frac{d^3\vec{p}}{2\tau r p^\tau} p^\nu \left(\frac{df}{dt}\right)_{Coll} \\
\left(\int \frac{dp^r r dp^\phi \tau dp^{\eta_s}}{2\tau r p^\tau} p^\nu\right) p^\mu \partial_\mu f(x^\mu, p^i) &= \int \frac{d^3\vec{p}}{2\tau r p^\tau} p^\nu \left(\frac{df}{dt}\right)_{Coll} \\
\Leftrightarrow \partial_\mu \int \frac{d^3\vec{p}}{2\tau r p^\tau} p^\mu p^\nu f(x^\mu, p^i) &= 0 \\
\Leftrightarrow \partial_\mu T^{\mu\nu} &= 0
\end{aligned} \tag{2.6.14}$$

In this case the integral over the collision term vanishes, due to the fact that the microscopic collisions have to conserve energy and momentum. Again one can read out the definition of the hydrodynamical object $T^{\mu\nu}$, which turns out to be the following expression.

$$T^{\mu\nu} = \int \frac{d^3\vec{p}}{2\tau r p^\tau} p^\mu p^\nu f(x^\mu, p^i) \tag{2.6.15}$$

2.6.2. Ideal Hydrodynamics

With the definitions (2.6.13) and (2.6.15) one can now compute the hydrodynamics emerging from the Jüttner distribution (2.4.13). Since this is the equilibrium distribution, one assumes the described fluid to be in equilibrium. Note that the factor in the exponent of the first expression in (2.4.13) guarantees the right reference frame transformation behavior. Computing the fields provides the ideal hydrodynamics, where N^μ and $T^{\mu\nu}$ reads as the following.

$$N^\mu = n u^\mu \tag{2.6.16}$$

$$T^{\mu\nu} = \epsilon u^\mu u^\nu - \Delta^{\mu\nu}\mathcal{P} \tag{2.6.17}$$

As one can see while comparing equations (2.6.16) and (2.6.17) with (2.6.3) and (2.6.4), all the above dissipative elements are not present in the ideal hydrodynamical fields. This is the reason why these additional fields are called dissipative contributions. As a remark let us mention that in the ideal hydrodynamical case the number of fields that have to be determinded in the above tensors is $1(n) + 3(u^\mu) + 1(\epsilon) + 1(\mathcal{P}) = 6$. Even in ideal hydrodynamics there is one field more to be detemined than there are equations on hand. But one is able to close the system of equations with an additional equation of state, which relates the (thermodynamic) energy density ϵ and the thermodynamic pressure $\mathcal{P}$. Such an equation of state can be gained by assuming the system to be built up by an ultrarelativistic ideal gas, which gives $\epsilon = 3\mathcal{P}$. It is much more realistic – but also it is much more complicated – to gain such an equation of state via Lattice-QCD [37]. Figure 2.10 shows the outcome for a QCD based equation of state from the Hot-QCD-collaboration.

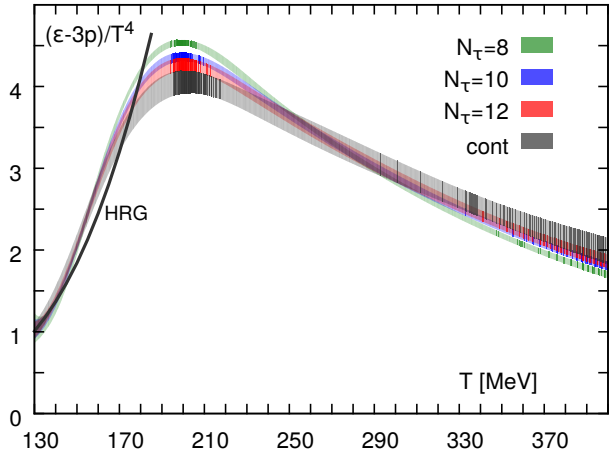

Figure 2.10.: Temperature dependent plot which relates energy density ϵ and pressure $\mathcal{P}$, while plotting the dimensionless so-called "trace anomaly" of the energy momentum tensor. Taken from [37].

With such an equation of state the system of equations is completely solvable, since the number of equations equals the number of to be determined fields.

In the local rest frame the components of the energy momentum tensor reads as follows.

$$T^{\mu\nu}_{LRF} = \begin{pmatrix} \epsilon & 0 & 0 & 0 \\ 0 & \mathcal{P} & 0 & 0 \\ 0 & 0 & \mathcal{P} & 0 \\ 0 & 0 & 0 & \mathcal{P} \end{pmatrix} \tag{2.6.18}$$

In addition the particle flow four vector in the LRF has the following form.

$$N^{\mu}_{LRF} = \begin{pmatrix} n \\ 0 \\ 0 \\ 0 \end{pmatrix} \tag{2.6.19}$$

2.6.3. Viscous Hydrodynamics

As we saw in chapter 2.4.2 there are several formalisms to model a deviation from local or global equilibrium. At the end of the chapter the concept of linearization was introduced. To construct the hydrodynamical fields for a system, which is not already in equilibrium the easiest ansatz is the linearization (2.4.10). Since the correction is additive, the integral for computing (2.6.12) and (2.6.14) will lead to additive contributions.

$$N^{\mu} = N^{\mu}_{eq} + \delta N^{\mu} \tag{2.6.20}$$
$$T^{\mu\nu} = T^{\mu\nu}_{eq} + \delta T^{\mu\nu} \tag{2.6.21}$$

Through a comparison with the decomposition (2.6.3) and (2.6.4) one can identify:

$$\delta N^{\mu} = \nu^{\mu} \tag{2.6.22}$$
$$\delta T^{\mu\nu} = q^{\mu}u^{\nu} + q^{\nu}u^{\mu} + \varpi^{\mu\nu} := \pi^{\mu\nu} \tag{2.6.23}$$

In addition one can compute the various dissipative contributions via various projections, which reads:

$$\Pi = -\frac{1}{3}\Delta_{\mu\nu}T^{\mu\nu} - \mathcal{P} \tag{2.6.24}$$
$$\nu^{\mu} = \Delta^{\mu}_{\ \rho}N^{\rho} \tag{2.6.25}$$
$$q^{\mu} = \Delta^{\mu}_{\ \rho}T^{\rho\nu}u_{\nu} \tag{2.6.26}$$
$$\varpi^{\mu\nu} = \left(\frac{1}{2}\left(\Delta^{\mu}_{\rho}\Delta^{\nu}_{\gamma} + \Delta^{\nu}_{\rho}\Delta^{\mu}_{\gamma}\right) - \frac{1}{3}\Delta^{\mu\nu}\Delta_{\rho\gamma}\right)T^{\rho\gamma} := T^{\langle\mu\nu\rangle} \tag{2.6.27}$$

If one chooses the Landau frame for the flow velocity one can get rid of expression (2.6.26). While inserting the above expressions for N^{μ} and $T^{\mu\nu}$ one can show that only the additive corrections δN^{μ} and $\delta T^{\mu\nu}$ will contribute to the dissipation, since the ideal hydrodynamical components vanish due to the projection. Nevertheless as already mentioned above there are still 9 more dissipative contributions arising.

Since there are more terms that need to be determined, it is important to gain more equations in order to close the system of equations again. A way how this can be achieved is presented for example in the lectures [34]. If the reader prefers to read the original publication we refer to the DNMR paper [31]. Hereafter we will only sketch the main concepts. The basic idea is to employ microscopic dynamics in order to work out more equations. As in the 1^{st} linerarization case one models a generalized force, which generates the dissipative flows (2.6.24) to (2.6.27). For symmetry reasons – since there has to exist such a force for every dissipative effect – there have to be various "generalized forces", namely one for every tensorial rank at play. Phenomenologically these generalized forces have to arise from gradients of hydrodynamical fields between neighboring fluid cells. Written in formulas these forces look like the following expressions.

$$\Theta = \partial_\mu u^\mu \tag{2.6.28}$$
$$I^\mu = \nabla^\mu \left(\frac{\mu}{T}\right) \tag{2.6.29}$$
$$\sigma^{\mu\nu} = \nabla^{\langle\mu} u^{\nu\rangle} \tag{2.6.30}$$
$$\omega^{\mu\nu} = \frac{1}{2}\left(\nabla^\mu u^\nu - \nabla^\nu u^\mu\right) \tag{2.6.31}$$

The quite extensive work to do now is to relate how the dissipative flows emerge as an answer to the forces, which are themselves originated by gradients of the hydrodynamical fields again. The crucial point to realize is that we did not introduce new fields, but used just gradients of already "established" fields. Which means that we have more equations (and more boundary conditions), but the same number of fields as before.

Please note that we are now implicitly dealing with at least two, in general independent, numbers. One was – due to it's importance in kinetic theory – already mentioned several times, namely the Knudsen number. This is "hidden" in the dynamics for the dissipative currents. Since we linearized several times in our model we would be able to compute linear contributions in Kn. The other transport number(s) is (are) the inverse Reynolds number, defined as

$$R_\Pi^{-1} = \frac{|\Pi|}{\mathcal{P}},\ R_\nu^{-1} = \frac{|\nu^\mu|}{n},\ R_\pi^{-1} = \frac{|\pi|}{\mathcal{P}} \tag{2.6.32}$$

These numbers are a measure for the deviation from the local equilibrium state and can be in general different from each others.

With the above ingredients one can now start computations. In the DNMR formalism the authors developed a way to treat the systems evolution in a systematic expansion in Kn and Re^{-1} [31]. Here let us just mention that in a specific limit, namely the relativistic Navier-Stokes formulation, one can identify the dissipative fields as a response for the forces to look like the following.

$$\Pi = -\xi\ \Theta \tag{2.6.33}$$
$$\nu^\mu = \kappa\ I^\mu \tag{2.6.34}$$
$$\pi^{\mu\nu} = 2\ \eta\ \sigma^{\mu\nu} \tag{2.6.35}$$

Here the (transport)-coefficients ξ, κ and η are the bulk viscosity, the heat conductivity and the shear viscosity. They are general properties of the medium. The most investigated transport coefficient is η. To be precise people look for values of the dimensionless ratio η/s.

Like the equation of state, in principle it would be useful to compute these coefficients from a microscopical theory, like Lattice-QCD. However it turns out, that this is a hard task to do. Therefore physicists often use this parameter η/s as a fit parameter in order to reproduce experimental data [38].

Another way to compute a value for η/s is the AdS/CFT-correspondence. This correspondence gives a value in the case that QCD would be described by an infinite-strongly coupled theory with an infinite number of colors, which is $1/4\pi$. This value is often argued to set the overall lower bound for the shear viscosity over entropy ratio.

Indeed values extracted from the mentioned fit procedure of dissipative hydrodynamics

tend to be near this lower bound. This is why the QGP is referred to be the most perfect fluid. Please keep in mind that the fact of a small η/s-value does not imply a small value for the shear viscosity. Due to the fact that the entropy density in the QGP is extremely high, the value for the shear viscosity is rather large.

2.6.4. Anisotropic Hydrodynamics

The formalism of anisotropic hydrodynamics is rather new and still in development. Since we explained the motivations for this formalism already in section 2.1, we just give a brief mathematical derivation here. One derives the hydrodynamical fields for anisotropic hydrodynamics by computing the moments of the Romatschke-Strickland distribution (2.5.1). In the original formulation to mimic the anisotropy at the very beginning of the hydrodynamical regime the anisotropy is chosen to point in the direction of the beam. Thus the distribution is written down in the following expression.

$$f_{anhy} = Ce^{\frac{1}{\Lambda}\sqrt{p^2+\xi(p^z)^2}} \tag{2.6.36}$$

Here the ξ denotes the anisotropy parameter, which we already saw before. Let us emphasize at this point again that Λ acts like a temperature in the case of isotropy, therefore it is called anisotropic temperature. Computing the moments of this distribution function f_{anhy} one ends up with the following energy momentum tensor in the local rest frame.

$$T^{\mu\nu}_{lrf} = \begin{pmatrix} \epsilon & 0 & 0 & 0 \\ 0 & \mathcal{P}^t & 0 & 0 \\ 0 & 0 & \mathcal{P}^t & 0 \\ 0 & 0 & 0 & \mathcal{P}^z \end{pmatrix} \tag{2.6.37}$$

In the above energy momentum tensor $\mathcal{P}^t$ denotes the transversal pressure component and $\mathcal{P}^z$ denotes the longitudinal component. Since we are not in an isotropic state, strictly speaking we can not apply thermodynamics anymore. Due to this fact one has no equation of state at hand. It is important as well to realize, that we introduced a new field, which has to be determined, namely ξ. In order to close the system of equations again, we refer the reader to [39].

The advantage of the anisotropic hydrodynamical framework is that it is claimed to treat the largest dissipative correction as resumed in the exponential function. Due to this fact it is already applicable in a region, where viscous hydrodynamics is not valid since there the δf-term in (2.4.10) would be too large. The last point we want to remark here is, that one can proceed further and take into account linear perturbations $\delta\tilde{f}$ as well. But since the z-components are already taken into account in the zeroth order, this $\delta\tilde{f}$ is not the same as the δf in (2.4.10). This makes the whole formalism a lot more complicated, but it was carried out, for example in [40].

Be aware that typical values for η/s arising from anisotropic hydrodynamical-fits to data are in general larger than those from viscous hydrodynamics [15]. Which means that they are not that near to the values extracted from an infinitely strongly coupled theory anymore.

2.6.5. Hydrodynamics including sources

A very recent development in the framework of hydrodynamics is the hydrodynamical framework including dynamical sources which is presented in [41] or in proceedings form [42] or [43]. This development is necessary due to the fact that – in order to describe the BES data properly – one needs to take into account the dynamical feeding-in of baryon-number as well as their energy and momentum. Such a feeding-in is necessary since the nucleons can be stopped, because their initial kinetic energy is much smaller than in ultra relativistic heavy-ion collisions. After being stopped their Baryon number and their energy and momentum contribute to the medium content. This can be modeled via the following formulas.

$$d_\mu N^\mu_{fluid} = \rho_{source} = -d_\mu N^\mu_{Bary} \tag{2.6.38}$$

$$d_\mu T^{\mu\nu}_{fluid} = J^\nu_{source} = -d_\mu T^{\mu\nu}_{Bary} \tag{2.6.39}$$

Here the particle fields – indicated by the index "Bary" – are simulated dynamical via an initial stage kinetic model, like for example URQMD[20].

2.7. Moments of the anisotropic free streaming solution for massless particles

In this section we are going to compute the hydrodynamic fields which arise from our new free-streaming distribution F_{fs}. Traditionally equation (2.6.13) is called the first moment of the distribution function. Whereas (2.6.15) is the second moment of the distribution function. The labeling refers to the powers of p^μ as weight. Of course one could build up higher moments as well. These higher moments are key-ingredients in the DNMR formalism[21]. For us this is not necessesary, since these higher moments are not directly related to a hydrodynamical field. But these higher moments are very promissing in order to get a closed system of equations in the formalism of anisotropic hydrodynamics, as it is done in [39] or in the proceedings [45].

2.7.1. Useful substitutions

In order to keep the computations as well-arranged as possible we want to list a few substitutions. This will enable us to keep the computation of the afterwards following integrals more compact.

The first substitution merges the temperature, the momentum component and the possible metric contribution in one variable in order to create a clean exponent.

$$q^{\eta_s} \equiv \frac{\tau}{T} p^{\eta_s} \quad \Rightarrow \quad dp^{\eta_s} = \frac{T}{\tau} dq^{\eta_s} \tag{2.7.1}$$

$$q^{\phi} \equiv \frac{r\sqrt{1+\frac{r^2}{R^2}}}{T} p^{\phi} \quad \Rightarrow \quad dp^{\phi} = \frac{T}{r\sqrt{1+\frac{r^2}{R^2}}} dq^{\phi} \tag{2.7.2}$$

$$q^{r} \equiv \frac{1}{T} p^{r} \quad \Rightarrow \quad dp^{r} = T dq^{r} \tag{2.7.3}$$

[20] URQMD stands for ultra relativistic quantum molecular dynamics [44].
[21] Although they are employing a secondary weight in energy as well.

The second substitution which we will frequently use, is a transformation in spherical coordinates in order to further simplify the exponent.

$$q^{\phi} \equiv |q^r| \cos(\theta_q) \tag{2.7.4}$$
$$q^{r} \equiv |q^r| \sin(\theta_q) \cos(\phi_q) \tag{2.7.5}$$
$$q^{\eta_s} \equiv |q^r| \sin(\theta_q) \sin(\phi_q) \tag{2.7.6}$$

Since we perform a transformation into spherical coordinates we have to transform the measures in the usual manner as well.

$$\int_{-\infty}^{\infty} dq^r \int_{-\infty}^{\infty} dq^{\phi} \int_{-\infty}^{\infty} dq^{\eta_s} \Rightarrow \int_0^{\infty} d|q^r| \int_0^{2\pi} d\phi_q \int_0^{\pi} d\theta_q |\ q^r|^2 \sin(\theta_q) \tag{2.7.7}$$

2.7.2. Moments of the massless anisotropic free streaming distribution F_{fs}

In this subsection we present the different moments of the anisotropic free streaming distribution function (2.5.5), which results in components of the hydrodynamical fields (2.6.13) and (2.6.15). We are first dealing with massless particles, because in that case the integrals are analytically solvable.

2.7.3. 0^{th}-moment of the free streaming distribution $F_{fs}(x^{\mu}, p^i)$

In the following we will present the computation for the zeroth component in detail. For the presented integrals afterwards we will not explain the same steps again, but rather denote them during the computation.

$$I_0 \equiv \int \frac{d^3p}{2\tau r p^{\tau}} F_{fs}(x^{\mu}, p^i)$$

Inserting the distribution function (2.5.5) leads to the following.

$$I_0 = \frac{C}{2} \int dp^r dp^{\phi} dp^{\eta_s} \frac{e^{-\sqrt{\frac{p^r p^r}{T^2} + \frac{r^2\left(1+\frac{r^2}{R^2}\right)p^{\phi}p^{\phi}}{T^2} + \frac{\tau^2 p^{\eta_s} p^{\eta_s}}{T^2}}}}{\sqrt{p^r p^r + r^2 p^{\phi} p^{\phi} + \tau^2 p^{\eta_s} p^{\eta_s}}}$$

In order to simplify the exponent we employ the substitutions (2.7.1) - (2.7.3) for the momentum components.

$$I_0 = \frac{CT^3}{2\tau r\sqrt{1+\frac{r^2}{R^2}}} \int dq^r dq^{\eta_s} dq^{\phi} \frac{e^{-\sqrt{q^r q^r + q^{\phi} q^{\phi} + q^{\eta_s} q^{\eta_s}}}}{T\sqrt{q^r q^r + \frac{q^{\phi} q^{\phi}}{(1+\frac{r^2}{R^2})} + q^{\eta_s} q^{\eta_s}}}$$

Now we can switch to the spherical coordinates (2.7.4) - (2.7.6), in order to simplify the integral further.

$$I_0 = \frac{CT^2}{2\tau r\sqrt{1+\frac{r^2}{R^2}}}\int_0^\infty d|q^r|\int_0^{2\pi}d\phi_q\int_0^\pi d\theta_q \frac{|q^r|^2\sin(\theta_q)e^{-|q^r|}}{|q^r|\sqrt{\sin^2(\theta_q)+\frac{\cos^2(\theta_q)}{(1+\frac{r^2}{R^2})}}}$$

At this point we can solve the $|q^r|$- and the ϕ_q-integral.

$$I_0 = \frac{\pi CT^2}{\tau r\sqrt{1+\frac{r^2}{R^2}}}\int_0^\pi d\theta_q \frac{\sin(\theta_q)}{\sqrt{\frac{(1+\frac{r^2}{R^2})\sin^2(\theta_q)+\cos^2(\theta_q)}{(1+\frac{r^2}{R^2})}}}$$

Now one can perform the θ_q integral as well.

$$\begin{aligned} I_0 &= \frac{\pi CT^2}{\tau r}\int_0^\pi d\theta_q \frac{\sin(\theta_q)}{\sqrt{1+\frac{r^2}{R^2}\sin^2(\theta_q)}} = \frac{\pi CT^2}{\tau r}\frac{2\arctan(\frac{r}{R})}{\frac{r}{R}} \\ &= \frac{2\pi CT^2 R}{\tau r^2}\arctan\left(\frac{r}{R}\right) \end{aligned} \tag{2.7.8}$$

Formula (2.7.8) is the zeroth moment of the free streaming solution (2.5.5). Unfortunately, this zeroth moment can not be related to a hydrodynamical field. However, since this is the easiest integral one can follow the individual steps to solve the integrals best in this case. In addition one can show, via using L'Hôpital's rule, that in the limit of vanishing anisotropy r/R the above moment coincides with the zeroth moment computed from a massless Jüttner distribution. This behavior guarantees a smooth transition of an isotropic system to an anisotropic free streaming system.

In the following the arising integrals will be computed in the same way as in the above case. In addition one can extract physical phenomena from all the following integrals in the sense that we can relate them to hydrodynamical field components.

2.7.4. 1^{st}-moment of the free streaming distribution $F_{fs}(x^\mu, p^i)$ wrt. p^τ

$$
\begin{aligned}
n \quad &= \quad N^\tau = \int \frac{d^3p}{2\tau r p^\tau} p^\tau F_{fs}(x^\mu, p^i) \\
&= \quad \frac{C}{2} \int dp^r dp^\phi dp^{\eta_s} e^{-\sqrt{\frac{p^r p^r}{T^2} + \frac{r^2\left(1+\frac{r^2}{R^2}\right)p^\phi p^\phi}{T^2} + \frac{\tau^2 p^{\eta_s} p^{\eta_s}}{T^2}}} \\
&\overset{(2.7.1)-(2.7.3)}{=} \quad \frac{CT^3}{2\tau r\sqrt{1+\frac{r^2}{R^2}}} \int dq^r dq^\phi dq^{\eta_s} e^{-\sqrt{q^r q^r + q^\phi q^\phi + q^{\eta_s} q^{\eta_s}}} \\
&\overset{(2.7.4)-(2.7.6)}{=} \quad \frac{2\pi CT^3}{\tau r\sqrt{1+\frac{r^2}{R^2}}} \int_0^\infty d|q^r| |q^r|^2 e^{-|q^r|} \\
&= \quad \frac{4\pi CT^3}{\tau r\sqrt{1+\frac{r^2}{R^2}}} \\
&= \quad \frac{1}{\sqrt{1+\frac{r^2}{R^2}}} n_{iso}
\end{aligned}
\tag{2.7.9}
$$

As one can see, the particle density grows with T^3, which should due to dimensional reasons be the case. Further it is guaranteed that the particle density is vanishing in the limit of $r \to \infty$. This should be the case in our setup, where a central source is emitting particles in the radial direction. Due to the longitudinal expansion in η_s-direction the density is also decreasing with time τ.

The effect of the anisotropy is a dilution of the particle density, with increasing value of r/R. In order to emphasize this fact, we did the last step of the computation, where n_{iso} is the particle density which would arise from computing the p^τ-moment from a massless Jüttner distribution (2.4.13) in the proper symmetry.

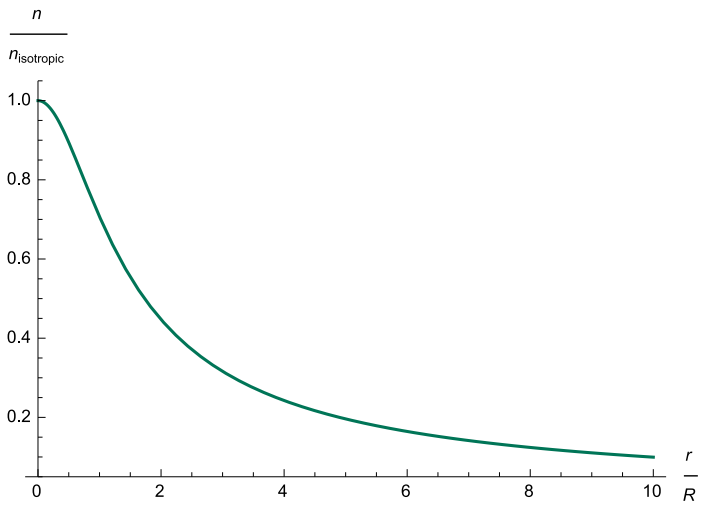

Figure 2.11.: Plot of the ratio n/n_{iso} over the anisotropy parameter r/R.

Figure 2.11 shows the effect of the anisotropy parameter r/R on the ratio of the computed

particle density over the isotropic particle density. As one can see the ratio is rapidly decreasing with increasing r/R. For an anisotropy parameter of around ten, the density already dropped one order of magnitude, compared to the isotropic system. Though at vanishing anisotropy the two densities are equivalent.

2.7.5. 1^{st}-moment of the free streaming distribution $F_{fs}(x^\mu, p^i)$ wrt. p^r

$$
\begin{aligned}
N^r &= \int \frac{d^3p}{2\tau r p^\tau} p^r F_{fs}(x^\mu, p^i) \\
&= \frac{C}{2}\int dp^r dp^\phi dp^{\eta_s} \frac{p^r \; e^{-\sqrt{\frac{p^r p^r}{T^2} + \frac{r^2\left(1+\frac{r^2}{R^2}\right)p^\phi p^\phi}{T^2} + \frac{\tau^2 p^{\eta_s} p^{\eta_s}}{T^2}}}}{\sqrt{p^r p^r + r^2 p^\phi p^\phi + \tau^2 p^{\eta_s} p^{\eta_s}}} \\
&\overset{(2.7.1)-(2.7.3)}{=} \frac{CT^3}{2\tau r\sqrt{1+\frac{r^2}{R^2}}} \int dq^r dq^\phi dq^{\eta_s} \frac{T q^r e^{-\sqrt{q^r q^r + q^\phi q^\phi + q^{\eta_s} q^{\eta_s}}}}{T\sqrt{q^r q^r + \frac{q^\phi q^\phi}{1+\frac{r^2}{R^2}} + q^{\eta_s} q^{\eta_s}}} \\
&\overset{(2.7.4)-(2.7.6)}{=} \frac{CT^3}{2\tau r\sqrt{1+\frac{r^2}{R^2}}} \int_0^\infty d|q^r| \int_0^\pi d\theta_q \int_0^{2\pi} \underline{d\phi_q} \frac{|q^r|^2 \sin^2(\theta_q)\underline{\cos(\phi_q)} \; e^{-|q^r|}}{\sqrt{\sin^2(\theta_q) + \frac{\cos^2(\theta_q)}{1+\frac{r^2}{R^2}}}} \\
&= 0 \qquad (2.7.10)
\end{aligned}
$$

The last step is due to the fact that the ϕ_q-integral vanishes[22]. All the spatial components of the particle current vanish. This is due to the fact that the free streaming distribution function $F_{fs}(x^\mu, p^i)$ is even in the p components. Thus integrating an even function multiplied by an odd one – namely p^i – over a symmetric interval for symmetry reasons ends up in a contribution which is zero. Of course this statement holds for the other moments with respect to p^ϕ and p^{η_s} as well. Therefore we find analog to the above computation that the other spacial components of the four current are vanishing.

$$N^r = N^\phi = N^{\eta_s} = 0 \qquad (2.7.11)$$

Comparing this findings of equation (2.7.11) to the discussion about dissipative hydrodynamics in chapter 2.6 one can deduce that there are no particle fluxes at play. In other words there are no particles entering from outside the fluid cell.

2.7.6. 2^{nd}-moment of the free streaming distribution $F_{fs}(x^\mu, p^i)$ wrt. p^τ

Now that we have computed all the fields contributing to the particle four current, we can start to compute the second moments, which are contributing to the energy momentum tensor (2.6.15).

[22] As it is indicated by the underline.

$$
\begin{aligned}
\epsilon &= T^{\tau\tau} = \int \frac{d^3p}{2\tau r p^\tau} p^\tau p^\tau F_{fs}(x^\mu, p^i) \\
&= \frac{C}{2} \int dp^r dp^\phi dp^{\eta_s} \sqrt{p^r p^r + r^2 p^\phi p^\phi + \tau^2 p^{\eta_s} p^{\eta_s}} \\
&\quad e^{-\sqrt{\frac{p^r p^r}{T^2} + \frac{r^2\left(1+\frac{r^2}{R^2}\right) p^\phi p^\phi}{T^2} + \frac{\tau^2 p^{\eta_s} p^{\eta_s}}{T^2}}} \\
&\overset{(2.7.1)-(2.7.3)}{=} \frac{CT^3}{2\tau r \sqrt{1+\frac{r^2}{R^2}}} \int dq^r dq^\phi dq^{\eta_s} T \sqrt{q^r q^r + \frac{q^\phi q^\phi}{1+\frac{r^2}{R^2}} + q^{\eta_s} q^{\eta_s}} \\
&\quad e^{-\sqrt{q^r q^r + q^\phi q^\phi + q^{\eta_s} q^{\eta_s}}} \\
&\overset{(2.7.4)-(2.7.6)}{=} \frac{CT^4}{2\tau r \sqrt{1+\frac{r^2}{R^2}}} \int_0^\infty d|q^r| \int_0^\pi d\theta_q \int_0^{2\pi} d\phi_q |q^r|^3 \sin(\theta_q) \\
&\quad \sqrt{\sin^2(\theta_q) + \frac{\cos^2(\theta_q)}{1+\frac{r^2}{R^2}}} e^{-|q^r|} \\
&= \frac{\pi CT^4}{\tau r \sqrt{1+\frac{r^2}{R^2}}} \int_0^\infty d|q^r| |q^r|^3 e^{-|q^r|} \int_0^\pi d\theta_q \sin(\theta_q) \\
&\quad \sqrt{\sin^2(\theta_q) + \frac{\cos^2(\theta_q)}{1+\frac{r^2}{R^2}}} \\
&= \frac{6\pi CT^4}{\tau r \sqrt{1+\frac{r^2}{R^2}}} \int_0^\pi d\theta_q \sin(\theta_q) \sqrt{\sin^2(\theta_q) + \frac{\cos^2(\theta_q)}{1+\frac{r^2}{R^2}}} \\
&= \frac{6\pi CT^4}{\tau r \left(1+\frac{r^2}{R^2}\right)} \left(1 + \frac{R}{r}\left[1+\frac{r^2}{R^2}\right] \arctan\left(\frac{r}{R}\right)\right) \qquad (2.7.12) \\
&= \frac{\epsilon_{iso}}{\left(1+\frac{r^2}{R^2}\right)} \left(1 + \frac{R}{r}\left[1+\frac{r^2}{R^2}\right] \arctan\left(\frac{r}{R}\right)\right)
\end{aligned}
$$

As before we illustrate the gained expression for the energy density (2.7.12) by plotting the ratio over with respect to the isotropic density over the anisotropy.

Figure 2.12 displays the dependence of the ratio of local energy density over the isotropic local energy density on the ratio r/R. As one can see the ratio is decreasing with increasing anisotropy, which means that the free streaming energy density is decreasing faster due to the increasing anisotropy in the system.

Looking at equation (2.7.12) one sees that in addition the energy density decreases with time due to the system's expansion along the beam line. The energy density also decreases with increasing radius r, which is reasonable for a cylindrical symmetric system.

2.7.7. 2^{nd}-moment of the free streaming distribution $F_{fs}(x^\mu, p^i)$ wrt. p^r

Next we compute the rr-component of the energy momentum tensor. Afterwards we plot the functional dependence on the anisotropy parameter r/R.

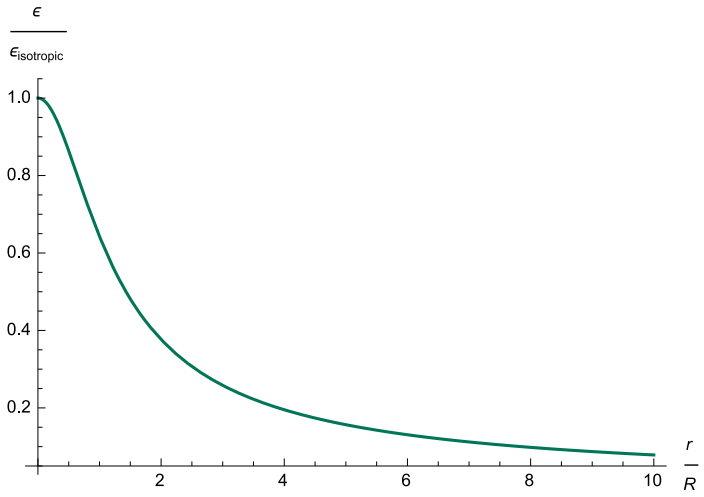

Figure 2.12.: Plot of the ratio ϵ/ϵ_{iso} over r/R.

$$
\begin{aligned}
\mathcal{P}^r \quad &= \quad T^{rr} = \int \frac{d^3p}{2\tau r p^\tau} p^r p^r F_{fs}(x^\mu, p^i) \\
&= \quad \frac{C}{2} \int dp^r dp^\phi dp^{\eta_s} \frac{p^r p^r e^{-\sqrt{\frac{p^r p^r}{T^2} + \frac{r^2\left(1+\frac{r^2}{R^2}\right) p^\phi p^\phi}{T^2} + \frac{\tau^2 p^{\eta_s} p^{\eta_s}}{T^2}}}}{\sqrt{p^r p^r + r^2 p^\phi p^\phi + \tau^2 p^{\eta_s} p^{\eta_s}}} \\
&\overset{(2.7.1)-(2.7.3)}{=} \quad \frac{CT^3}{2\tau r\sqrt{1+\frac{r^2}{R^2}}} \int dq^r dq^\phi dq^{\eta_s} \frac{T^2 q^r q^r e^{-\sqrt{q^r q^r + q^\phi q^\phi + q^{\eta_s} q^{\eta_s}}}}{T\sqrt{q^r q^r + \frac{q^\phi q^\phi}{1+\frac{r^2}{R^2}}}} \\
&\overset{(2.7.4)-(2.7.6)}{=} \quad \frac{CT^4}{2\tau r\sqrt{1+\frac{r^2}{R^2}}} \int_0^\infty d|q^r| \int_0^\pi d\theta_q \int_0^{2\pi} d\phi_q \frac{|q^r|^4 \sin^3(\theta_q)\cos^2(\phi_q) e^{-|q^r|}}{|q^r|\sqrt{\sin^2(\theta_q) + \frac{\cos^2(\theta_q)}{1+\frac{r^2}{R^2}}}} \\
&= \quad \frac{3\pi C T^4}{\tau r} \int_0^\pi d\theta_q \frac{\sin^3(\theta_q)}{\sqrt{1+\frac{r^2}{R^2}\sin^2(\theta_q)}} \\
&= \quad \frac{3\pi C T^4}{\tau r} \frac{R^2}{r^2} \left[1 + \frac{R}{r}\left(\frac{r^2}{R^2} - 1\right) \arctan\left(\frac{r}{R}\right)\right] \qquad (2.7.13) \\
&= \quad \alpha \frac{R^2}{r^2} \left[1 + \frac{R}{r}\left(\frac{r^2}{R^2} - 1\right) \arctan\left(\frac{r}{R}\right)\right]
\end{aligned}
$$

In the last step we defined the first ratio of equation (2.7.13) to be α in order to plot the functional dependence of the radial pressure component on the ratio r/R, which is shown in the following figure 2.13.

2.7.8. 2^{nd}-moment of the free streaming distribution $F_{fs}(x^\mu, p^i)$ wrt. p^ϕ

This brings us to compute the $\phi\phi$- component of the energy momentum tensor $T^{\mu\nu}$.

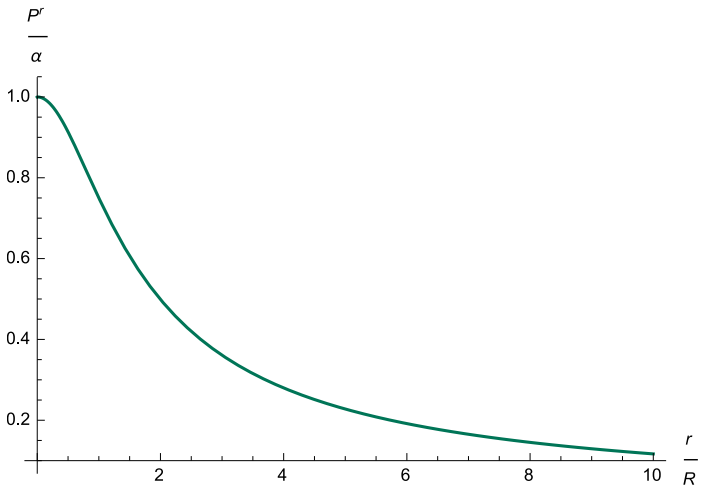

Figure 2.13.: Plot of the ratio $\mathcal{P}^r/\alpha$ over r/R.

$$
\begin{aligned}
\frac{\mathcal{P}^\phi}{r^2} &= T^{\phi\phi} = \int \frac{d^3p}{2\tau r p^\tau} p^\phi p^\phi F_{fs}(x^\mu, p^i) \\
&= \frac{C}{2} \int dp^r dp^\phi dp^{\eta_s} \frac{p^\phi p^\phi e^{-\sqrt{\frac{p^r p^r}{T^2} + \frac{r^2\left(1+\frac{r^2}{R^2}\right) p^\phi p^\phi}{T^2} + \frac{\tau^2 p^{\eta_s} p^{\eta_s}}{T^2}}}}{\sqrt{p^r p^r + r^2 p^\phi p^\phi + \tau^2 p^{\eta_s} p^{\eta_s}}} \\
&\overset{(2.7.1)-(2.7.3)}{=} \frac{CT^3}{2\tau r\sqrt{1+\frac{r^2}{R^2}}} \int dq^r dq^\phi dq^{\eta_s} \frac{T^2 q^\phi q^\phi e^{-\sqrt{q^r q^r + q^\phi q^\phi + q^{\eta_s} q^{\eta_s}}}}{Tr^2\left(1+\frac{r^2}{R^2}\right)\sqrt{q^r q^r + \frac{q^\phi q^\phi}{1+\frac{r^2}{R^2}}}} \\
&\overset{(2.7.4)-(2.7.6)}{=} \frac{CT^4}{2\tau r^3\left(1+\frac{r^2}{R^2}\right)^{\frac{3}{2}}} \int_0^\infty d|q^r| \int_0^\pi d\theta_q \int_0^{2\pi} d\phi_q \frac{|q^r|^4 \sin(\theta_q)\cos^2(\theta_q) e^{-|q^r|}}{|q^r|\sqrt{\sin^2(\theta_q) + \frac{\cos^2(\theta_q)}{1+\frac{r^2}{R^2}}}} \\
&= \frac{6\pi CT^4}{\tau r^3\left(1+\frac{r^2}{R^2}\right)} \int_0^\pi d\theta_q \frac{\sin(\theta_q)\cos^2(\theta_q)}{\sqrt{1+\frac{r^2}{R^2}\sin^2(\theta_q)}} \\
&= \frac{6\pi CT^4}{\tau r^3\left(1+\frac{r^2}{R^2}\right)} \frac{R^3}{r^3}\left[-\frac{r}{R} + \left(1+\frac{r^2}{R^2}\right)\arctan\left(\frac{r}{R}\right)\right] \qquad (2.7.14) \\
&= \frac{2\alpha}{r^2\left(1+\frac{r^2}{R^2}\right)} \frac{R^3}{r^3}\left[-\frac{r}{R} + \left(1+\frac{r^2}{R^2}\right)\arctan\left(\frac{r}{R}\right)\right]
\end{aligned}
$$

To deal with a physical anisotropic pressure, we have to take care of the metrics contribution r^2. Multiplying formula (2.7.14) with this factor enables us to plot the $\mathcal{P}^\phi$-component's dependence on r/R of the energy momentum tensor.

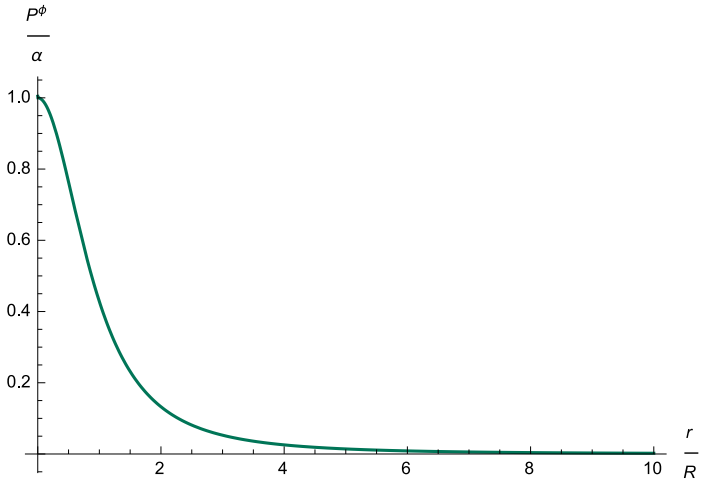

Figure 2.14.: Plot of $^{\mathcal{P}^\phi}/_{\alpha}$ over $^{r}/_{R}$

2.7.9. 2^{nd}-moment of the free streaming distribution $F_{fs}(x^\mu, p^i)$ wrt. p^{η_s}

Here we present the last diagonal component of the energy momentum tensor, which is the $\eta_s\eta_s$ component.

$$
\begin{aligned}
\frac{\mathcal{P}^{\eta_s}}{\tau^2} &= T^{\eta_s\eta_s} = \int \frac{d^3p}{2\tau r p^\tau} p^{\eta_s} p^{\eta_s} F_{fs}(x^\mu, p^i) \\
&= \frac{C}{2}\int dp^r dp^\phi dp^{\eta_s} \frac{p^{\eta_s} p^{\eta_s} e^{-\sqrt{\frac{p^r p^r}{T^2} + \frac{r^2\left(1+\frac{r^2}{R^2}\right)p^\phi p^\phi}{T^2} + \frac{\tau^2 p^{\eta_s} p^{\eta_s}}{T^2}}}}{\sqrt{p^r p^r + r^2 p^\phi p^\phi + \tau^2 p^{\eta_s} p^{\eta_s}}} \\
&\overset{(2.7.1)-(2.7.3)}{=} \frac{CT^3}{2\tau^3 r\sqrt{1+\frac{r^2}{R^2}}}\int dq^r dq^\phi dq^{\eta_s} \frac{T^2 q^{\eta_s} q^{\eta_s} e^{-\sqrt{q^r q^r + q^\phi q^\phi + q^{\eta_s} q^{\eta_s}}}}{T\sqrt{q^r q^r + \frac{q^\phi q^\phi}{1+\frac{r^2}{R^2}}}} \\
&\overset{(2.7.4)-(2.7.6)}{=} \frac{CT^4}{2\tau^3 r\sqrt{1+\frac{r^2}{R^2}}}\int_0^\infty d|q^r| \int_0^\pi d\theta_q \int_0^{2\pi} d\phi_q \frac{|q^r|^4 \sin^3(\theta_q)\sin^2(\phi_q) e^{-|q^r|}}{|q^r|\sqrt{\sin^2(\theta_q) + \frac{\cos^2(\theta_q)}{1+\frac{r^2}{R^2}}}} \\
&= \frac{3\pi CT^4}{\tau^3 r}\int_0^\pi d\theta_q \frac{\sin^3(\theta_q)}{\sqrt{1+\frac{r^2}{R^2}\sin^2(\theta_q)}} \\
&= \frac{3\pi CT^4}{\tau^3 r}\frac{R^2}{r^2}\left[1 + \frac{R}{r}\left(\frac{r^2}{R^2} - 1\right)\arctan\left(\frac{r}{R}\right)\right] \qquad (2.7.15) \\
&= \frac{\alpha}{\tau^2}\frac{R^2}{r^2}\left[1 + \frac{R}{r}\left(\frac{r^2}{R^2} - 1\right)\arctan\left(\frac{r}{R}\right)\right]
\end{aligned}
$$

Again we have to take care of the metrics contribution in order to deal with a physical anisotropic pressure component. The factor is in this case τ^2.

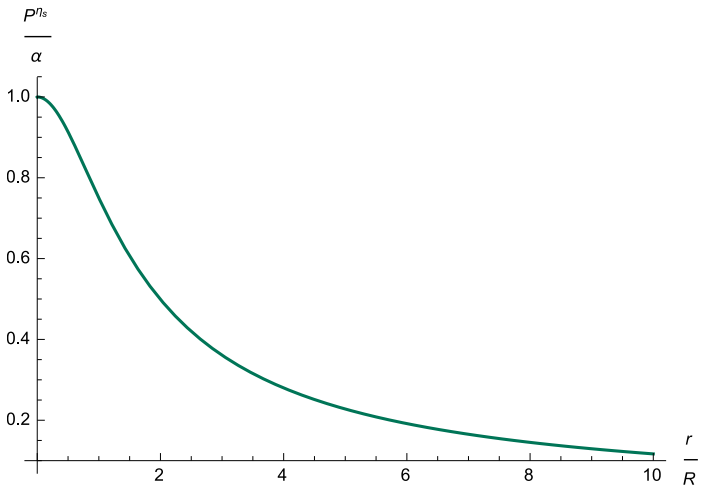

Figure 2.15.: Plot of the ratio $\mathcal{P}^{\eta_s}/\alpha$ over r/R

2.7.10. Comments

As a first remark let us mention that all off-diagonal elements of the energy momentum tensor T^{ij} are vanishing, since they consist of an integral of an odd function in p^μ or p^ν, a symmetric integration interval – with respect to zero – and the in momentum components even function F_{fs}[23]. As expected we have no " new-dissipative" contributions to the hydrodynamic fields, since particle fluxes $N^i = 0$ or energy fluxes $T^{\mu\nu} = 0$ – where $\nu \neq \mu$ – are vanishing. In this sense we are still dealing with a look alike ideal hydrodynamical framework. But since the pressure components are not all the same, we capture at least the most important dissipative effect arising from the anisotropy.

The second remark is about the trace of the computed energy-momentum tensor. To check this let us introduce the following abbreviations[24].

$$\frac{6\pi C T^4}{\tau r} = 2\alpha$$

and

$$\frac{r}{R} = x$$

With this we can compute the trace of the energy momentum tensor clearly represented.

[23] This is the same argument as for the space-components of the current N^i.

[24] The attentive reader recognizes, that we used the definition of α already in the last steps of the second moment computations.

$$
\begin{aligned}
T^{\mu}{}_{\mu} &= \epsilon - \left(T^{rr} + r^2 T^{\phi\phi} + \tau^2 T^{\eta_s \eta_s}\right) \\
&\overset{(2.7.12)-(2.7.15)}{=} 2\alpha \left[\frac{1}{1+x^2} + \frac{\arctan(x)}{x} - \frac{1}{2x^2}\left(1 + \frac{1}{x}\left(x^2-1\right)\arctan(x)\right)\right. \\
&\quad \left. - \frac{1}{1+x^2}\frac{1}{x^3}\left(-x + (1+x^2)\right)\arctan(x)\right] \\
&\quad - \frac{\alpha}{2x^2}\left[1 + \frac{1}{x}(x^2-1)\arctan(x)\right] \\
&= 2\alpha \left[\frac{1}{1+x^2} + \frac{\arctan(x)}{x} - \frac{1}{2x^2} - \frac{\arctan(x)}{2x} + \frac{\arctan(x)}{2x^3}\right. \\
&\quad \left. + \frac{1}{x^2(1+x^2)} - \frac{\arctan(x)}{x^3} - \frac{1}{2x^2} - \frac{\arctan(x)}{2x} + \frac{\arctan(x)}{2x^3}\right] \\
&= 2\alpha \left[\frac{1}{1+x^2} - \frac{1}{x^2} + \frac{1}{x^2(1+x^2)}\right] \\
&= 0 \qquad (2.7.16)
\end{aligned}
$$

This trace is vanishing for all positions and temperatures of the system. Although the simple equation of state in the isotropic case, which reads for massless non interacting particles like $\epsilon = 3\mathcal{P}$ is not valid anymore, since the pressure components differ in the anisotropic case, we can still make the statement $\epsilon = \sum_i \mathcal{P}^i$. Due to the fact that regarding formula (2.7.16) the energy momentum tensor arising from F_{fs} has a vanishing trace.

This characteristic can be found in the ideal hydrodynamical case as well.

2.7.11. Evolution of the pressure components

In this section we present a graph of the two relevant pressure's ratio $\mathcal{P}^{\phi}/\mathcal{P}^{r}$ to check how the anisotropy in the system is evolving in the steady state setup[25].

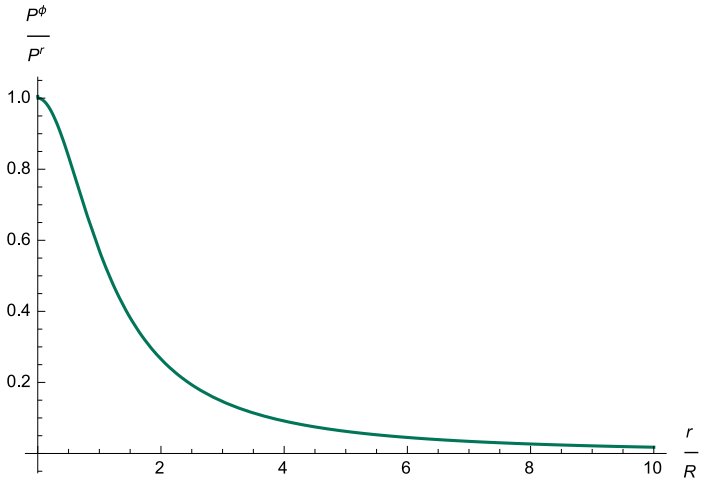

Figure 2.16.: Plot of the ratio $\mathcal{P}^{\phi}/\mathcal{P}^{r}$ over r/R.

[25] We already saw a conceptually similar ratio of pressures as a measure of anisotropy in Figure 2.1.

As one can see in figure 2.16, the system is at $r = 0$ isotropic and all relevant pressure components are the same since we start our system from a Jüttner distribution. With increasing "distance" r/R the ratio $\mathcal{P}^\phi/\mathcal{P}^r$ decreases. Therefore the polar pressure component decreases faster than radial counterpart. After approximately a value of $r/R = 4$ the pressure ratio decayed already to a value of approximately 0.1. In other words at this point the orthoradial pressure component $\mathcal{P}^\phi$ is already one order of magnitude less than the radial pressure component $\mathcal{P}^r$. This effect is due to the computed anisotropy parameter (2.5.3).

A second remark is about the scale R at which the anisotropy develops. While setting this scale to a higher value, the anisotropy's effect can be delayed. Figure 2.17 shows this behavior for three different values of the anisotropy scale R.

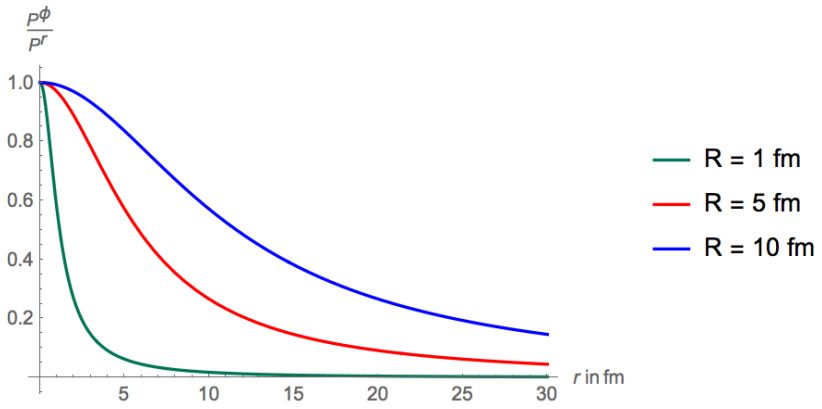

Figure 2.17.: Plot of the ratio $\mathcal{P}^\phi/\mathcal{P}^r$ over r for different values of R .

Let us emphasize that the hydrodynamical fields computed from the derived massless free streaming solution interpolate in a smooth way between the isotropic equilibrium state and the free streaming scenario. Therefore one can make the statement that our aim to smoothen this transition is fulfilled in the case of massless degrees of freedom.

2.8. Computing the moments of the anisotropic equilibrium distribution for massive particles

In this section we are going to present the relevant moments of the free streaming solution F_{fs} for massive particles. Due to the mass in the distribution's exponent the corresponding integrals yield more complicated expressions compared to the ones in the previous section.

2.8.1. Useful substitution and useful functions

In order to compute the moments of the massive free streaming distribution – as far as possible analytically – it is very helpful to deal with a further substitution, namely

$$|q^r| \equiv \sqrt{\frac{m^2}{T^2}}\ \sinh(u) \Leftrightarrow d|q^r| = \frac{m}{T}\cosh(u)\ du \tag{2.8.1}$$

Furthermore we will employ the definition of the modified Bessel functions of second kind.

$$K_\alpha(x) \equiv \int_0^\infty dt\ \cosh(\alpha t)\ e^{-x\cosh(t)} \tag{2.8.2}$$

In addition there exist some useful recurrence identities for "consecutive neighbors" for modified Bessel functions. These relate the n-th modified Bessel function of second kind to the $(n+1)^{th}$ and the $(n-1)^{th}$ in the following way.

$$K_{n+1}(x) = K_{n-1}(x) + \frac{2n}{x}K_n(x) \tag{2.8.3}$$

These identities can be found for example in [23][26].

2.8.2. 1^{st}-moment of the free streaming distribution $F_{fs}(x^\mu, p^i)$ wrt. p^τ

Since the 0^{st}-moment of the distribution function has no hydrodynamical meaning we start with the computation of the 1^{st}-moment with respect to p^τ for massive particles. Note that this coincides to the particle density in the limit of $u^r \ll u^\tau$, which corresponds to a small perpendicular expansion. Like in the case before the first computation of this kind will be presented in detail, all the others, which employ the same steps are presented without comments.

$$N^\tau = \int \frac{d^3p}{2\tau r p^\tau} p^\tau F_{fs}(x^\mu, p^i)$$

Inserting the massive version of the free streaming distribution function leads to the following equation.

$$N^\tau = \frac{C}{2}\int dp^r dp^\phi dp^{\eta_s} e^{-\sqrt{\frac{m^2}{T^2}+\frac{p^r p^r}{T^2}+\left(1+\frac{r^2}{R^2}\right)\frac{r^2 p^\phi p^\phi}{T^2}+\frac{\tau^2 p^{\eta_s} p^{\eta_s}}{T^2}}}$$

At this point we can employ the substitutions (2.7.1) - (2.7.3) for the momentum components.

$$N^\tau = \frac{CT^3}{2\tau r\sqrt{1+\frac{r^2}{R^2}}}\int dq^r dq^\phi dq^{\eta_s} e^{-\sqrt{\frac{m^2}{T^2}+q^r q^r+q^\phi q^\phi+q^{\eta_s} q^{\eta_s}}}$$

Now we can simplify the exponent while switching to spherical coordinates.

$$N^\tau \overset{(2.7.4)-(2.7.6)}{=} \frac{2\pi CT^3}{\tau r\sqrt{1+\frac{r^2}{R^2}}}\int_0^\infty d|q^r||q^r|^2 e^{-\sqrt{\frac{m^2}{T^2}+|q^r|^2}}$$

At this point we need to perform the above presented substitution (2.8.1), in order to simplify the exponent further.

[26] Chapter 2.4.2 page 111

$$N^\tau \overset{(2.8.1)}{=} \frac{2\pi C m^3}{\tau r\sqrt{1+\frac{r^2}{R^2}}} \int_0^\infty du \cosh(u)\sinh^2(u) e^{-\sqrt{\frac{m^2}{T^2}\left(1+\sinh^2(u)\right)}} \tag{2.8.4}$$

For the hyperbolic functions sinh and cosh, there exist useful relations. We will employ $\left(1+\sinh^2(u)\right) = \cosh^2(u)$ for the exponent and $\cosh(u)\sinh^2(u) = 1/2\cosh(u)(\cosh(2u) - 1) = 1/4\left(\cosh(3u) - \cosh(u)\right)$ for the product of hyperbolic functions in equation (2.8.4). Inserting these expressions results in the following sum of integrals.

$$N^\tau = \frac{\pi C m^3}{2\tau r\sqrt{1+\frac{r^2}{R^2}}} \left[\int_0^\infty du \cosh(3u) e^{-\frac{m}{T}\cosh(u)} - \int_0^\infty du \cosh(u) e^{-\frac{m}{T}\cosh(u)}\right]$$

Here we can make use of the definitions of the modified Bessel function (2.8.2).

$$N^\tau \overset{(2.8.2)}{=} \frac{\pi C m^3}{2\tau r\sqrt{1+\frac{r^2}{R^2}}} \left[K_3\left(\frac{m}{T}\right) - K_1\left(\frac{m}{T}\right)\right]$$

As a last step we can simplify the gained expression further by making use of the "consecutive neighbors" identities (2.8.3).

$$N^\tau \overset{(2.8.3)}{=} \frac{2\pi T C m^2}{\tau r\sqrt{1+\frac{r^2}{R^2}}} K_2\left(\frac{m}{T}\right) \tag{2.8.5}$$

Expression (2.8.5) is the final result for the 1^{st}-moment with respect to p^τ of the massive free streaming solution. Please note that the dependence of the particle density n on the position space is the same as in the massless case. To illustrate the dependence of n on the (dimensionless) ratio m/T we show figure 2.18. As one can see the density has a finite value in the limit of $m \to 0$ and is vanishing for $m/T \to \infty$, since for small arguments z, $K_2(z) \overset{\lim_{z\to 0}}{\longrightarrow} 2/z^2$. Note that this limit also guarantees the T^3 dependence of N^τ, which we found in the massless case as well.

The expression (2.8.5) for the massive particle density is comparable to expression (25) in [46], although they dealt with the above mentioned concept of a longitudinal anisotropy in momentum space.

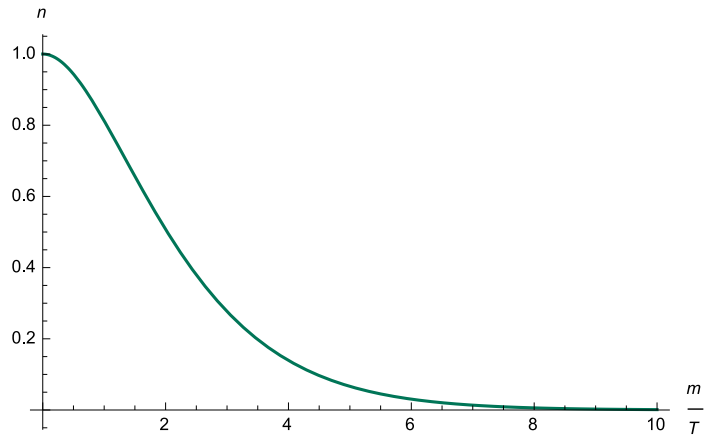

Figure 2.18.: Plot of the density n over the mass to temperature ratio m/T.

To be consistent with the plots shown before, we also plotted the particle density over the anisotropy parameter. We set the particle's mass $m = 140$ MeV, which is comparable to the pion mass. Please note that we choose this mass for all the following plots as well.

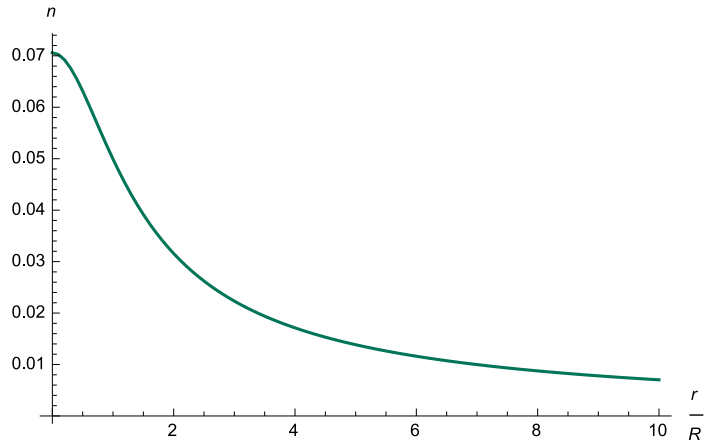

Figure 2.19.: Plot of the density n over r/R for $m = 140$ MeV and $T = 150$ MeV

2.8.3. 1^{st}-moment of the free streaming distribution $F_{fs}(x^\mu, p^i)$ wrt. p^i

For the same parity reasons as in the case of the massless first moments N^i shown in section 2.7.5 and massless second moments $T^{\mu\nu}$ with $\mu \neq \nu$ shown in section 2.7.10 the integrals weighted by a factor of p^i are vanishing.

In the case of massive particles there is still no particle flux or dissipation at work in the first moment of the distribution function.

2.8.4. 2^{nd}-moment of the free streaming distribution $F_{fs}(x^\mu, p^i)$ wrt. p^τ

At this point we can start to compute the second moment of $F_{fs}(x^\mu, p^i)$ with respect to p^τ, which gives the energy density field.

$$
\begin{aligned}
\epsilon \quad &= \quad T^{\tau\tau} = \int \frac{d^3p}{2\tau r p^\tau} p^\tau p^\tau F_{fs}(x^\mu, p^i) \\
&= \quad \frac{C}{2} \int dp^r dp^\phi dp^{\eta_s} \sqrt{m^2 + p^r p^r + r^2 p^\phi p^\phi + \tau^2 p^{\eta_s} p^{\eta_s}} \\
&\quad\; e^{-\sqrt{\frac{m^2}{T^2} + \frac{p^r p^r}{T^2} + \frac{r^2\left(1+\frac{r^2}{R^2}\right) p^\phi p^\phi}{T^2} + \frac{\tau^2 p^{\eta_s} p^{\eta_s}}{T^2}}} \\
\overset{(2.7.1)-(2.7.3)}{=} \quad &\frac{CT^4}{2\tau r \sqrt{1+\frac{r^2}{R^2}}} \int dq^r dq^\phi dq^{\eta_s} \sqrt{\frac{m^2}{T^2} + q^r q^r + \frac{q^\phi q^\phi}{1+\frac{r^2}{R^2}} + q^{\eta_s} q^{\eta_s}} \\
&\quad\; e^{-\sqrt{\frac{m^2}{T^2} + q^r q^r + q^\phi q^\phi + q^{\eta_s} q^{\eta_s}}} \\
\overset{(2.7.4)-(2.7.6)}{=} \quad &\frac{CT^4}{2\tau r \sqrt{1+\frac{r^2}{R^2}}} \int_0^\infty d|q^r| \int_0^{2\pi} d\phi_q \int_0^\pi d\theta_q |q^r|^2 \sin(\theta_q) \\
&\quad\; \sqrt{\frac{m^2}{T^2} + |q^r|^2 \left(\sin^2(\theta_q) + \frac{\cos^2(\theta_q)}{1+\frac{r^2}{R^2}} \right)} e^{-\sqrt{\frac{m^2}{T^2} + |q^r|^2}} \\
\overset{(2.8.1)}{=} \quad &\frac{\pi m^4 C}{\tau r \sqrt{1+\frac{r^2}{R^2}}} \int_0^\infty du \int_0^\pi d\theta_q \sin(\theta_q) \sqrt{1 + \sinh^2(u) \left(\sin^2(\theta_q) + \frac{\cos^2(\theta_q)}{1+\frac{r^2}{R^2}} \right)} \\
&\quad\; \underbrace{\cosh(u) \quad \underbrace{\sinh^2(u)}_{=\frac{1}{2}(\cosh(2u)-1)}}_{=\frac{1}{4}(\cosh(3u)-\cosh(u))} \quad e^{-\frac{m}{T}\cosh(u)} \\
= \quad &\frac{\pi m^4 C}{4\tau r \sqrt{1+\frac{r^2}{R^2}}} \int_0^\infty du \int_0^\pi d\theta_q \sin(\theta_q) \sqrt{1 + \frac{r^2}{R^2} \sinh^2(u) \sin^2(\theta_q)} \\
&\quad\; [\cosh(3u) - \cosh(u)]\, e^{-\frac{m}{T}\cosh(u)} \qquad (2.8.6)
\end{aligned}
$$

Unfortunately, one can not compute all integrals in formula (2.8.6) analytically. Of course the integral over the angle θ_q is possible to compute. This problem is the same for the pressure components T^{rr}, $T^{\phi\phi}$ and $T^{\eta_s\eta_s}$. In order to get shorter expressions, in [46] they defined functions $\mathcal{H}$ and $\tilde{\mathcal{H}}$ in their Appendix, which basically contain the two leftover integrals over an angle and a radial component. Nevertheless it is still possible to compute the integrals for the energy density and the pressure components for massive particles numerically in order to get an insight in their functional behavior.

2.8.5. Numerical computation of the 2^{nd}-moments of the free streaming distribution $F_{fs}(x^\mu, p^i)$

Therefore we present in this subsection the numerical computed components of the energy momentum tensor for particles which have a pion mass of 140 MeV and a temperature of 150 MeV. As one can see in figure 2.20, both the energy density and the pressure components are decreasing due to increasing anisotropy. Note that the components $\mathcal{P}^r$ and $\mathcal{P}^{\eta_s}$ are lying on top of each other. In addition, this plot shows that after 10 times of the characteristic scale R the energy density and the pressure components already dropped over one order of

magnitude.

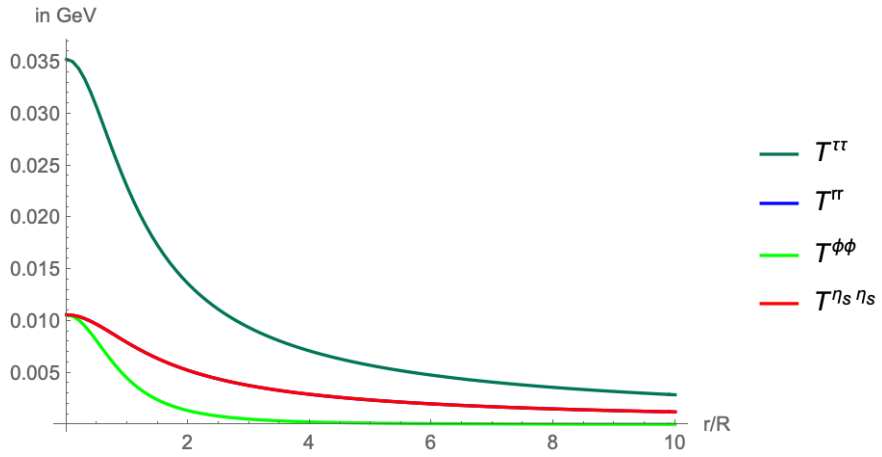

Figure 2.20.: Plot of the diagonal components of the massive energy momentum tensor over r/R for $m = 140$ MeV and $T = 150$ MeV.

Figure 2.21 shows the so called trace anomaly $T^{\tau\tau} - T^{rr} - T^{\phi\phi} - T^{\eta_s\eta_s}$ of the numerical computed energy momentum tensor. As a short reminder for the massless case we found the trace to be vanishing. In the numerical computed, massive case we get a contribution for the trace. But this contribution is small and decays with increasing anisotropy.

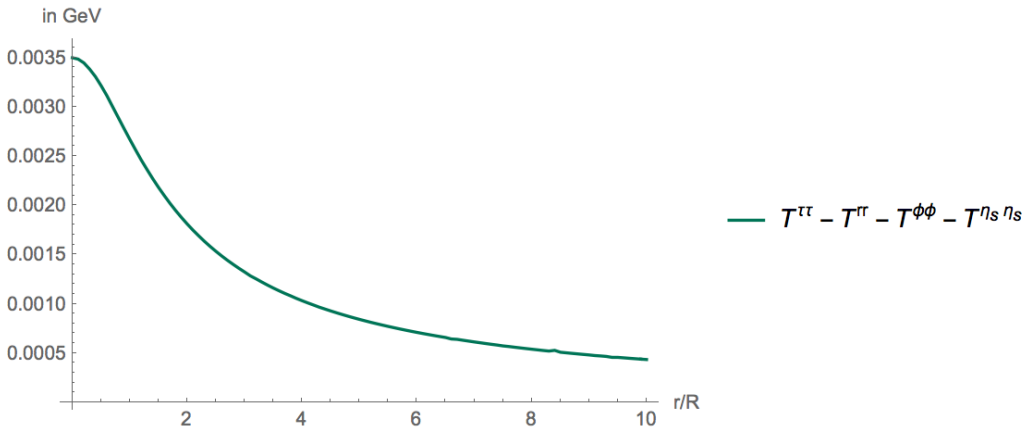

Figure 2.21.: Plot of the massive energy momentum tensor 's trace over r/R for $m = 140$ MeV and $T = 150$ MeV.

2.8.6. Remarks

Within the two last sections 2.7 and 2.8 we computed the hydrodynamical fields, which emerge from the free streaming distribution function F_{fs} for massless particles as well as in the case of massive particles. In addition we showed various plots of the arising fields. As a conclusion we should mention that all fields follow a continuous evolution with respect to r/R. Furthermore, all fields are negligible at least after 10 times of the scale R.

2.9. Physical observables for the distribution $F_{fs}(x^\mu, p^i)$

Since we computed up to now the hydrodynamical fields, we will now turn to compute "real" heavy-ion observables, in the sense of observables which are measured in the experiment. The most intuitive observable is the particle spectrum. It is the (Lorentz invariant) number of detected particles per momentum bin. One can compute this particle spectrum via the already mentioned Cooper-Frye formula, since in this formalism the fliud emits right at the hypersurface particles which are not interacting anymore. Therefore their momenta are frozen from that hypersurface on. Please note that this is not valid anymore if one incorporates interactions after the hypersurface throughout an afterburner [47].

2.9.1. Particle spectrum from an isotropic fluid

In order to compute the particle spectrum we follow the well known idea of [16] established in 1974. The publication basically deals with the question how to convert a fluiddynamical field into a particle spectrum, while conserving energy and momentum. The starting point is the single-particle phase space density f. In order to present the basic ingredients of the Cooper-Frye formula in a compact way, we will follow the argumentation of [1][27]. If the distribution function is normalized in the right way, its integral over phase space gives the total number of particles N in the system. Therefrom we can deduce the following.

$$\begin{aligned} N &= \int \frac{d^3\vec{x}\; d^3\vec{p}}{(2\pi)^3}\; f \\ \Leftrightarrow dN &= dV \int \frac{d^3\vec{p}}{(2\pi)^3}\; f \end{aligned}$$

The desired observable is the Lorentz invariant particle number per momentum bin, which looks as follows.

$$E_p \frac{d^3N}{d^3\vec{p}} \tag{2.9.1}$$

Note that the factor p^τ or E_p guarantees the particle spectrum to be a Lorentz invariant number and therefore a proper observable. In order to gain such an expression (2.9.1) we have to integrate out the position space dependence of the distribution function.

This is not that trivial. Since we want to describe the transformation of a whole fluid flowing through a surface Σ, we have to change the reference frame from a local one to a global one, where the surface Σ is at rest. At some point we have to specify the hypersurface by a model. With all these ingredients one can gather the Cooper-Frye formula which is written in the next expression.

$$E_p\; \frac{d^3N}{d^3p} = \frac{1}{(2\pi)^3} \int_\Sigma p^\mu d\Sigma_\mu(x)\; f([p^\alpha u_\alpha(x)]) \tag{2.9.2}$$

In formula (2.9.2) Σ_μ denotes the normal surface vector of the hypersurface Σ over which one has to integrate. The factor $p^\mu \cdot d\Sigma_\mu(x)$ guarantees that the fluid element is comoving.

[27] Chapter 15.3

The hydrodynamicla evolution prior to the kinetic freeze out enters this formula via the flow velocity field $u_\alpha(x)$. Since we are not running a numerical hydro code, we are implementing for the velocity field a blast wave ansatz [48, 49]. This ansatz just reads:

$$u^\tau = \sqrt{1+(u^r)^2} \tag{2.9.3}$$

$$u^r = u_{max}\frac{r}{R_{BW}}\left(1+2\sum_{n=2}V_n\ cos(n\phi)\right)\Theta(R_{BW}-r) \tag{2.9.4}$$

$$u^\phi = u^{\eta_s} = 0 \tag{2.9.5}$$

This flow profile mimics a radial hydrodynamical expansion, whose acceleration is stopped at the blast wave radius R_{BW}. Consistently we choose the hypersurface's radial extent to have a radius of R_{BW} in the transverse plane. The factors V_n are implementing a possible polar $2\pi/n$ structure, which will be important for the next sections. Throughout non vanishing V_n of course the Radius R_{BW} is slightly varying with the azimuthal angle ϕ.

Note that while running a real hydro code one has to model the freeze out surface Σ with an underlying physical model. As mentioned already in the motivation 2.1, here one can choose the hypersurface to be the collection of points where either temperature, particle density, energy density or mean free path reaches some critical value.

Another problem arises from surface regions, where the factor $p^\mu \cdot d\Sigma_\mu(x)$ gives negative contributions. It was taken care of this problem in [50] at the expence of discontinuities in the evolution and in [51] within a transport approach and interpreting negative contributions as fluid reentering particles.

Within our computations we perform a freeze out at a specific proper time τ_0 on a cylinder of radius R_{BW} as done e.g. by Teaney [52]. Written in a formula it reads as the following.

$$p^\mu \cdot d\Sigma_\mu = m_t\ \cosh(y-\eta_s)\ \tau_0\ d\eta_s\ r dr\ d\phi$$

In order to compute the spectrum for an ideal fluid of classical particles within the blast wave ansatz one has to compute the following steps.

$$\begin{aligned}
p_t\frac{d^2N}{d^2p_t} &= \frac{C}{(2\pi)^3}\int_\Sigma p^\mu d\Sigma_\mu\ e^{-\frac{p^\mu u_\mu}{T}} \\
&= \frac{C}{(2\pi)^3}\int_0^{2\pi}d\phi\int_0^{R_{BW}}dr\ r\int_{-\infty}^{\infty}d\eta_s\ \tau_0\ m_t\ \cosh(\eta_s)\ e^{-\frac{m_t\cosh(\eta_s)}{T}} \\
&= \frac{C\ m_t\ \tau_0}{(2\pi)^2}\frac{R_{BW}^2}{2}\int_{-\infty}^{\infty}d\eta_s\ \cosh(\eta_s)\ e^{-\frac{m_t}{T}\ \cosh(\eta_s)} \\
&\overset{(2.8.2)}{=} \frac{C\ m_t\ \tau_0\ R_{BW}^2}{(2\pi)^2}\ K_1\left(\frac{m_t}{T}\right)
\end{aligned} \tag{2.9.6}$$

This result can be found to agree with the expression in the Appendix of [52] as well.

Figure 2.22 shows a plot of three pion spectra computed from a local Jüttner distribution (2.4.13), within the above mentioned assumptions for different freeze out temperatures T. As one can see the spectra differ very much in the low p_t regime. In numbers the difference is over two hundred particles in the lowest momentum bin, although the temperature difference is about 25 MeV.

This figure is a first example that physical observables have a strong dependence on quantities chosen at the freeze out surface. So this plot is reflecting our main motivation for the anisotropic freeze out formalism.

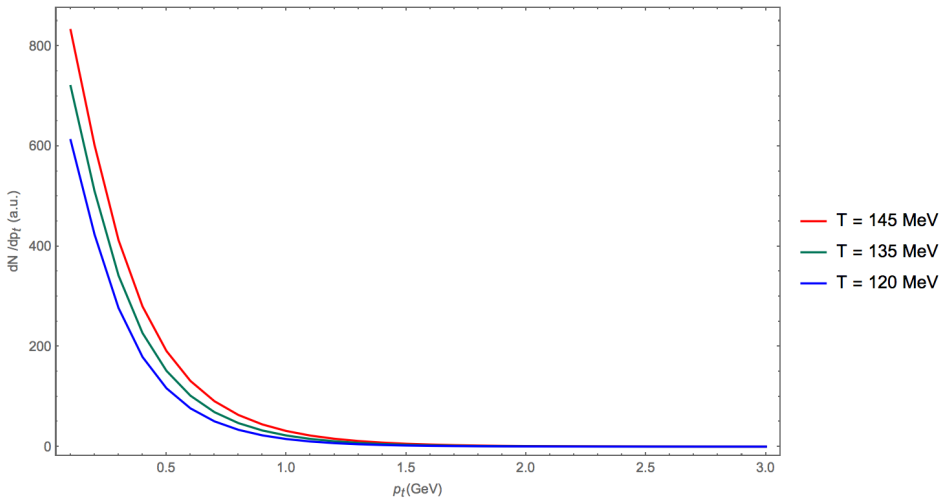

Figure 2.22.: Plot of the particle spectra at different temperatures. For the mass m we used the pion mass.

Figure 2.23 shows the same spectra on a logarithmic scale. As one can see the pion spectra are nearly linear on a logarithmic scale.

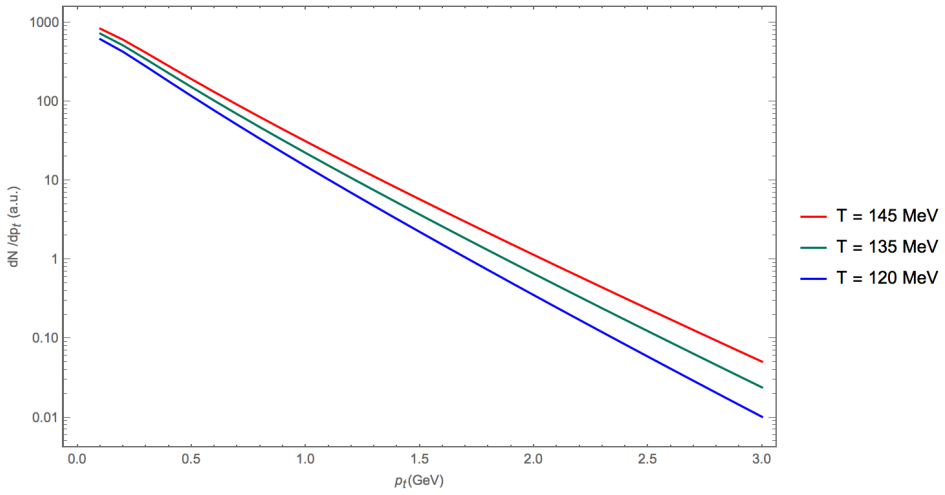

Figure 2.23.: Logarithmic plot of the particle spectra at different temperatures. For the mass m we used the pion mass.

Figure 2.24 shows particle spectra for the same temperature T, but for different particle masses. The masses are the corresponding pion, kaon and proton masses, which build up the majority of detected particles in heavy-ion collisions. As one can see in general, heavier particles are emitted in a smaller number. This has to be the case, since the Cooper-Frye formula is constructed to conserve energy. As a second observation one can recognize that

the higher particle masses result in a more pronounced curvature starting right below the particle mass.

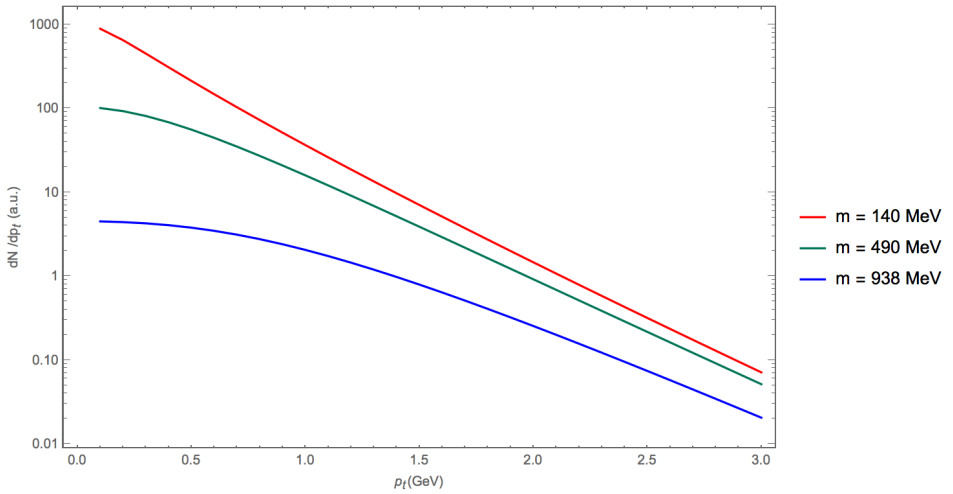

Figure 2.24.: Logarithmic plot of the particle spectra for different particle masses. For the temperature T we choose 130 MeV.

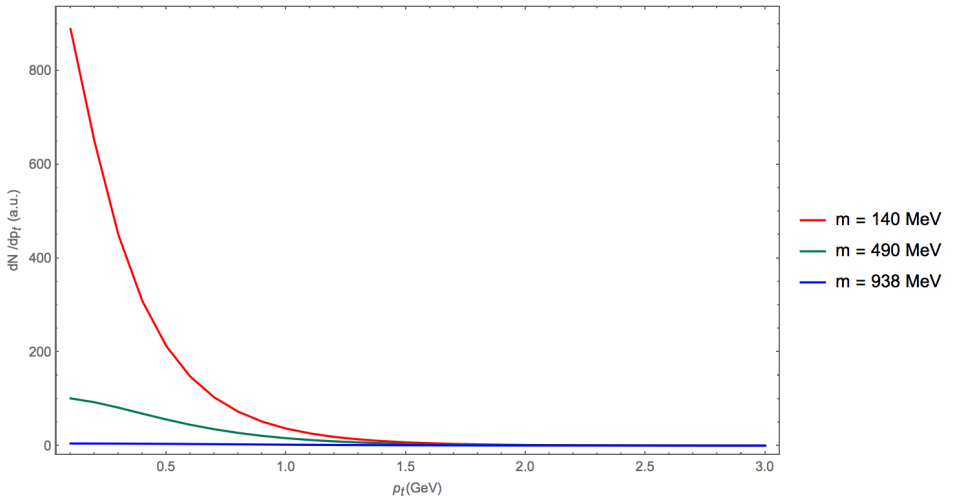

Figure 2.25.: Linear plot of the particle spectra for different particle masses. For the temperature T we chose 130 MeV.

Now that we introduced the basic features of the particle momentum spectra let us take a look at experimental data of the spectrum in recent measurements presented in the ALICE publication [53].

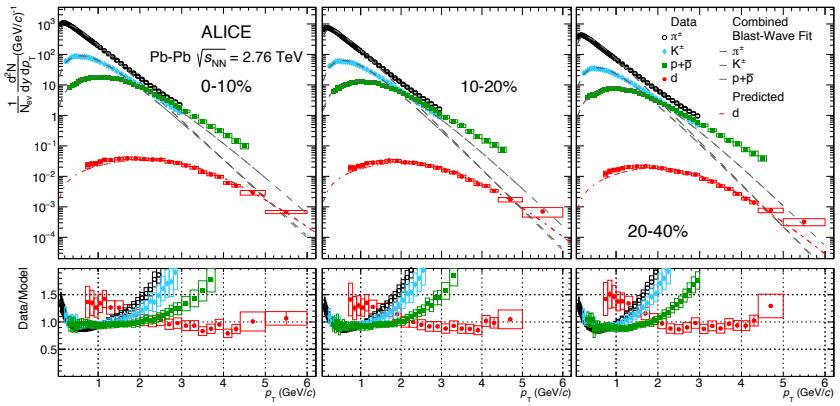

Figure 2.26.: Logarithmic plot of the particle spectra over transverse momentum p_t for two different energies in Pb-Pb collisions. Taken from ALICE measurements [53].

The upper plots show the particle spectra plotted over transversal momentum p_t. Therefore let us concentrate on the upper part of the figure. There the spectra for pions, kaons, protons and deuterion are plotted over the transverse momentum p_t. From the left panel to the right panel the collisions are more noncentral. One can see the effect of the bending of the curves due to increasing masses, since the deuterium mass is more than ten times higher than the pion mass.

A comparison to figure (2.24) shows that already this simple model reproduces the shape of the spectra quite well.

2.9.2. Particle spectrum from $F_{fs}(x^\mu, p^i)$

Since we want to investigate the freeze out from the elaborated local anisotropic distribution function F_{fs} the computations become more difficult, because the anisotropy builds up with radius. Therefore the integrals over the position space become harder to solve. Nevertheless we computed them numerically. To show that the freeze out procedure is smoothed by the anisotropy we chose an isotropic freeze out process as reference state. For this we chose a kinetic freeze out temperature of 130 MeV. In order to perform the integrals over the freeze out hypersurface we have to boost the locally formulated distribution function in a global reference frame. For the blast wave coefficients we chose again for the radius $R_{BW} = 10$ fm, for the proper time $\tau_0 = 7.5$ fm and for the velocity field $u_{max} = 1$. As a last remark let me mention again that we denoted – as it is common – the "anisotropic temperatures" by the letter Λ in order to emphasize that this is not the isotopic temperature anymore. Written in a formula we have to solve the following integral:

$$\begin{aligned} p^\tau \frac{d^2N}{d^2p_t} &= \frac{C}{2\pi}\int_\Sigma p^\mu \, d\Sigma_\mu e^{-\frac{1}{\Lambda}\sqrt{(p\cdot u)^2+\frac{r^4}{R^2}\left(u^\tau p^\phi - u^\phi p^\tau\right)^2}} \\ &= \frac{C}{2\pi}\int_{-\infty}^{\infty} d\eta_s \int_0^{2\pi} d\phi \int_0^{R_{BW}} dr \; r \; \tau_0 \; m_t \; \cosh(\eta_s) \\ &\quad e^{-\frac{1}{\Lambda}\sqrt{(p^\tau u_\tau - p^r u_r)^2+\frac{r^4}{R^2}\left(u^\tau p^\phi - u^\phi p^\tau\right)^2}} \end{aligned} \tag{2.9.7}$$

Since we have no anisotropic hydro solver at work, we had to deal with a crucial point,

which I will describe here. If we perform a kinetic freeze out at some specific point in one case and perform a kinetic freeze out for another scenario later, we are not able to mimic the "in between time" hydrodynamically. This is due to the lack of a suitable code. Therefore we performed the computations in the "backwards direction", since we fitted the anisotropy parameter scale R in such a way that the particle spectra for different temperatures are matching. Of course this has to be optimized within a dynamical framework at some point. But here as a proof of principle of the formalism's advantages it works out well as we will see in the following.

Particle spectra[28] computed via formula (2.9.7) are shown in figure 2.27 for different anisotropic temperatures Λ at the freeze out surface. The fitted values for the scale R are listed on the right hand side. As one can see within the anisotropic freeze out we are able to get rid of the strong dependence of the spectra on the freeze out temperature. Please note that for temperatures that are smaller than the isotropic reference temperature we had to chose the anisotropy contribution to have a negative sign. Looking at the computed moments one realizes that phenomenological a negative sign of the anisotropy parameter leads to larger pressure components, energy densities and particle densities in the anisotropic hydrodynamics.

Figure 2.28 shows the same data as 2.27 plotted on a linear scale. If one compares these two plots with the above shown plots 2.22 and 2.23 over the whole plotted p_t region, one realizes the achieved insensitivity of the observable on the temperature at freeze out.

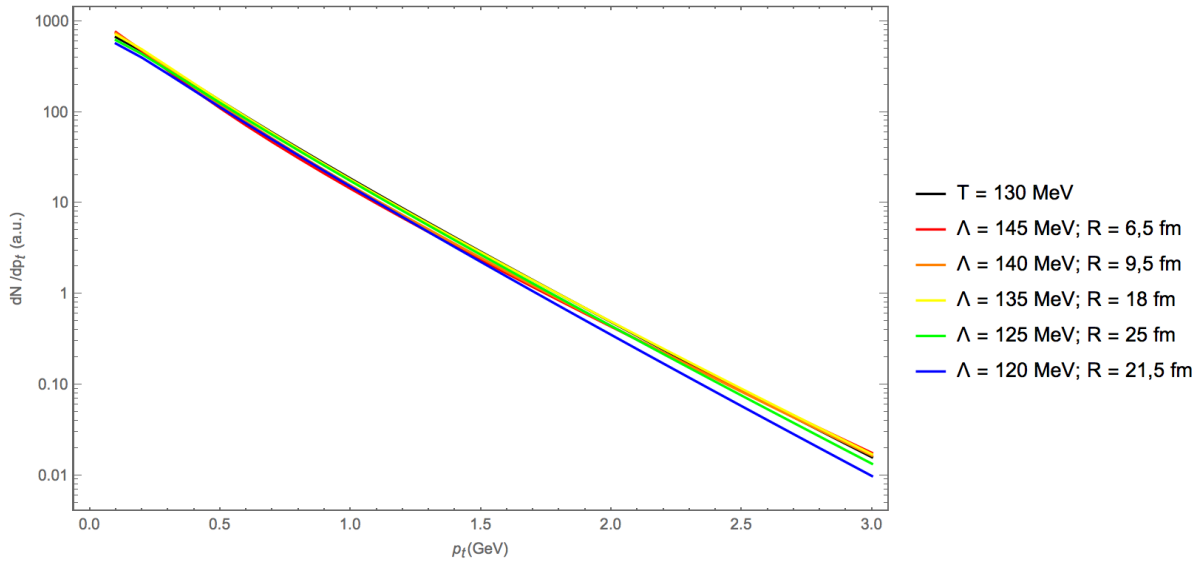

Figure 2.27.: Logarithmic plot of the particle spectra at different temperatures and anisotropy scales. For the mass m we used the pion mass of 140 MeV.

[28] Of course including after the insertion of the definitions for the relevant p^μ and u^μ components, which leads to a daunting expression.

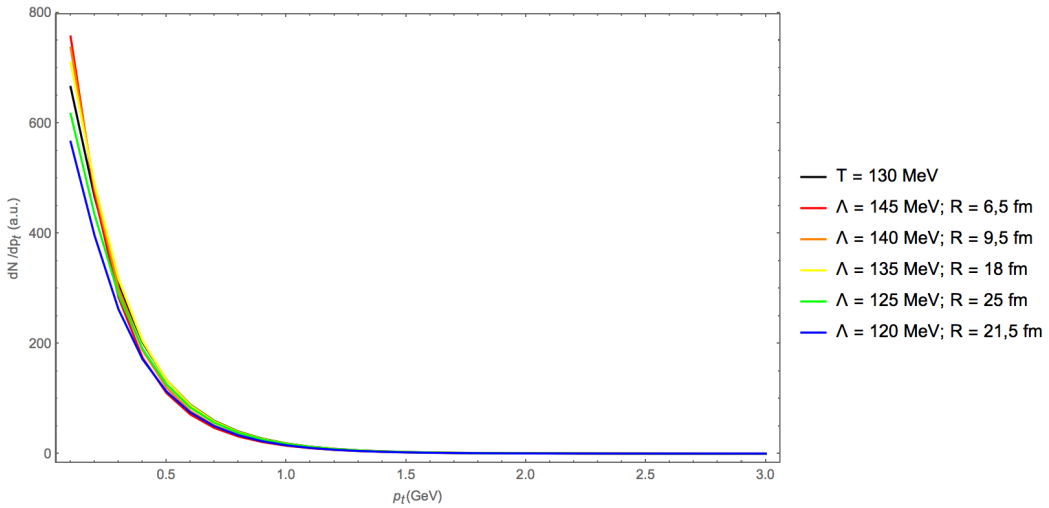

Figure 2.28.: Linear plot of the particle spectra at different temperatures and anisotropies. For the mass m we used the pion mass.

The next figure (2.29) shows a plot of the relative differences of the particle's spectra in dependence of the transverse momentum. As one can see for very low temperatures it gets harder to fit the anisotropic spectrum to an isotropic one. But leaving aside the blue curve this plot shows that the anisotropic freeze out works within 20 % over a temperature interval of 20 MeV over the whole collective momentum scale. Note that the optimization of the parameter R was done by eye. There were no algorithm at work, which means there would be space for further optimization as well.

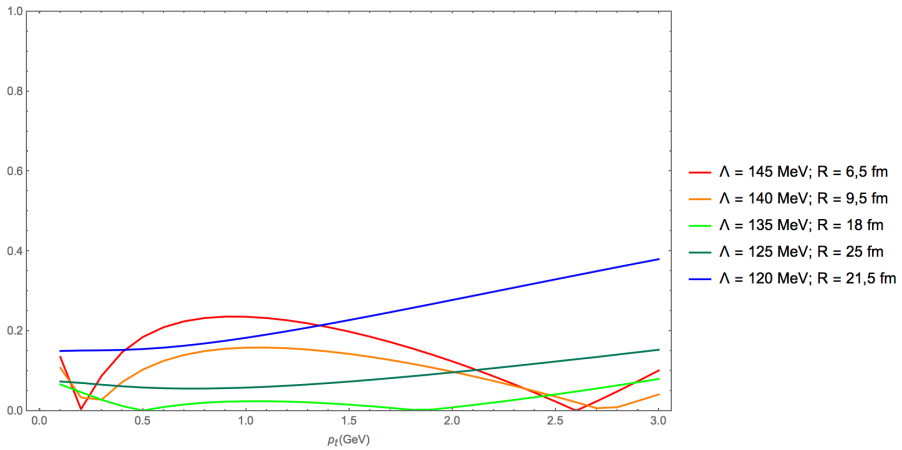

Figure 2.29.: Plot of the relative differences of the anisotropic particle spectra to the isotropic spectra. For the mass m we used the pion mass.

Before closing the section about the particle spectra we present plot 2.30 with the determined values for the anisotropy parameter R in dependence of the temperature Λ.

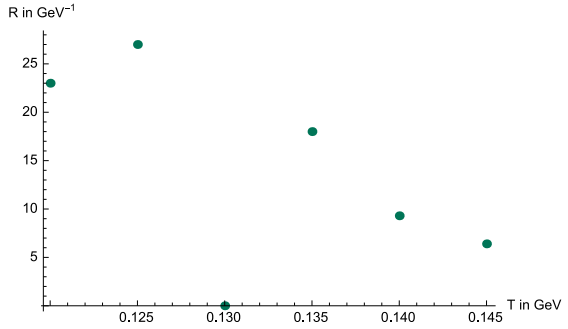

Figure 2.30.: Plot of the determined values for R over the temperature Λ.

As one can see the "backwards determined value" of R shows a rather smooth dependence of the temperature at the freeze out surface. Note that the data point at 130 MeV is ill defined, since this is the isotropic reference state, which exhibit per definition no anisotropy scale.

2.9.3. Anisotropic flow coefficients v_n

In the last section we dealt with the particle spectrum, which is basically counting particles in dependence of their momenta. But there is of course a bunch of other observables. A commonly used observable is governed by the anisotropic flow coefficients. The first investigations of anisotropies in the transverse flow – in the regime of highly Lorentz contracted nuclei collisions – can be found in [54]. The common formulation of this observable was established a bit later in [55].

The basic idea behind this observable from a mathematical point of view is a Fourier expansion in the momentum polar angle[29] ϕ_p of the particle momentum spectrum. Due to the fact that one expects an even symmetry with respect to the symmetry axis ψ_n, whose geometrical meanings are illustrated in figure 2.32, one only has to deal with cos contributions in the expansion[30]. In general this reads like the next formula[31].

$$\frac{dN}{d^2\vec{p}_t\, d\eta} = \frac{1}{2\pi}\frac{d^3N}{p_t\, dp_t\, d\eta}\left[1 + 2\sum_{n=2}^{\infty} v_n(p_t)\cos(n(\phi_p - \psi_n))\right] \tag{2.9.8}$$

Here the $v_n(p_t)$ are the anisotropic flow coefficients of n^{th}-order, which can be computed via the following expression.

$$v_n(p_t) = \frac{\int_0^{2\pi} d\phi_p \, \frac{d^3N}{d^2\vec{p}_t d\eta}\cos(n\phi_p)}{\int_0^{2\pi} d\phi_p \, \frac{d^3N}{d^2\vec{p}_t d\eta}} \tag{2.9.9}$$

Since these coefficients are a measure for the amplitude of the $2\pi/n$-periodicity of the momentum space spectra they are very often attached to geometrical objects. In figure 2.31 the resulting symmetries for the first coefficients are sketched.

[29] Which has per definition a periodicity, which is needed for applying the concept of Fourier expansions.
[30] See [56] for a detailed derivation.
[31] Note that we implicitly assumed the coordinate system to be centralized, so the sum starts at $n = 2$.

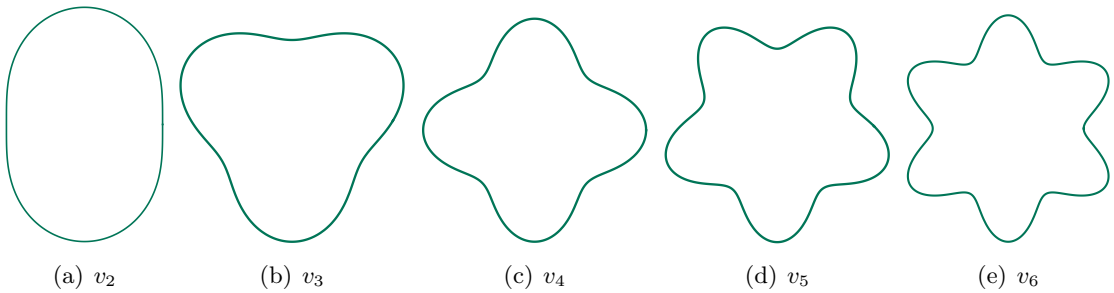

(a) v_2 (b) v_3 (c) v_4 (d) v_5 (e) v_6

Figure 2.31.: Sketch of the symmetries which are characterized by harmonic flow coefficients v_2, v_3, v_4, v_5 and v_6.

For example v_2 is referred to the elliptic flow, v_3 to the triangular flow and so forth. The angle ψ_n is called n^{th}-harmonic symmetry plane. It indicates the symmetry plane of the spectrum's $^{2\pi}/_{n}$-symmetry. As a remark let us mention that as of mid 2018 the flow coefficients are experimentally measured up to the sixth order. Especially in the collective dynamic p_t-regime, these $v_n(p_t)$ coefficients are built up due to eccentricities in the initial position space distribution. Figure 2.32 shows the standard picture of the origin of non vanishing anisotropic flow coefficients.

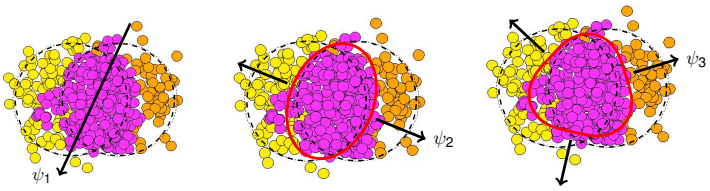

Figure 2.32.: Sketch of the initial state in position space of a heavy-ion collision. Taken from [57].

The overlap region of the two colliding nuclei varies from event to event, because a nucleus is built up by nucleons which are distributed with a certain distribution, namely the Woods-Saxon distribution for large nuclei. For such an overlap region one can compute the eccentricity ϵ_2 as well as higher eccentricities ϵ_n, with $n \geq 3$. During the expansion, which can be described for example hydrodynamically, these eccentricities in position space are transferred into the anisotropic flow coefficients in the momentum space.

Before 2010 people always averaged over many initial conditions, which leads to vanishing odd flow coefficients in collisions of identical nuclei. Consequently the initial condition looked like the overlap region in figure 2.33. Afterwards they built the averaged initial condition into hydro codes in order to compute for example the flow coefficients. However hydrodynamics is non linear, which means averaging over initial stage plus evolving hydrodynamically[32] gives other values than evolving every initial condition and average over the – so called – event-by-event hydrodynamical observables[33]. Please note, that not only hydrodynamics is able to "translate" initial stage excentricities into non vanishing flow coefficients, but also kinetic theory shows such a behavior, although the efficiency is smaller [25–27,29]. But all in

[32] ,as was done by the theorists.
[33] ,as happens in the experiment.

all interactions are needed to transform the eccentricities to non-vanishing flow coefficients, therefore the flow coefficients are often held to be observables of collectivity.

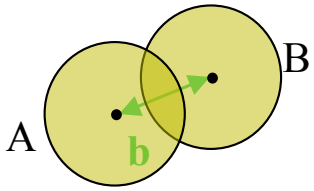

Figure 2.33.: Sketch of an idealized/averaged initial state of a heavy-ion collision. Taken from [18].

As a next remark let us mention that the values of the flow coefficients will in reality also depend on the impact parameter b of the collision, as can be seen in figure 2.33. Figure 2.34 shows experimental data of the p_t-integrated flow coefficients plotted over centrality classes to show the above mentioned dependence. Centrality classes are roughly related to the impact parameter and, compared to b, experimentally measurable. Note that the centrality class of $0 - 5\%$ correspond to most central collisions, whereas higher classes do arise from higher impact parameters.

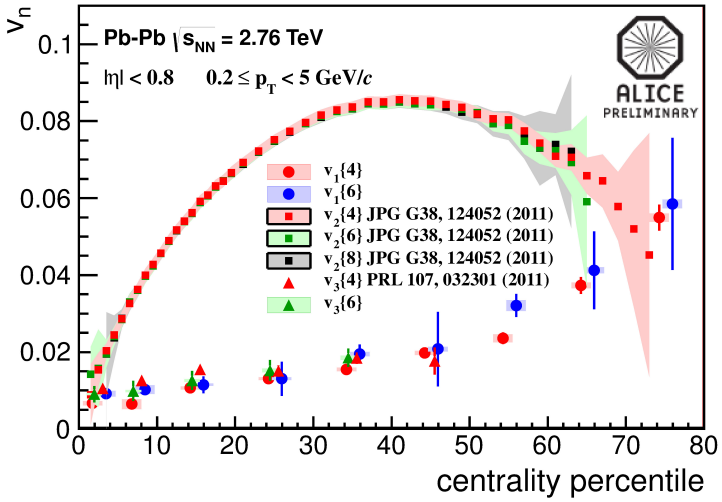

Figure 2.34.: Centrality dependence of v_1, v_2 and v_3. Taken from [58].

As one can see for most central collisions all anisotropic flow coefficients are of equal size. In this regime the coefficients origin is mostly fluctuations, which are equal for all orders. As the centrality rises –and therefore b as well – the v_2 coefficient starts to dominate due to the situation plotted in figure 2.33, where the ellipticity is the most prominent asymmetry. For more peripheral collisions the v_2 coefficients decrease again, due to the fact that the overlap region decreases and becomes fluctuation-dominated again.

Since we do not simulate the whole collision process from the initial overlap of the nuclei until the detection, we are not reproducing plots like 2.34. We are rather interested in the p_t dependence of the flow coefficients. Experimental measurements taken from lead lead

collisions for such dependence are shown in figure 2.35.

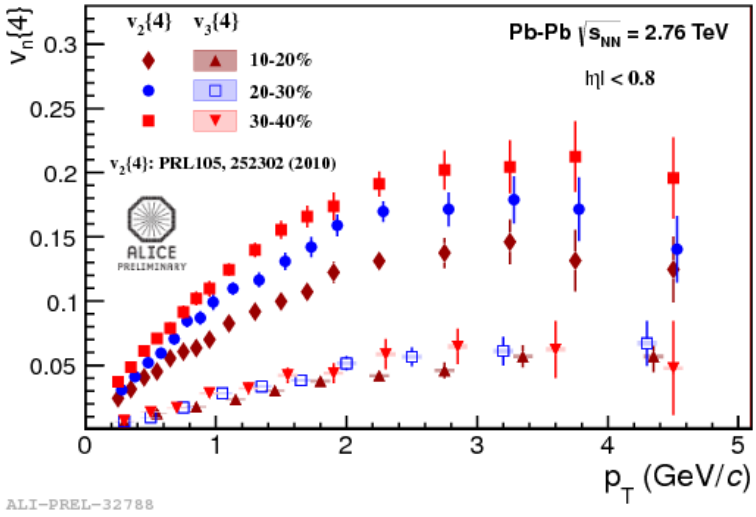

Figure 2.35.: Tranverse momentum dependence of v_2 and v_3. Taken from [58].

As one can see the flow coefficients are increasing with the modulus of the transverse momentum up to roughly 3 GeV. At a momentum scale of roughly 2 GeV they start to saturate until they even decrease. At this point the upper limit of the collective or soft p_t scale is reached. Of course the p_t scale depends on the initially deposed energy and therefore on the collision energy as well. Within our framework we should be able to mimic the flow coefficients collective behavior up to 2 GeV for such high collision energies shown in figure 2.35.

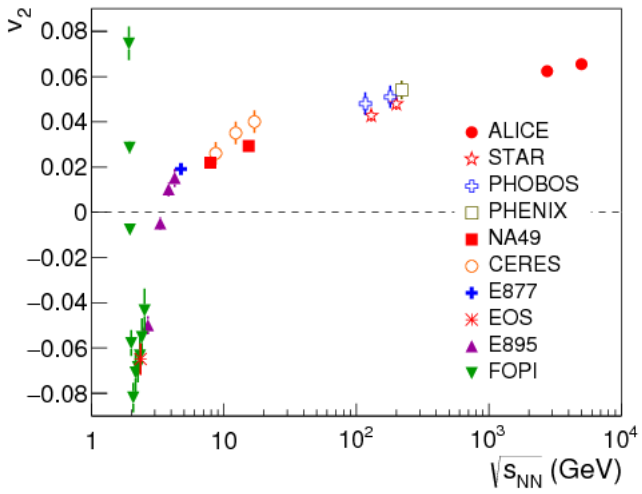

Figure 2.36.: Dependence of the p_t integrated v_2 on collision energy. Taken from [59].

As a last remark we want to mention that the p_t-integrated anisotropic flow also depends on the collision energy. Figure 2.36 shows the value of the integrated v_2 over a large interval of collision energies. In this plot one can see that the dependence of v_2 on the collision energy is non trivial. The negative values at small energies are arising, since for such small energies the spectators are shielding the medium from expanding into the direction $\phi_p - \psi_2 = 0$.

2.9.4. Anisotropic flow coefficients v_n from an isotropic fluid

In order to compute the anisotropic flow coefficients we calculated formula (2.9.9) for the Jüttner distribution. Since we already performed the particle momentum spectra determination, here we just need to compute the convolution with the $\cos(n\phi)$ terms. Note that our blast wave model factors V_n given in formulas (2.9.3)-(2.9.5) mimic now a nontrivial flow profile in ϕ_p-direction in order to gain a non vanishing signal for the observable v_n. For the computations we choose the coefficients $V_2 = V_3 = 0.1$ and $V_{n\geq 4} = 0$, since again we just want to test the applicability of our elaborated anisotropic kinetic freeze out procedure. A fine-tuning of these parameters in order to fit experimental data is not our aim at this point. But in general one could relate these parameters for example to centrality classes.

If we now compute the pion flow coefficients starting from v_2 up to v_5 emitted from an Jüttner distributed fluid element for different temperatures at the freeze out hypersurface we get the following diagrams.

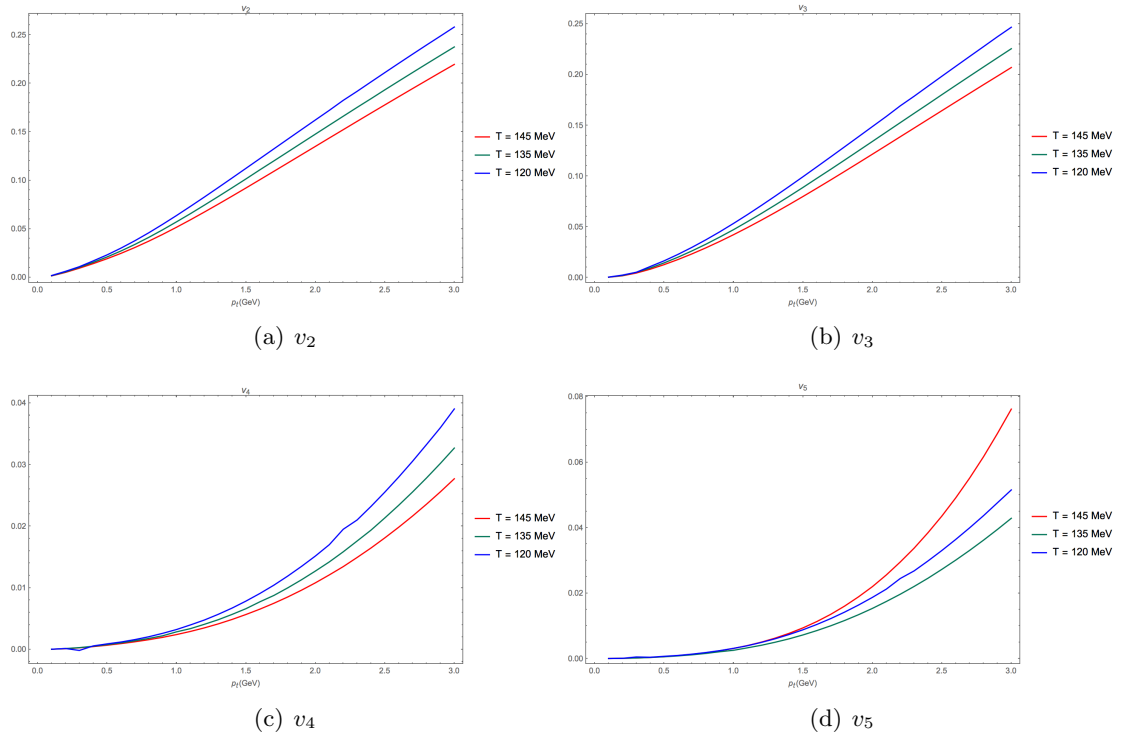

(a) v_2 (b) v_3

(c) v_4 (d) v_5

Figure 2.37.: Plot of the harmonic flow coefficients v_2, v_3, v_4, v_5 for different temperatures at the freeze out hypersurface Σ, emitted from a Jüttner distribution for pions.

As the reader can see the value for the flow coefficients depends very much on the temperature at freeze out. In addition if one compares the plots with the experimental data

one sees that we do not mimic the saturation. This is due to our simple model, which just describes the physics below the saturation sets in.

2.9.5. Anisotropic flow coefficients v_n from $F_{fs}(x^\mu, p^i)$

In order to further investigate the effect of the anisotropic freeze out procedure we present in this section the same harmonic flow coefficients v_2, v_3, v_4 and v_5, but now under the assumption that the particles are emitted from the anisotropic $F_{fs}(x^\mu, p^i)$ distribution. After implementing the distribution function but keeping the blast wave parameters fixed at the above chosen values, we computed the plots shown in figures 2.38 - 2.40.

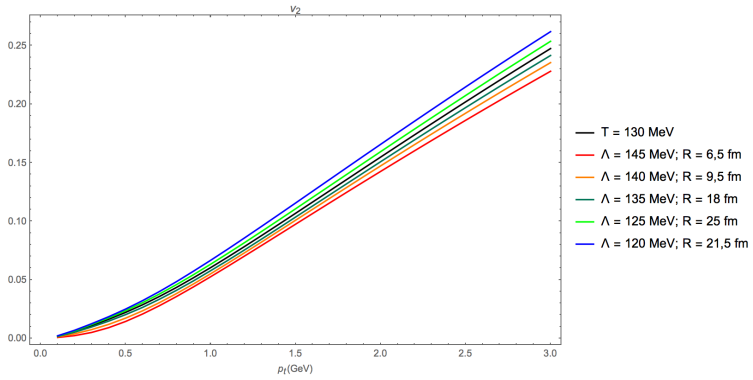

Figure 2.38.: Plot of the harmonic flow coefficient v_2 for different anisotropic temperatures at the freeze out hypersurface Σ, emitted from $F_{fs}(x^\mu, p^i)$ pion distribution.

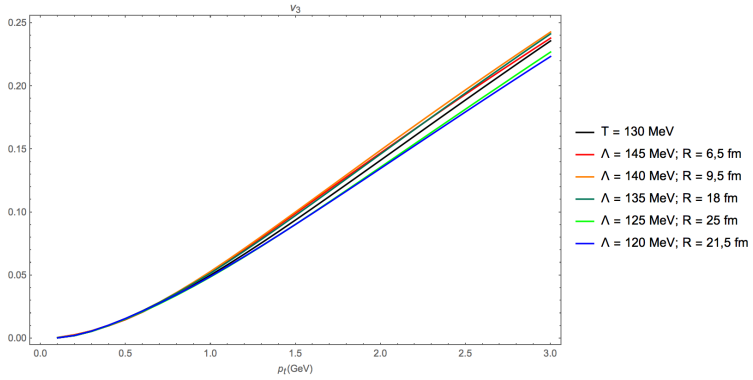

Figure 2.39.: Plot of the harmonic flow coefficient v_3 for different anisotropic temperatures at the freeze out hypersurface Σ, emitted from $F_{fs}(x^\mu, p^i)$ pion distribution.

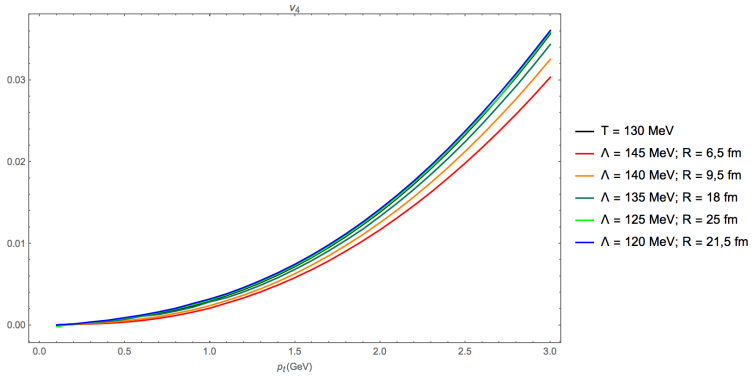

Figure 2.40.: Plot of the harmonic flow coefficient v_4 for different anisotropic temperatures at the freeze out hypersurface Σ, emitted from $F_{fs}(x^\mu, p^i)$ pion distribution.

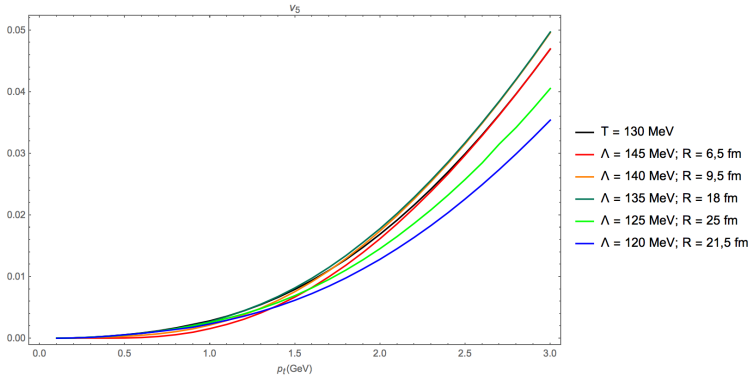

Figure 2.41.: Plot of the harmonic flow coefficient v_5 for different anisotropic temperatures at the freeze out hypersurface Σ, emitted from $F_{fs}(x^\mu, p^i)$ pion distribution.

The black curve in figures 2.38 - 2.40 indicates again the isotropic reference state. Note that we did not optimize the value of R, but just took the values obtained from the momentum spectra "fitting". As we can see the values for the observable v_n have a less strong dependence on the freeze out temperature than in figure 2.37. This is, beside the particle spectrum, another example for the smoothness of our anisotropic freeze out formalism.

2.10. Discussion and outlook

In the previous sections we discussed several main experimental observables. In addition we computed this observables arising from the derived distribution function $F_{fs}(x^\mu, p^i)$. As we saw both, particle spectrum and various anisotropic flow coefficients are rather insensitive to the anisotropic temperature at freeze out. In our view, this is preferable to approaches that necessitate a very specific freeze-out temperature that corresponds to no know feature in the phase diagram of strong interacting matter. At the risk of repeating ourselves, the Cooper-Frye formula is introduced for switching from one description to another one. But it does not reflect a sharp physical transition.

In addition we saw that in order to make a stronger statement about our freeze out model, instead of fitting the characteristic scale of the parameter R, we should simulate the expansion on a spacetime grid and let r/R emerge from the simulation. This would in addition even more emphasize the smoothness of our freeze out procedure.

After this is achieved one can investigate the observables to see if not only the trend, but also the amplitudes of the observables agree with measurements from the experiments.

3

Era of last rescatterings

3.1. Computing the different moments of the massless Boltzmann equation within 1^{st} linearization

This part is inspired by the article "Steady Expansion of a Gas into a Vacuum" of R. H. Edwards and H. K. Cheng [60]. Although they did studies on classical flow of particles in cylindrical symmetries, whereas we are interested in a relativistic formulation in order to apply the resulting formalism to high energy physics.

We are now searching for the evolution of a cylindrical (Bjorken-flow) symmetric, steady expanding system in the case of weakly interacting particles.

Whereas in the prior sections we only calculated the steady state dynamics of non-interacting particles in the case of a source sitting in the origin, we now want to go "backwards" in the evolution and investigate the era of "last interactions", which is also called "eremitic expansion" [29] by other authors. We achieve this by implementing the relaxation time approximation ansatz (2.4.9) for the collision term of the Boltzmann equation. We get the corresponding – less trivial – dynamics by computing various moments of the following Boltzmann equation in relaxation time approximation.

$$\left[p^r\partial_r - \frac{2}{r}p^r p^\phi \frac{\partial}{\partial p^\phi} + r p^\phi p^\phi \frac{\partial}{\partial p^r}\right] f(x^\mu, p^i) = \frac{1}{\tau_{rel}}\left(F_{fs}(x^\mu, p^i) - f(x^\mu, p^i)\right) \tag{3.1.1}$$

Here $F_{fs}(x^\mu, p^i)$ is the already discussed free streaming solution, τ_{rel} represents the relaxation time, which is assumed to be momentum independent. Of course, since we construct everything to be time independent, here the parameter τ_{rel} can be thought of being proportional to a relaxation length scale r_{rel}, via ${}^{r_{rel}}/_{c} = \tau_{rel}$. Additionally the system is assumed to be cylindrical symmetric and settled in the mid-rapidity region, which can be seen by the non-appearance of the corresponding gradients in formula (3.1.1).

Note that in equation (3.1.1) the right hand side is taken to be linear in $f(x^\mu, p^i)$. In other words we are working within the first linearization of the collision integral.

It is important to notice, that we do not linearize around the equilibrium state, like it is usually done, but we linearize around the free streaming solution $F_{fs}(x^\mu, p^i)$. This is an attempt to approach the area of non zero inverse Knudsen number Kn^{-1}.

For dealing with the moments please keep the definitions (2.6.13) and (2.6.15) in mind.

Since we want to elaborate a hydrodynamic like theory, which describes the flow of energy

we will match the second moments, namely the energy-momentum tensor components instead of the first moments, which would lead to Eckart-frame description. Whenever we use this fact throughout the computations we will denote this by the label *matching*. The physical energy density and the pressures components are again defined as follows.

$$\epsilon = \int \frac{d^3p}{2\tau r p^\tau} p^\tau p^\tau f(x^\mu, p^i) \tag{3.1.2}$$

$$\mathcal{P}^r = \int \frac{d^3p}{2\tau r p^\tau} p^r p^r f(x^\mu, p^i) \tag{3.1.3}$$

$$\mathcal{P}^\phi = r^2 \int \frac{d^3p}{2\tau r p^\tau} p^\phi p^\phi f(x^\mu, p^i) \tag{3.1.4}$$

$$\mathcal{P}^{\eta_s} = \tau^2 \int \frac{d^3p}{2\tau r p^\tau} p^{\eta_s} p^{\eta_s} f(x^\mu, p^i) \tag{3.1.5}$$

The corresponding fields of the first moment, namely the particle four current, are defined as follows.

$$n = \int \frac{d^3p}{2\tau r p^\tau} p^\tau f(x^\mu, p^i) \tag{3.1.6}$$

$$N^r = \nu^r = \int \frac{d^3p}{2\tau r p^\tau} p^r f(x^\mu, p^i) \tag{3.1.7}$$

$$N^\phi = \nu^\phi = \int \frac{d^3p}{2\tau r p^\tau} p^\phi f(x^\mu, p^i) \tag{3.1.8}$$

$$N^{\eta_s} = \nu^{\eta_s} = \int \frac{d^3p}{2\tau r p^\tau} p^{\eta_s} f(x^\mu, p^i) \tag{3.1.9}$$

Note that we will from now on omit the notation of the distribution function's dependence on the position and momentum variables in order to obtain shorter formulas.

In the following sections we will present the computations for the zeroth, first and second moments. As we already did above we will present the first computation in a detailed way, while presenting the following, similar ones shorter.

3.1.1. 0^{th}-moment of the Boltzmann-equation in RTA

The zeroth moment of the whole Boltzmann equation (3.1.1) with the proper symmetries and a relaxation ansatz for the right hand side provides the evolution equation of the first moment of the distribution function. It reads as written in the next formula.

$$\int \frac{d^3p}{2\tau r p^\tau} \left[p^r \partial_r - \frac{2}{r} p^r p^\phi \frac{\partial}{\partial p^\phi} + r p^\phi p^\phi \frac{\partial}{\partial p^r} \right] f = \frac{1}{\tau_{rel}} \int_{-\infty}^{\infty} \frac{d^3p}{2\tau r p^\tau} (F_{fs} - f)$$

Assuming that the distribution function f is continuous, we can exchange the derivatives and the integrals, while taking care that we do not exchange derivatives with respect to r and factors of r. Be aware that also in the p^τ there are r and p^i dependencies hidden. In addition we multiply the equation by a factor of two.

$$\begin{aligned}
\Leftrightarrow\quad & \frac{1}{r}\partial_r \int \frac{d^3p}{\tau r p^\tau} r p^r f + \frac{1}{r}\int \frac{d^3p}{\tau r}\frac{r^2 p^\phi p^\phi p^r}{(p^\tau)^3} f - \frac{2}{r}\int \frac{d^3p}{\tau r p^\tau}\frac{\partial}{\partial p^\phi}\left(p^r p^\phi f\right) \\
& + \frac{2}{r}\int \frac{d^3p}{\tau r p^\tau}(p^r f) + r\int \frac{d^3p}{\tau r}\frac{\partial}{\partial p^r}\frac{p^\phi p^\phi}{p^\tau} f + r\int \frac{d^3p}{\tau r}\frac{p^r p^\phi p^\phi}{(p^\tau)^3} f \\
& = \frac{1}{\tau_{rel}}\int \frac{d^3p}{\tau r p^\tau}(F_{fs} - f)
\end{aligned}$$

After performing parts of the r-derivative, this expression can be simplified, since some summands are canceling each other.

$$\begin{aligned}
\Leftrightarrow\quad & \frac{3}{r}\int \frac{d^3p}{\tau r p^\tau} p^r f + \partial_r \int \frac{d^3p}{\tau r p^\tau} p^r f + \int \frac{d^3p}{\tau r}\frac{r p^r p^\phi p^\phi}{(p^\tau)^3} f - \frac{2}{r}\int \frac{d^3p}{\tau r}\frac{\partial}{\partial p^\phi}\frac{p^r p^\phi}{p^\tau} f \\
& - 2\int \frac{d^3p}{\tau r}\frac{r p^r p^\phi p^\phi}{(p^\tau)^3} f + r\int \frac{d^3p}{\tau r}\frac{\partial}{\partial p^r}\frac{p^\phi p^\phi}{p^\tau} f + r\int \frac{d^3p}{\tau r}\frac{p^r p^\phi p^\phi}{(p^\tau)^3} f \\
& = \frac{1}{\tau_{rel}}\int \frac{d^3p}{\tau r p^\tau}(F_{fs} - f) \\
\Leftrightarrow\quad & \frac{3}{r}\int \frac{d^3p}{\tau r p^\tau} p^r f + \partial_r \int \frac{d^3p}{\tau r p^\tau} p^r f - \frac{2}{r}\int \frac{d^3p}{\tau r}\frac{\partial}{\partial p^\phi}\frac{p^r p^\phi}{p^\tau} f + r\int \frac{d^3p}{\tau r}\frac{\partial}{\partial p^r}\frac{p^\phi p^\phi}{p^\tau} f \\
& = \frac{1}{\tau_{rel}}\int \frac{d^3p}{\tau r p^\tau}(F_{fs} - f)
\end{aligned}$$

Since the distribution function f is assumed to be normalized, the two last terms on the left hand side, built up by an integral and a derivative of the same variable, are vanishing.

$$\Leftrightarrow\quad \partial_r \int \frac{d^3p}{\tau r p^\tau} p^r f + \frac{1}{r}\int \frac{d^3p}{\tau r p^\tau} p^r f = \frac{1}{\tau_{rel}}\int \frac{d^3p}{\tau r p^\tau}(F_{fs} - f)$$

Now one can make use of the definition of the particle four current components (3.1.7) in order to gain an evolution equation which governs the dynamics of the corresponding field.

$$\begin{aligned}
\Leftrightarrow\quad & \partial_r N^r + \frac{1}{r}N^r = \frac{1}{\tau_{rel}}\int \frac{d^3p}{2\tau r p^\tau}(F_{fs} - f) \\
\overset{(2.7.8)}{\Leftrightarrow}\quad & \partial_r N^r + \frac{1}{r}N^r = \frac{1}{\tau_{rel}}\left[\frac{2\pi C T^2 R}{\tau r^2}\arctan\left(\frac{r}{R}\right) - \int \frac{d^3p}{2\tau r p^\tau} f\right]
\end{aligned} \tag{3.1.10}$$

3.1.2. 1^{st}-moment wrt p^τ of the Boltzmann-equation in RTA

In this subsection we will compute the first moment of the Boltzmann equation with respect to p^τ. This will contribute to the spacial evolution of the particle density n.

$$
\begin{aligned}
& \int \frac{d^3p}{2\tau r p^\tau} p^\tau \left[p^r \partial_r - \frac{2}{r} p^r p^\phi \frac{\partial}{\partial p^\phi} + r p^\phi p^\phi \frac{\partial}{\partial p^r} \right] f = \frac{1}{\tau_{rel}} \int \frac{d^3p}{2\tau r p^\tau} p^\tau (F_{fs} - f) \\
\Leftrightarrow \quad & \frac{1}{r} \partial_r \int \frac{d^3p}{\tau r} r p^r f - \frac{2}{r} \int \frac{d^3p}{\tau r} \frac{\partial}{\partial p^\phi} p^r p^\phi f + \frac{2}{r} \int \frac{d^3p}{\tau r} p^r f + r \int \frac{d^3p}{\tau r} \frac{\partial}{\partial p^r} p^\phi p^\phi f \\
& = \frac{1}{\tau_{rel}} \int \frac{d^3p}{\tau r} (F_{fs} - f) \\
\overset{(2.7.9)}{\Leftrightarrow} \quad & \partial_r \int \frac{d^3p}{\tau r} p^r f + \frac{1}{r} \int \frac{d^3p}{\tau r} p^r f = \frac{1}{\tau_{rel}} \left[\frac{4\pi C T^3}{\tau r \sqrt{1 + \frac{r^2}{R^2}}} - n \right] \\
\overset{P.I.+(3.1.6)}{\Leftrightarrow} \quad & \partial_r n + \frac{n}{r} = \frac{-1}{\tau_{rel}} \left[\frac{4\pi C T^3}{\tau r \sqrt{1 + \frac{r^2}{R^2}}} - n \right]
\end{aligned} \tag{3.1.11}
$$

Note that in the last step we employ the integration by parts with respect to p^r. With this we can get rid of the factor of p^r in front of the distribution function f.

3.1.3. 1^{st}-moment wrt p^ϕ of the Boltzmann-equation in RTA

For computing the next three moments it it useful to remember that the integral over the free streaming solution F_{fs} vanishes due to the same symmetry reasons as in all the above computations.

$$
\begin{aligned}
& \int \frac{d^3p}{2\tau r p^\tau} p^\phi \left[p^r \partial_r - \frac{2}{r} p^r p^\phi \frac{\partial}{\partial p^\phi} + r p^\phi p^\phi \frac{\partial}{\partial p^r} \right] f = \frac{1}{2\tau_{rel}} \int \frac{d^3p}{\tau r p^\tau} p^\phi (F_{fs} - f) \\
\Leftrightarrow \quad & \frac{1}{r} \partial_r \int \frac{d^3p}{\tau r p^\tau} r p^r p^\phi f + \frac{1}{r} \int \frac{d^3p}{\tau r} \frac{r^2 p^r p^\phi p^\phi p^\phi}{(p^\tau)^3} f - \frac{2}{r} \int \frac{d^3p}{\tau r p^\tau} \frac{\partial}{\partial p^\phi} \left(p^r p^\phi p^\phi f \right) \\
& + \frac{4}{r} \int \frac{d^3p}{\tau r p^\tau} p^r p^\phi f + r \int \frac{d^3p}{\tau r} \frac{\partial}{\partial p^r} \frac{p^\phi p^\phi p^\phi}{p^\tau} f + r \int \frac{d^3p}{\tau r} \frac{p^r p^\phi p^\phi p^\phi}{(p^\tau)^3} f \\
& = \frac{1}{\tau_{rel}} \int \frac{d^3p}{\tau r p^\tau} p^\phi (F_{fs} - f) \\
\Leftrightarrow \quad & \partial_r \int \frac{d^3p}{\tau r p^\tau} p^r p^\phi f + \frac{5}{r} \int \frac{d^3p}{\tau r p^\tau} p^r p^\phi f + 2r \int \frac{d^3p}{\tau r} \frac{p^r p^\phi p^\phi p^\phi}{(p^\tau)^3} f \\
& - \frac{2}{r} \int \frac{d^3p}{\tau r} \frac{\partial}{\partial p^\phi} \frac{p^r p^\phi p^\phi}{p^\tau} f - \frac{2}{r} \int \frac{d^3p}{\tau r} \frac{r^2 p^r p^\phi p^\phi p^\phi}{(p^\tau)^3} f \\
& = \frac{1}{\tau_{rel}} \int \frac{d^3p}{\tau r p^\tau} p^\phi (-f) \\
\overset{(3.1.8)}{\Leftrightarrow} \quad & \partial_r \int \frac{d^3p}{2\tau r p^\tau} p^r p^\phi f + \frac{1}{r} \int \frac{d^3p}{2\tau r p^\tau} p^r p^\phi f = -\frac{N^\phi}{\tau_{rel}}
\end{aligned} \tag{3.1.12}
$$

3.1.4. 1^{st}-moment wrt p^{η_s} of the Boltzmann-equation in RTA

In this subsection we compute the first moment of the Boltzmann equation with respect to p^{η_s}.

$$
\begin{aligned}
& \int \frac{d^3p}{2\tau r p^\tau} p^{\eta_s} \left[p^r \partial_r - \frac{2}{r} p^r p^\phi \frac{\partial}{\partial p^\phi} + r p^\phi p^\phi \frac{\partial}{\partial p^r} \right] f = \frac{1}{\tau_{rel}} \int \frac{d^3p}{2\tau r p^\tau} p^{\eta_s} (F_{fs} - f) \\
\Leftrightarrow \quad & \frac{1}{r} \partial_r \int \frac{d^3p}{\tau r p^\tau} r p^r p^{\eta_s} f + \frac{1}{r} \int \frac{d^3p}{\tau r} \frac{r^2 p^r p^\phi p^\phi p^{\eta_s}}{(p^\tau)^3} f - \frac{2}{r} \int \frac{d^3p}{\tau r p^\tau} \frac{\partial}{\partial p^\phi} \left(p^r p^\phi p^{\eta_s} f \right) \\
& + \frac{2}{r} \int \frac{d^3p}{\tau r p^\tau} p^r p^{\eta_s} f + r \int \frac{d^3p}{\tau r} \frac{\partial}{\partial p^r} \frac{p^\phi p^\phi p^{\eta_s}}{p^\tau} f + r \int \frac{d^3p}{\tau r} \frac{p^r p^\phi p^\phi p^{\eta_s}}{(p^\tau)^3} f \\
& = \frac{1}{\tau_{rel}} \int \frac{d^3p}{\tau r p^\tau} p^{\eta_s} (F_{fs} - f) \\
\Leftrightarrow \quad & \partial_r \int \frac{d^3p}{\tau r p^\tau} p^r p^{\eta_s} f + \frac{3}{r} \int \frac{d^3p}{\tau r p^\tau} p^r p^{\eta_s} f + \frac{2}{r} \int \frac{d^3p}{\tau r} \frac{r^2 p^r p^\phi p^\phi p^{\eta_s}}{(p^\tau)^3} f \\
& - \frac{2}{r} \int \frac{d^3p}{\tau r} \frac{\partial}{\partial p^\phi} \frac{p^r p^\phi p^{\eta_s}}{p^\tau} f - \frac{2}{r} \int \frac{d^3p}{\tau r} \frac{r^2 p^r p^\phi p^\phi p^{\eta_s}}{(p^\tau)^3} f \\
& = - \frac{1}{\tau_{rel}} \int \frac{d^3p}{\tau r p^\tau} p^{\eta_s} f \\
\overset{(3.1.9)}{\Leftrightarrow} \quad & \partial_r \int \frac{d^3p}{2\tau r p^\tau} p^r p^{\eta_s} f + \frac{1}{r} \int \frac{d^3p}{2\tau r p^\tau} p^r p^{\eta_s} f = - \frac{N^{\eta_s}}{\tau_{rel}}
\end{aligned}
\tag{3.1.13}
$$

3.1.5. 1^{st}-moment wrt p^r of the Boltzmann-equation in RTA

$$
\begin{aligned}
& \int \frac{d^3p}{2\tau r p^\tau} p^r \left[p^r \partial_r - \frac{2}{r} p^r p^\phi \frac{\partial}{\partial p^\phi} + r p^\phi p^\phi \frac{\partial}{\partial p^r} \right] f = \frac{1}{\tau_{rel}} \int \frac{d^3p}{2\tau r p^\tau} p^r (F_{fs} - f) \\
\Leftrightarrow \quad & \frac{1}{r} \partial_r \int \frac{d^3p}{\tau r p^\tau} r p^r p^r f + \int \frac{d^3p}{\tau r} \frac{r p^r p^r p^\phi p^\phi}{(p^\tau)^3} f - \frac{2}{r} \int \frac{d^3p}{\tau r} \frac{\partial}{\partial p^\phi} \frac{p^r p^r p^\phi}{p^\tau} f \\
& - 2 \int \frac{d^3p}{\tau r} \frac{r p^r p^r p^\phi p^\phi}{(p^\tau)^3} f + \frac{2}{r} \int \frac{d^3p}{\tau r p^\tau} p^r p^r f + r \int \frac{d^3p}{\tau r p^\tau} \frac{\partial}{\partial p^r} p^r p^\phi p^\phi f \\
& - r \int \frac{d^3p}{\tau r p^\tau} p^\phi p^\phi f = \frac{1}{\tau_{rel}} \int \frac{d^3p}{\tau r p^\tau} p^r (F_{fs} - f) \\
\Leftrightarrow \quad & \partial_r \mathcal{P}_r + \frac{\mathcal{P}_r}{r} - \frac{\mathcal{P}_\phi}{r} = \frac{-1}{\tau_{rel}} \int \frac{d^3p}{\tau r p^\tau} p^r f \\
\Leftrightarrow \quad & \partial_r \mathcal{P}_r - \frac{\mathcal{P}_\phi - \mathcal{P}_r}{r} = - \frac{N^r}{\tau_{rel}}
\end{aligned}
\tag{3.1.14}
$$

Note that in the above evolution equation (3.1.14) we have the first equation coupling second moments of the distribution function f to first moments of the distribution function f, while the second moments are diagonal elements of the energy momentum tensor. This coupling arises due to the non vanishing right hand side of the Boltzmann equation.

3.1.6. 2^{nd}-moment wrt p^τ of the Boltzmann-equation in RTA

$$
\begin{aligned}
& \int \frac{d^3p}{2\tau r p^\tau} p^\tau p^\tau \left[p^r \partial_r - \frac{2}{r} p^r p^\phi \frac{\partial}{\partial p^\phi} + r p^\phi p^\phi \frac{\partial}{\partial p^r} \right] f = \frac{1}{\tau_{rel}} \int \frac{d^3p}{2\tau r p^\tau} p^\tau p^\tau (F_{fs} - f) \\
\Leftrightarrow \quad & \int \frac{d^3p}{\tau r} p^\tau p^r \partial_r f - \frac{2}{r} \int \frac{d^3p}{\tau r} p^\tau \frac{\partial}{\partial p^\phi} (p^r p^\phi f) + \frac{2}{r} \int \frac{d^3p}{\tau r} p^\tau p^r f \\
& + r \int \frac{d^3p}{\tau r} \frac{\partial}{\partial p^r} p^\tau p^\phi p^\phi f - \int \frac{d^3p}{\tau r} \frac{r p^r p^\phi p^\phi}{p^\tau} f = \frac{1}{\tau_{rel}} \int \frac{d^3p}{\tau r} p^\tau (F_{fs} - f) \\
\Leftrightarrow \quad & \frac{1}{r} \partial_r \int \frac{d^3p}{\tau r} r p^\tau p^r f - \int \frac{d^3p}{\tau r} \frac{r p^r p^\phi p^\phi}{p^\tau} f - \frac{2}{r} \int \frac{d^3p}{\tau r} \frac{\partial}{\partial p^\phi} p^\tau p^r p^\phi f \\
& + \frac{2}{r} \int \frac{d^3p}{\tau r} p^\tau p^r f + 2 \int \frac{d^3p}{\tau r} \frac{r p^r p^\phi p^\phi}{p^\tau} f - \int \frac{d^3p}{\tau r} \frac{r p^r p^\phi p^\phi}{p^\tau} f \\
& = \frac{1}{\tau_{rel}} \int \frac{d^3p}{\tau r p^\tau} p^\tau p^\tau (F_{fs} - f) \\
\Leftrightarrow \quad & \partial_r \int \frac{d^3p}{\tau r} p^\tau p^r f + \frac{1}{r} \int \frac{d^3p}{\tau r} p^\tau p^r f \overset{matching}{=} 0
\end{aligned}
\tag{3.1.15}
$$

In the last step we employed for the first time the concept of matching. The basic idea is that we choose the departure state f to have the same pressure components and the same energy density as the state the system is approaching through collisions. This guarantees that we are moving along these quantities. Another possible matching would be to move along the particles, which would result in vanishing first moment collisional contributions in equations (3.1.11)-(3.1.14). Of course one could also perform no matching, which would result in more cumbersome equations, which do not have any further information.

3.1.7. 2^{nd}-moment wrt p^ϕ of the Boltzmann-equation in RTA

$$
\begin{aligned}
& \int \frac{d^3p}{2\tau r p^\tau} p^\phi p^\phi \left[p^r \partial_r - \frac{2}{r} p^r p^\phi \frac{\partial}{\partial p^\phi} + r p^\phi p^\phi \frac{\partial}{\partial p^r} \right] f = \frac{1}{\tau_{rel}} \int \frac{d^3p}{2\tau r p^\tau} p^\phi p^\phi (F_{fs} - f) \\
\Leftrightarrow \quad & \frac{1}{r} \partial_r \int \frac{d^3p}{\tau r} \frac{r p^r p^\phi p^\phi}{p^\tau} f + \int \frac{d^3p}{\tau r} \frac{r p^r p^\phi p^\phi p^\phi p^\phi}{(p^\tau)^3} f - \frac{2}{r} \int \frac{d^3p}{\tau r p^\tau} \frac{\partial}{\partial p^\phi} \left(p^r p^\phi p^\phi p^\phi \right) f \\
& + \frac{2}{r} \int \frac{d^3p}{\tau r p^\tau} 3 p^r p^\phi p^\phi f + r \int \frac{d^3p}{\tau r} \frac{\partial}{\partial p^r} \frac{p^\phi p^\phi p^\phi p^\phi}{p^\tau} f + r \int \frac{d^3p}{\tau r} \frac{p^r p^\phi p^\phi p^\phi p^\phi}{(p^\tau)^3} f \\
& = \frac{1}{\tau_{rel}} \int \frac{d^3p}{\tau r p^\tau} p^\phi p^\phi (F_{fs} - f) \\
\Leftrightarrow \quad & \partial_r \int \frac{d^3p}{\tau r p^\tau} p^r p^\phi p^\phi f + \frac{1}{r} \int \frac{d^3p}{\tau r p^\tau} p^r p^\phi p^\phi f + \frac{1}{r} \int \frac{d^3p}{\tau r} \frac{r p^r p^\phi p^\phi p^\phi p^\phi}{(p^\tau)^3} f \\
& - \frac{2}{r} \int \frac{d^3p}{\tau r} \frac{\partial}{\partial p^\phi} \frac{p^r p^\phi p^\phi p^\phi}{p^\tau} f - 2 \int \frac{d^3p}{\tau r} \frac{r p^r p^\phi p^\phi p^\phi p^\phi}{(p^\tau)^3} f + \frac{6}{r} \int \frac{d^3p}{\tau r p^\tau} p^r p^\phi p^\phi f \\
& + r \int \frac{d^3p}{\tau r} \frac{\partial}{\partial p^r} \frac{p^\phi p^\phi p^\phi p^\phi}{p^\tau} f + r \int \frac{d^3p}{\tau r} \frac{p^r p^\phi p^\phi p^\phi p^\phi}{(p^\tau)^3} f = \frac{1}{\tau_{rel}} \int \frac{d^3p}{\tau r p^\tau} p^\phi p^\phi (F_{fs} - f) \\
\Leftrightarrow \quad & \partial_r \int \frac{d^3p}{\tau r p^\tau} p^r p^\phi p^\phi f + \frac{1}{r} \int \frac{d^3p}{\tau r p^\tau} p^r p^\phi p^\phi f \overset{matching}{=} 0
\end{aligned}
\tag{3.1.16}
$$

3.1.8. 2^{nd}-moment wrt p^{η_s} of the Boltzmann-equation in RTA

$$
\begin{aligned}
&\int \frac{d^3p}{2\tau r p^\tau} p^{\eta_s} p^{\eta_s} \left[p^r \partial_r - \frac{2}{r} p^r p^\phi \frac{\partial}{\partial p^\phi} + r p^\phi p^\phi \frac{\partial}{\partial p^r} \right] f = \frac{1}{\tau_{rel}} \int \frac{d^3p}{2\tau r p^\tau} p^{\eta_s} p^{\eta_s} (F_{fs} - f) \\
\Leftrightarrow\ & \frac{1}{r} \partial_r \int \frac{d^3p}{\tau r p^\tau} r p^r p^{\eta_s} p^{\eta_s} f + \int \frac{d^3p}{\tau r} \frac{r p^r p^\phi p^\phi p^{\eta_s} p^{\eta_s}}{(p^{\eta_s})^3} f - \frac{2}{r} \int \frac{d^3p}{\tau r p^\tau} \frac{\partial}{\partial p^\phi} p^r p^\phi p^{\eta_s} p^{\eta_s} f \\
& + \frac{2}{r} \int \frac{d^3p}{\tau r p^\tau} p^r p^{\eta_s} p^{\eta_s} f + r \int \frac{d^3p}{\tau r} \frac{\partial}{\partial p^r} \frac{p^\phi p^\phi p^{\eta_s} p^{\eta_s}}{p^\tau} f + r \int \frac{d^3p}{\tau r} \frac{p^r p^\phi p^\phi p^{\eta_s} p^{\eta_s}}{(p^\tau)^3} f \\
& = \frac{1}{\tau_{rel}} \int \frac{d^3p}{\tau r p^\tau} p^{\eta_s} p^{\eta_s} (F_{fs} - f) \\
\Leftrightarrow\ & \frac{1}{r} \partial_r \int \frac{d^3p}{\tau r p^\tau} r p^r p^{\eta_s} p^{\eta_s} f + \int \frac{d^3p}{\tau r} \frac{r p^r p^\phi p^\phi p^{\eta_s} p^{\eta_s}}{(p^\tau)^3} f - \frac{2}{r} \int \frac{d^3p}{\tau r} \frac{\partial}{\partial p^\phi} \frac{p^r p^\phi p^{\eta_s} p^{\eta_s}}{p^\tau} f \\
& - 2 \int \frac{d^3p}{\tau r} \frac{r p^r p^\phi p^\phi p^{\eta_s} p^{\eta_s}}{(p^\tau)^3} f + \frac{2}{r} \int \frac{d^3p}{\tau r p^\tau} p^r p^{\eta_s} p^{\eta_s} f + r \int \frac{d^3p}{\tau r} \frac{\partial}{\partial p^r} \frac{p^\phi p^\phi p^{\eta_s} p^{\eta_s}}{p^\tau} f \\
& + r \int \frac{d^3p}{\tau r} \frac{p^r p^\phi p^\phi p^{\eta_s} p^{\eta_s}}{(p^\tau)^3} f = \frac{1}{\tau_{rel}} \int \frac{d^3p}{\tau r p^\tau} p^{\eta_s} p^{\eta_s} (F_{fs} - f) \\
\Leftrightarrow\ & \partial_r \int \frac{d^3p}{\tau r p^\tau} p^r p^{\eta_s} p^{\eta_s} f + \frac{1}{r} \int \frac{d^3p}{\tau r p^\tau} p^r p^{\eta_s} p^{\eta_s} f \overset{matching}{=} 0
\end{aligned}
\tag{3.1.17}
$$

3.1.9. 2^{nd}-moment wrt p^r of the Boltzmann-equation in RTA

$$
\begin{aligned}
&\int \frac{d^3p}{2\tau r p^\tau} p^r p^r \left[p^r \partial_r - \frac{2}{r} p^r p^\phi \frac{\partial}{\partial p^\phi} + r p^\phi p^\phi \frac{\partial}{\partial p^r} \right] f = \frac{1}{\tau_{rel}} \int \frac{d^3p}{2\tau r p^\tau} p^r p^r (F_{fs} - f) \\
\Leftrightarrow\ & \frac{1}{r} \partial_r \int \frac{d^3p}{\tau r p^\tau} \frac{r p^r p^r p^r}{p^\tau} f + \int \frac{d^3p}{\tau r} \frac{r p^r p^r p^r p^\phi p^\phi}{(p^\tau)^3} f - \frac{2}{r} \int \frac{d^3p}{\tau r} \frac{p^r p^r p^r}{p^\tau} \frac{\partial}{\partial p^\phi} (p^\phi f) \\
& + \frac{2}{r} \int \frac{d^3p}{\tau r p^\tau} p^r p^r p^r f + \int \frac{d^3p}{\tau r p^\tau} \frac{\partial}{\partial p^r} r p^r p^r p^\phi p^\phi f + \int \frac{d^3p}{\tau r} \frac{p^r p^r p^r p^\phi p^\phi}{(p^\tau)^3} f \\
& - 2 \int \frac{d^3p}{\tau r p^\tau} \frac{r p^r p^\phi p^\phi}{p^\tau} f = \frac{1}{\tau_{rel}} \int \frac{d^3p}{\tau r p^\tau} p^r p^r (F_{fs} - f) \\
\Leftrightarrow\ & \frac{1}{r} \partial_r \int \frac{d^3p}{\tau r p^\tau} \frac{r p^r p^r p^r}{p^\tau} f + \int \frac{d^3p}{\tau r} \frac{r p^r p^r p^r p^\phi p^\phi}{(p^\tau)^3} f - \frac{2}{r} \int \frac{d^3p}{\tau r} \frac{\partial}{\partial p^\phi} \frac{p^r p^r p^r p^\phi}{p^\tau} f \\
& - \frac{2}{r} \int \frac{d^3p}{\tau r} \frac{r^2 p^r p^r p^r p^\phi p^\phi}{(p^\tau)^3} f + \frac{2}{r} \int \frac{d^3p}{\tau r p^\tau} p^r p^r p^r f + \int \frac{d^3p}{\tau r} \frac{\partial}{\partial p^r} \frac{r p^r p^r p^\phi p^\phi}{p^\tau} f \\
& + \int \frac{d^3p}{\tau r} \frac{r p^r p^r p^r p^\phi p^\phi}{(p^\tau)^3} f - 2 \int \frac{d^3p}{\tau r p^\tau} r p^r p^\phi p^\phi f \\
& = \frac{1}{\tau_{rel}} \int \frac{d^3p}{\tau r p^\tau} p^r p^r (F_{fs} - f) \\
\Leftrightarrow\ & \partial_r \int \frac{d^3p}{\tau r p^\tau} p^r p^r p^r f + \frac{1}{r} \int \frac{d^3p}{\tau r p^\tau} p^r p^r p^r f - 2r \int \frac{d^3p}{\tau r p^\tau} p^r p^\phi p^\phi f \\
& \overset{matching}{=} 0
\end{aligned}
\tag{3.1.18}
$$

3.1.10. Remarks

With the computed equations (3.1.10) up to (3.1.18) we have expressions for the system dynamics in the case of non vanishing particle interactions. One possibility is now to solve the system of coupled equations for f in order to get insights into the evolution of the particles. After elaborating the solution one could compute all the moments of the distribution function like we did this in the last chapter 2 in the case of the collisionless solution F_{fs}. However to solve the system of equations is nontrivial.

Therefore we will simplify our equations further with the help of phenomenological arguments and tools, in order to circumvent the mathematical challenging task to solve the above dynamics.

3.2. Closing the equations via 2^{nd}-linearization

In order to work out the equations of motion for the different moments of the Boltzmann equation in the relaxation time approximation in a closed form, we have to linearize our problem a second time. In section 2.4.11 we already sketched how such a second linearization is usually implemented. In this section we will linearize the distribution function f around the free streaming solution F_{fs}.

$$f = F_{fs} + \delta f \tag{3.2.1}$$

Further we demand the deviation δf to be small, via making the following statement.

$$F_{fs} \gg \delta f \tag{3.2.2}$$

In order to summarize the linearizations let us mention that the first linearization was a linearization of the collision kernel in f, while the second is a linearization of f itself. It is important to notice that we expand the distribution function around the free streaming solution F_{fs}, whereas most often people use the RTA to linearize around a Jüttner distribution $f_{\text{Jüt}}$ (2.4.13). This is indeed the reason, why our equations are only valid in the era of "last interactions", near the free streaming stage, where the deviations are small. Note that equation (3.2.2) quantifies the statement about the smallness of the deviation δf. In addition we demand that a similar statement (3.2.2) is true for the derivatives of the distribution functions.

Next we are going to insert the ansatz (3.2.1) into the relaxation time approximated Boltzmann equation, using the elaborated free streaming solution. In addition we neglect the p^{η_s} component in the exponent, which results in a description for the transverse plane in the mid-rapidity region. The resulting equation reads as follows.

$$\left[p^\tau \partial_\tau + p^r \partial_r + p^\phi \partial_\phi - \frac{2}{r} p^r p^\phi \frac{\partial}{\partial p^\phi} + r p^\phi p^\phi \frac{\partial}{\partial p^r}\right] (F_{fs} + \delta f) = m \frac{F_{fs} - (F_{fs} + \delta f)}{\tau_{rel}} \tag{3.2.3}$$

Due to equation (3.2.2) we neglect all derivatives of the deviation δf. Therefore we can simplify equation (3.2.3) to the following expression.

$$\left[p^\tau\partial_\tau + p^r\partial_r + p^\phi\partial_\phi - \frac{2}{r}p^r p^\phi\frac{\partial}{\partial p^\phi} + rp^\phi p^\phi\frac{\partial}{\partial p^r}\right]F_{fs} = -m\frac{\delta f}{\tau_{rel}}$$

From the above formula we can easily extract an expression for the deviation δf.

$$\delta f = -\frac{\tau_{rel}}{m}\left[p^\tau\partial_\tau + p^r\partial_r + p^\phi\partial_\phi - \frac{2}{r}p^r p^\phi\frac{\partial}{\partial p^\phi} + rp^\phi p^\phi\frac{\partial}{\partial p^r}\right]F_{fs} \tag{3.2.4}$$

Please note that in equation (3.2.4) the Knudsen number Kn is hidden. Since τ_{rel} is a (more or less) microscopical scale and the derivatives in τ are of macroscopic size the correction δf is proportional to Kn. In this regime, shortly before free streaming the Knudsen number is huge. In order to define a meaningful small parameter, one should utilize the inverse Knudsen number as the small parameter. With the help of equation (3.2.4) we can compute the linear perturbation as a function of the free streaming solution F_{fs}. As the origin of the "non-equilibriumness"[1] of the distribution function, we implement a temperature profile[2], which varies in position space $T = T(r,\phi)$. This ansatz is comparable to the computation we did in the viscous hydrodynamical section 2.6.3, where the gradients were introduced in order to generate a force.

In the following we will compute the resulting expression for the deviation of the free streaming distribution function in the above mentioned scenario.

$$\delta f = -\frac{\tau_{rel}}{m}\left[p^\tau\partial_\tau + p^r\partial_r + p^\phi\partial_\phi - \frac{2}{r}p^r p^\phi\frac{\partial}{\partial p^\phi} + rp^\phi p^\phi\frac{\partial}{\partial p^r}\right] e^{-\frac{\sqrt{m^2+p^r p^r+r^2\left(1+\frac{r^2}{R^2}\right)p^\phi p^\phi}}{T(r,\phi)}}$$

Performing the derivatives leads to the following lengthy expression.

[1],or as a force driving the system away from equilibrium,

[2]Strictly speaking this is an anisotropic temperature like profile. Nevertheless we will label this field by the letter T instead of Λ.

$$
\begin{aligned}
\delta f \;=\; & -\frac{\tau_{rel}}{m}\Bigg[-p^{\tau}\sqrt{m^2+p^r p^r+r^2\left(1+\frac{r^2}{R^2}\right)p^{\phi}p^{\phi}}\left(\partial_{\tau}\frac{1}{T}\right)\\
& -p^{r}\sqrt{m^2+p^r p^r+r^2\left(1+\frac{r^2}{R^2}\right)p^{\phi}p^{\phi}}\left(\partial_{r}\frac{1}{T}\right)\\
& -p^{r}\frac{rp^{\phi}p^{\phi}}{T\sqrt{m^2+p^r p^r+r^2\left(1+\frac{r^2}{R^2}\right)p^{\phi}p^{\phi}}}\\
& -p^{r}\frac{2r^3p^{\phi}p^{\phi}}{R^2T\sqrt{m^2+p^r p^r+r^2\left(1+\frac{r^2}{R^2}\right)p^{\phi}p^{\phi}}}\\
& -p^{\phi}\sqrt{m^2+p^r p^r+r^2\left(1+\frac{r^2}{R^2}\right)p^{\phi}p^{\phi}}\left(\partial_{\phi}\frac{1}{T}\right)\\
& -\frac{2p^r p^{\phi}}{rT}\left(-\frac{r^2\left(1+\frac{r^2}{R^2}\right)p^{\phi}}{\sqrt{m^2+p^r p^r+r^2\left(1+\frac{r^2}{R^2}\right)p^{\phi}p^{\phi}}}\right)\\
& +\frac{rp^{\phi}p^{\phi}}{T}\left(-\frac{p^r}{\sqrt{m^2+p^r p^r+r^2\left(1+\frac{r^2}{R^2}\right)p^{\phi}p^{\phi}}}\right)\Bigg]\\
& e^{-\frac{\sqrt{m^2+p^r p^r+r^2\left(1+\frac{r^2}{R^2}\right)p^{\phi}p^{\phi}}}{T(r,\phi)}}
\end{aligned}
$$

The above formula can be simplified, since some summands are canceling each other.

$$
\begin{aligned}
\delta f \;=\; & -\frac{\tau_{rel}}{m}\sqrt{m^2+p^r p^r+r^2\left(1+\frac{r^2}{R^2}\right)p^{\phi}p^{\phi}}\\
& \left[-p^{\tau}\left(\partial_{\tau}\frac{1}{T}\right)-p^{r}\left(\partial_{r}\frac{1}{T}\right)-p^{\phi}\left(\partial_{\phi}\frac{1}{T}\right)\right]F_{fs}
\end{aligned}
$$

Furthermore one can partly perform the derivative of the inverse temperature T.

$$
\delta f=-\frac{\tau_{rel}}{m}\frac{\sqrt{m^2+p^r p^r+r^2\left(1+\frac{r^2}{R^2}\right)p^{\phi}p^{\phi}}}{T^2}\left[p^{\tau}\left(\partial_{\tau}T\right)+p^{r}\left(\partial_{r}T\right)+p^{\phi}\left(\partial_{\phi}T\right)\right]F_{fs} \tag{3.2.5}
$$

With equation (3.2.5) we have an expression for the perturbation δf arising from gradients in the temperature field T. With this formula we can compute the moments of the Boltzmann equation again. In contrast to the previous approach in section 3.1 we obtained a closed expression, since we related the perturbation to the distribution, which was the starting point of the expansion (3.2.2).

3.3. Computing the moments of the dissipative, massless correction to the free-streaming solution

In this section we will further assume a ϕ-symmetry, massless particles and work only in the p^r and the p^ϕ-direction in momentum space. In other words we are working in the transverse plane. This results in a slightly changed integral measure.

Basically we compute the various moments of the deviation δf, similar to the computations worked out for the free streaming solution (2.5.5). Since we assumed in (3.2.1) the correction to be additive, the corresponding correction for the fields will be additive as well.

The resulting equations are describing the collisional contributions to the system's expansion in the regime shortly before free streaming which is the era of last rescatterings.

3.3.1. 0^{th}-moment of δf

Since we neglect the η_s-direction, the integral measure slightly changes. The zeroth moment becomes

$$I_0 \;=\; \int \frac{d^2p}{2rp^\tau}\delta f$$

Inserting the elaborated expression for the perturbation's evolution (3.2.5) leads to the subsequent expression.

$$I_0 \;=\; -\frac{\tau_{rel}}{2r}\int \frac{d^2p}{\sqrt{p^rp^r+r^2p^\phi p^\phi}}\frac{\sqrt{p^rp^r+r^2\left(1+\frac{r^2}{R^2}\right)p^\phi p^\phi}}{T^2}\left[p^\tau\left(\partial_\tau T\right)+p^r\left(\partial_r T\right)\right]F_{fs}$$

In order to compute the momentum integrals we use the substitutions (2.7.1)-(2.7.3) and insert the functional form of the two dimensional free streaming solution.

$$\begin{aligned} I_0 \;=\; & -\frac{TC\tau_{rel}}{2r\sqrt{1+\frac{r^2}{R^2}}}\int dq^r dq^\phi \frac{\sqrt{q^rq^r+q^\phi q^\phi}}{\sqrt{q^rq^r+\frac{q^\phi q^\phi}{1+\frac{r^2}{R^2}}}} \\ & \left[\sqrt{q^rq^r+\frac{q^\phi q^\phi}{1+\frac{r^2}{R^2}}}(\partial_\tau T)+(q^r\partial_r T)\right]e^{-\sqrt{q^rq^r+q^\phi q^\phi}} \end{aligned}$$

In order to simplify the exponent further we perform the substitutions (2.7.4)-(2.7.6).

$$\begin{aligned} I_0 \;=\; & -\frac{TC\tau_{rel}}{2r\sqrt{1+\frac{r^2}{R^2}}}\int_0^\infty d|q^r|\int_0^{2\pi}d\phi_q \frac{|q^r|^2e^{-|q^r|}}{|q^r|\sqrt{\cos^2(\phi_q)+\frac{\sin^2(\phi_q)}{1+\frac{r^2}{R^2}}}} \\ & \left[|q^r|\sqrt{\cos^2(\phi_q)+\frac{\sin^2(\phi_q)}{1+\frac{r^2}{R^2}}}(\partial_\tau T)+|q^r|\cos(\phi_q)(\partial_r T)\right] \end{aligned}$$

At this point the $|q^r|$-integral can be calculated.

$$I_0 = -\frac{2TC\tau_{rel}}{2r}\int_0^{2\pi} d\phi_q \frac{1}{\frac{r}{R}\cos(\phi_q)}\left[\frac{\frac{r}{R}\cos(\phi_q)}{\sqrt{1+\frac{r^2}{R^2}}}(\partial_\tau T)+\cos(\phi_q)(\partial_r T)\right]$$

In a last step we perform the ϕ_q-integral, which is indeed trivial.

$$I_0 = -\frac{2\pi TC\tau_{rel}}{r}\left[\frac{(\partial_\tau T)}{\sqrt{1+\frac{r^2}{R^2}}}+\frac{R}{r}(\partial_r T)\right] \tag{3.3.1}$$

Like in all the above sections we compute and present the following moments of δf in a compact way, since all the employed steps are already discussed in the zeroth moment computation.

3.3.2. 1^{st}-moment of δf wrt p^τ

$$\begin{aligned}
\delta N^\tau &= \int \frac{d^2p}{2rp^\tau} p^\tau \delta f \\
&= -\frac{\tau_{rel}}{2T^2 r}\int d^2p \sqrt{p^r p^r + r^2\left(1+\frac{r^2}{R^2}\right)p^\phi p^\phi} \\
&\quad \left[\sqrt{p^r p^r + r^2 p^\phi p^\phi}(\partial_\tau T)+p^r(\partial_r T)\right] F_{fs} \\
&\overset{(2.7.1)-(2.7.6)}{=} -\frac{CT^2\tau_{rel}}{2r\sqrt{1+\frac{r^2}{R^2}}}\int_0^\infty d|q^r|\int_0^{2\pi} d\phi_q |q^r|^3 e^{-|q^r|} \\
&\quad \left[\sqrt{\cos^2(\phi_q)+\frac{\sin^2(\phi_q)}{1+\frac{r^2}{R^2}}}(\partial_\tau T)+\cos(\phi_q)(\partial_r T)\right] \\
&= -\frac{6CT^2\tau_{rel}}{2r\sqrt{1+\frac{r^2}{R^2}}}\int_0^{2\pi} d\phi_q \cos(\phi_q) \\
&\quad \left[\left(\frac{\frac{r}{R}}{\sqrt{1+\frac{r^2}{R^2}}}\right)(\partial_\tau T)+(\partial_r T)\right] = 0
\end{aligned} \tag{3.3.2}$$

Note that the last step is due to the fact that the integral over cos is vanishing. This argument is employed in the computations for the following 1^{st}-moments as well.

3.3.3. 1^{st}-moment of δf wrt p^r

$$
\begin{aligned}
\delta N^r &= \int \frac{d^2p}{2rp^\tau} p^r \delta f \\
&= -\frac{\tau_{rel}}{2T^2 r} \int d^2p \frac{\sqrt{p^r p^r + r^2\left(1+\frac{r^2}{R^2}\right)p^\phi p^\phi}}{\sqrt{p^r p^r + r^2 p^\phi p^\phi}} \\
&\quad p^r \left[\sqrt{p^r p^r + r^2 p^\phi p^\phi}(\partial_\tau T) + p^r(\partial_r T)\right] F_{fs} \\
&\overset{(2.7.1)-(2.7.3)}{=} -\frac{CT^2\tau_{rel}}{2r\sqrt{1+\frac{r^2}{R^2}}} \int dq^r dq^\phi \frac{q^r\sqrt{q^r q^r + q^\phi q^\phi}}{\sqrt{q^r q^r + \frac{q^\phi q^\phi}{1+\frac{r^2}{R^2}}}} \\
&\quad \left[\sqrt{q^r q^r + \frac{q^\phi q^\phi}{1+\frac{r^2}{R^2}}}(\partial_\tau T) + q^r(\partial_r T)\right] e^{-\sqrt{q^r q^r + q^\phi q^\phi}} \\
&\overset{(2.7.4)-(2.7.6)}{=} -\frac{CT^2\tau_{rel}}{2r\sqrt{1+\frac{r^2}{R^2}}} \int_0^\infty d|q^r| \int_0^{2\pi} d\phi_q \frac{|q^r|^3 e^{-|q^r|}\cos(\phi_q)}{\sqrt{\cos^2(\phi_q) + \frac{\sin^2(\phi_q)}{1+\frac{r^2}{R^2}}}} \\
&\quad \left[\sqrt{\cos^2(\phi_q) + \frac{\sin^2(\phi_q)}{1+\frac{r^2}{R^2}}}(\partial_\tau T) + \cos(\phi_q)(\partial_r T)\right] \\
&= -\frac{3CT^2\tau_{rel}}{r} \int_0^{2\pi} d\phi_q \left[\frac{\cos(\phi_q)(\partial_\tau T)}{\sqrt{1+\frac{r^2}{R^2}}} + \frac{R}{r}\cos(\phi_q)(\partial_r T)\right] \\
&= 0
\end{aligned}
\tag{3.3.3}
$$

3.3.4. 1^{st}-moment of δf wrt p^{ϕ}

$$
\begin{aligned}
\frac{\delta N^{\phi}}{r} &= \int \frac{d^2p}{2rp^{\tau}} p^{\phi}\delta f \\
&= -\frac{\tau_{rel}}{2T^2 r}\int d^2p \frac{\sqrt{p^r p^r + r^2\left(1+\frac{r^2}{R^2}\right)p^{\phi}p^{\phi}}}{\sqrt{p^r p^r + r^2 p^{\phi}p^{\phi}}} \\
&\quad p^{\phi}\left[\sqrt{p^r p^r + r^2 p^{\phi}p^{\phi}}(\partial_{\tau}T) + p^r(\partial_r T)\right] F_{fs} \\
&\overset{(2.7.1)-(2.7.3)}{=} -\frac{CT^2\tau_{rel}}{2r^2\left(1+\frac{r^2}{R^2}\right)}\int dq^r dq^{\phi} \frac{q^{\phi}\sqrt{q^r q^r + q^{\phi}q^{\phi}}}{\sqrt{q^r q^r + \frac{q^{\phi}q^{\phi}}{1+\frac{r^2}{R^2}}}} \\
&\quad \left[\sqrt{q^r q^r + \frac{q^{\phi}q^{\phi}}{1+\frac{r^2}{R^2}}}(\partial_{\tau}T) + q^r(\partial_r T)\right] e^{-\sqrt{q^r q^r + q^{\phi}q^{\phi}}} \\
&= -\frac{CT^2\tau_{rel}}{2r^2\left(1+\frac{r^2}{R^2}\right)}\int_0^{\infty} d|q^r||q^r|^3 e^{-|q^r|}\int_0^{2\pi} d\phi_q \frac{\sin(\phi_q)}{\frac{r}{R}\cos(\phi_q)} \\
&\quad \sqrt{1+\frac{r^2}{R^2}}\left[\frac{\frac{r}{R}\cos(\phi_q)}{\sqrt{1+\frac{r^2}{R^2}}}(\partial_{\tau}T) + \cos(\phi_q)(\partial_r T)\right] \\
&= -\frac{3CT^2\tau_{rel}}{r^2\sqrt{1+\frac{r^2}{R^2}}}\int_0^{2\pi} d\phi_q \sin(\phi_q)\left[\frac{(\partial_{\tau}T)}{\sqrt{1+\frac{r^2}{R^2}}} + \frac{R}{r}(\partial_r T)\right] \\
&= 0
\end{aligned}
\tag{3.3.4}
$$

Since we work only in two space dimensions we are left with computing the second moments of the perturbation δf.

3.3.5. 2^{nd}-moment of δf wrt p^τ

$$
\begin{aligned}
\delta T^{\tau\tau} &= \int \frac{d^2p}{2rp^\tau} p^\tau p^\tau \delta f \\
&= -\frac{\tau_{rel}}{2T^2 r} \int d^2p \sqrt{p^r p^r + r^2\left(1+\frac{r^2}{R^2}\right)p^\phi p^\phi}\sqrt{p^r p^r + r^2 p^\phi p^\phi} \\
&\quad \left[\sqrt{p^r p^r + r^2 p^\phi p^\phi}(\partial_\tau T) + p^r(\partial_r T)\right] F_{fs} \\
&\overset{(2.7.1)-(2.7.3)}{=} -\frac{CT^3\tau_{rel}}{2r\sqrt{1+\frac{r^2}{R^2}}} \int dq^r dq^\phi \sqrt{q^r q^r + q^\phi q^\phi}\sqrt{q^r q^r + \frac{q^\phi q^\phi}{1+\frac{r^2}{R^2}}} \\
&\quad \left[\sqrt{q^r q^r + \frac{q^\phi q^\phi}{1+\frac{r^2}{R^2}}}(\partial_\tau T) + q^r(\partial_r T)\right] e^{-\sqrt{q^r q^r + q^\phi q^\phi}} \\
&\overset{(2.7.4)-(2.7.6)}{=} -\frac{CT^3\tau_{rel}}{2r\sqrt{1+\frac{r^2}{R^2}}} \int_0^\infty d|q^r||q^r|^4 e^{-|q^r|} \int_0^{2\pi} d\phi_q \sqrt{\cos^2(\phi_q) + \frac{\sin^2(\phi_q)}{1+\frac{r^2}{R^2}}} \\
&\quad \left[\sqrt{\cos^2(\phi_q) + \frac{\sin^2(\phi_q)}{1+\frac{r^2}{R^2}}}(\partial_\tau T) + \cos(\phi_q)(\partial_r T)\right] \\
&= -\frac{12CT^3\tau_{rel}}{r\sqrt{1+\frac{r^2}{R^2}}} \int_0^{2\pi} d\phi_q \frac{r}{R}\frac{\cos(\phi_q)}{\sqrt{1+\frac{r^2}{R^2}}} \\
&\quad \left[\frac{r}{R}\frac{\cos(\phi_q)}{\sqrt{1+\frac{r^2}{R^2}}}(\partial_\tau T) + \cos(\phi_q)(\partial_r T)\right] \\
&= -\frac{24\pi CT^3\tau_{rel}}{\tau r^2\left(1+\frac{r^2}{R^2}\right)} \left[\frac{r^2}{R^2}\frac{1}{\sqrt{1+\frac{r^2}{R^2}}}(\partial_\tau T) + \frac{r}{R}(\partial_r T)\right] \qquad (3.3.5)
\end{aligned}
$$

3.3.6. 2^{nd}-moment of δf wrt p^r

$$
\begin{aligned}
\delta T^{rr} &= \int \frac{d^2p}{2rp^\tau} p^r p^r \delta f \\
&= -\frac{\tau_{rel}}{2T^2 r}\int d^2p \sqrt{p^r p^r + r^2\left(1+\frac{r^2}{R^2}\right)p^\phi p^\phi}\,\frac{p^r p^r}{\sqrt{p^r p^r + r^2 p^\phi p^\phi}} \\
&\quad \left[\sqrt{p^r p^r + r^2 p^\phi p^\phi}(\partial_\tau T) + p^r(\partial_r T)\right] F_{fs} \\
&\overset{(2.7.1)-(2.7.3)}{=} -\frac{CT^3\tau_{rel}}{2r\sqrt{1+\frac{r^2}{R^2}}}\int dq^r dq^\phi \frac{q^r q^r \sqrt{q^r q^r + q^\phi q^\phi}}{\sqrt{q^r q^r + \frac{q^\phi q^\phi}{1+\frac{r^2}{R^2}}}} \\
&\quad \left[\sqrt{q^r q^r + \frac{q^\phi q^\phi}{1+\frac{r^2}{R^2}}}(\partial_\tau T) + q^r(\partial_r T)\right] e^{-\sqrt{q^r q^r + q^\phi q^\phi}} \\
&\overset{(2.7.4)-(2.7.6)}{=} -\frac{CT^3\tau_{rel}}{2r\sqrt{1+\frac{r^2}{R^2}}}\int_0^\infty d|q^r||q^r|^4 e^{-|q^r|}\int_0^{2\pi} d\phi_q \frac{\cos^2(\phi_q)}{\sqrt{\cos^2(\phi_q) + \frac{\sin^2(\phi_q)}{1+\frac{r^2}{R^2}}}} \\
&\quad \left[\sqrt{\cos^2(\phi_q) + \frac{\sin^2(\phi_q)}{1+\frac{r^2}{R^2}}}(\partial_\tau T) + \cos(\phi_q)(\partial_r T)\right] \\
&= -\frac{12CT^3\tau_{rel}}{r\sqrt{1+\frac{r^2}{R^2}}}\int_0^{2\pi} d\phi_q \frac{R}{r}\cos(\phi_q) \\
&\quad \left[\frac{r}{R}\frac{\cos(\phi_q)}{\sqrt{1+\frac{r^2}{R^2}}}(\partial_\tau T) + \cos(\phi_q)(\partial_r T)\right] \\
&= -\frac{12\pi CT^3\tau_{rel}}{r\sqrt{1+\frac{r^2}{R^2}}}\left[\frac{(\partial_\tau T)}{\sqrt{1+\frac{r^2}{R^2}}} + \frac{R}{r}(\partial_r T)\right] \qquad (3.3.6)
\end{aligned}
$$

3.3.7. 2^{nd}-moment of δf wrt p^ϕ

$$
\begin{aligned}
\frac{\delta T^{\phi\phi}}{r^2} &= \int \frac{d^2p}{2rp^\tau} p^\phi p^\phi \delta f \\
&= -\frac{\tau_{rel}}{2T^2 r} \int d^2p \sqrt{p^r p^r + r^2\left(1+\frac{r^2}{R^2}\right) p^\phi p^\phi} \frac{p^\phi p^\phi}{\sqrt{p^r p^r + r^2 p^\phi p^\phi}} \\
&\quad \left[\sqrt{p^r p^r + r^2 p^\phi p^\phi}(\partial_\tau T) + p^r(\partial_r T)\right] F_{fs} \\
&\overset{(2.7.1)-(2.7.3)}{=} -\frac{CT^3\tau_{rel}}{2r\sqrt{1+\frac{r^2}{R^2}}} \int dq^r dq^\phi \sqrt{q^r q^r + q^\phi q^\phi} \frac{q^\phi q^\phi}{r^2\left(1+\frac{r^2}{R^2}\right)\sqrt{q^r q^r + \frac{q^\phi q^\phi}{1+\frac{r^2}{R^2}}}} \\
&\quad \left[\sqrt{q^r q^r + \frac{q^\phi q^\phi}{1+\frac{r^2}{R^2}}}(\partial_\tau T) + q^r(\partial_r T)\right] e^{-\sqrt{q^r q^r + q^\phi q^\phi}} \\
&\overset{(2.7.4)-(2.7.6)}{=} -\frac{CT^3\tau_{rel}}{2r^3\left(1+\frac{r^2}{R^2}\right)^{\frac{3}{2}}} \int_0^\infty d|q^r||q^r|^4 e^{-|q^r|} \int_0^{2\pi} d\phi_q \frac{\sin^2(\phi_q)}{\sqrt{\cos^2(\phi_q) + \frac{\sin^2(\phi_q)}{1+\frac{r^2}{R^2}}}} \\
&\quad \left[\sqrt{\cos^2(\phi_q) + \frac{\sin^2(\phi_q)}{1+\frac{r^2}{R^2}}}(\partial_\tau T) + \cos(\phi_q)(\partial_r T)\right] \\
&= -\frac{12CT^3\tau_{rel}}{r^3\left(1+\frac{r^2}{R^2}\right)} \int_0^{2\pi} d\phi_q \sin^2(\phi_q) \left[\frac{(\partial_\tau T)}{\sqrt{1+\frac{r^2}{R^2}}} + \frac{R}{r}(\partial_r T)\right] \\
&= -\frac{12\pi CT^3\tau_{rel}}{r^3\left(1+\frac{r^2}{R^2}\right)} \left[\frac{(\partial_\tau T)}{\sqrt{1+\frac{r^2}{R^2}}} + \frac{R}{r}(\partial_r T)\right] \qquad (3.3.7)
\end{aligned}
$$

3.4. Discussion and outlook

With the expressions (3.3.1) up to (3.3.7) we have the resulting – so to say dissipative – fields, that arise from the 2^{nd}-linearization around the massless, anisotropic free streaming solution (2.5.5). As it was shown, the dissipative corrections to the particle flow are all vanishing, only the second and the zeroth moments are present in this two dimensional setup.

In order to compute the arising observables like anisotropic flow coefficients v_n from this setup – as we did for the collision-less case in section 2.9 – one needs to solve the equations (3.3.1) up to (3.3.7) on a discretized position space grid, incorporating a realistic anisotropic temperature gradient. If this is achieved, an interesting question is whether the anisotropic freeze-out including dissipative corrections due to last interactions could also reproduce measured HBT-Radii[3]. These radii are an observable arising from the femtoscopy and measure roughly speaking the size and the shape of the spacial volume, where the freeze out takes place. A computation of these radii could be done in the collision-less approach as well, but it would be somehow ill-defined.

However the above elaborated approach can be seen as a first step for developing a tool that describes the area of the green arrow in figure 2.7.

[3]HBT is an abbreviation for Hanbury-Brown and Twiss. In order to read more about this observable we refer to [61].

For the future it would be interesting to investigate whether the choice of linearizing the collision term and the distribution function, describes the system's evolution as good as a full treatment of the collision term, as it was used in [25] and in [26].

4

Azimuthally dependent two-particle correlations

4.1. Introduction

The investigation of correlations between particles is a crucial point in the heavy-ion collision research field. Correlations give a measure of the particle's "relationship" to each other. For example it could be that all particles in a created medium do not interact with others and are totally uncorrelated. The other extreme would be that all particles know at all time about all the other particles in the system[1] and evolve with respect to this "knowledge" as for example in a Bose-Einstein condensate. To investigate whether particles in the fireball behave like the former or the latter or somehow in between correlations are the central object of research. Of course one can exclude the two limiting cases of no and infinite correlation.

In contrast to for example pure $e^+ - e^-$– collisions, where one knows about the initial state and can from this on compute cross sections, in heavy-ion collisions the initial stage and its degrees of freedom are not exactly known. Therefore one can not compute the transition elements connecting initial state and final state. The only statement one can make is about how the particles in the final state are correlated to each other[2]. This is the reason why correlations are investigated intensively.

The single-particle distribution, which can be characterized by the already mentioned anisotropic flow coefficients, is in this context the simplest correlation one can think of. From the experimental side the final state degrees of freedom's correlations are expressed by the Lorentz invariant M-particle-momentum distribution.

$$E_{\vec{p}_1} \cdot ... \cdot E_{\vec{p}_M} \frac{d^{3M}N}{d^3\vec{p}_1 \cdot ... \cdot d^3\vec{p}_M} \tag{4.1.1}$$

This Lorentz invariant observable gives the number of particles in the corresponding momentum space element. Note that for the above formula $M \leq N$ must hold, where N is the total number of particles. Such an observable can be modeled from a mathematical point of view by a M particle probability density distribution.

$$p^{(M)}(\vec{p}_1, ...\vec{p}_M) \tag{4.1.2}$$

[1] Of course the physics of the special relativity sets for this case a causal limit in reality.
[2] ,or to certain symmetry planes, as discussed later.

It gives the probability for a system that there is one particle with momentum $\vec{p}_1 + d\vec{p}$ and one particle with momentum $\vec{p}_2 + d\vec{p}$ and so on. Note that in contrast to the distribution functions f in former chapters – which are normalized to particle number,– the probability distributions p are normalized to 1. Leaving aside problems of normalization in the case of fluctuating particle number, let us turn to the physical content of the probability (4.1.2).

In the case $M = 1$ we saw the usual treatment already in the introduction of this thesis. In this case one deals with a single-particle momentum spectrum. Since for high energetic collisions one mostly detects the mid rapidity region, one can get rid of the η_s-dimension. If one uses in addition the fact that the symmetry of the transverse plane is polar, one can perform a Fourier expansion in the azimuthal angle ϕ_p. This justifies the name of the chapter, since we are just investigating the azimuthal dependence of correlations. While performing the above listed assumptions, for the one particle case we end up with the anisotropic flow coefficients, which we already discussed. This expansion in flow coefficients builds the basis of all statistical descriptions of the fireball expansion. Every further signal develops on the background of this(these) correlation(s) to the symmetry plane(s). Therefore a careful investigation of this observable is essential for making statements about more detailed correlations.

As a quite natural extension of the concept we consider the case $M = 2$. In the case that two particles in the system are completely independent the two-particle distribution function factorizes in the following way.

$$p^{(2)}(\vec{p}_1, \vec{p}_2) = p^{(1)}(\vec{p}_1) \cdot p^{(1)}(\vec{p}_2) \tag{4.1.3}$$

However luckily for all physicists dealing with interactions, this will never be the case in a heavy-ion description, due to the fact that there have to be correlations at play. Potential and important sources of two – or even more – particle correlations that are worth being investigated are listed here.

- **Decays of particles** during the way to the detector in the hadronic phase. Because in a decay the original particle's momentum and energy has to be conserved. For example due to the process $\Delta^{++} \to p + \pi^+$ one should get a correlation signal for pions and protons.

- **Quantum correlations** like Bose enhancement or Fermi suppression for identical particles settled in the same phase space region. Here for example the Bose enhancement is easily measurable in $\pi - \pi$–correlations. A repulsion of protons[3] should be in principle also present, but it is harder to detect such a process due to the next point.

- **Final state particles interacting** via a the strong interaction or via electroweak gauge bosons. A simple example are particles emitted by a β^--decay, which attract each other, whereas final state particles from a β^+-decay are pushed apart, due to their same charge.

- The last source is the **global transverse momentum conservation** of the whole system, which has been analyzed in [62]. In fact all the transverse momenta of the particles have to add up to zero.

[3],since neutrons are harder to detect since they do not carry an electric charge.

All these listed sources are rich of – in principle known – physics. In order to discover "new physics" or anomalous effects, one has to understand first how the above effects are reflected in the correlations. Due to the listed effects in principle the two-particle distribution contains, in addition to expression (4.1.3), a two-particle correlation part

$$p^{(2)}(\vec{p}_1, \vec{p}_2) = p^{(1)}(\vec{p}_1) \cdot p^{(1)}(\vec{p}_2) + p_c^{(2)}(\vec{p}_1, \vec{p}_2) \tag{4.1.4}$$

Of course this concept can be extended to three or more particle correlations, although some of the above listed origins are not able to generate correlations between many particles. For three particles the above expression generalizes to the following sum.

$$\begin{aligned} p^{(3)}(\vec{p}_1, \vec{p}_2, \vec{p}_3) \quad = \quad & p^{(1)}(\vec{p}_1) \cdot p^{(1)}(\vec{p}_2) \cdot p^{(1)}(\vec{p}_3) \\ & + p_c^{(2)}(\vec{p}_1, \vec{p}_2) \cdot p^{(1)}(\vec{p}_3) + p_c^{(2)}(\vec{p}_2, \vec{p}_3) \cdot p^{(1)}(\vec{p}_1) + p_c^{(2)}(\vec{p}_1, \vec{p}_3) \cdot p^{(1)}(\vec{p}_2) \\ & + p_c^{(3)}(\vec{p}_1, \vec{p}_2, \vec{p}_3) \end{aligned} \tag{4.1.5}$$

At this point let us emphasize that the real particle correlations are labeled by the index c. It is important to notice that a three-particle distribution $p^{(3)}$ can also be non vanishing in the case of vanishing three-particle correlations $p_c^{(3)}$, which are also called cumulants . This expression can be visualized in pictures as in the following figure 4.1.

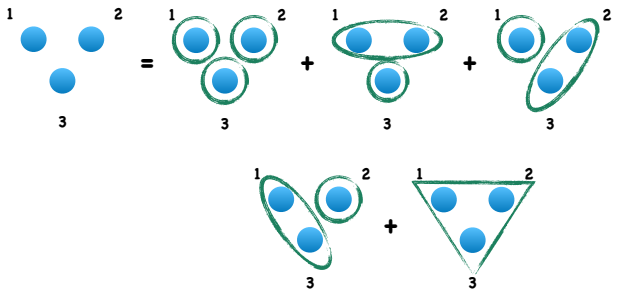

Figure 4.1.: Cartoon of three-particle correlations.

In figure 4.1 the two-particle bubbles, which symbolize $p_c^{(2)}$ could be realized for example by a decay of a particle in two final state particles, whereas the three-particle triangle, which is the last summand, could be realized by a particle decaying in three final state particles.

4.2. On the way to two-particle distributions

After investigating the anisotropic flow and therefore clarifying how particle emission with respect to symmetry planes looks like, one should proceed and generalize the concept in order to investigate two-particle flow coefficients. This generalization is creating an observable which is sensitive to the correlation of two particles $p_c^{(2)}$. The first step in this direction was done in [56].

Such two-particle flow coefficients can in principle be used in order to determine the flow of unstable particles like K_s^0, ϕ or Λ, which decayed outside the fireball but already before reaching the detector. Such a flow analysis can be achieved through a study of the flows of the decay products. After removing all "simple" sources of correlation, the remaining correlation

of the daughter particles has to be due to the flow of the decayed particle. Another possible subject which should be analyzed by two-particle flow coefficients is jet quenching. Since a jet builds up a more or less conical structure as boundary, the fireball's shape can be deposited in jet structures, which are measurable. In order to quantify such deposited shapes due to azimuthal dependent medium pathlength, two-particle correlations are a good observable.

In the following we will construct observables for such two-particle flow studies as was done in [56]. The single-particle probability distribution after Fourier expansion looks like the following.

$$p^{(1)}(\phi_p|\{\psi_n\}) \propto \frac{1}{2\pi}\left[1 + 2\sum_{n=1}^{\infty} v_n(p_t)\cos(n(\phi_p - \psi_n))\right] \tag{4.2.1}$$

In comparison the formula (2.9.8), which is normalized to the particle number, the above expression should be normalized to one. Therefore the expression can be interpreted as a distribution function. Formula (4.2.1) gives the probability of an emitted particle with momentum p_t in direction of ϕ_p under a given set of plane angles ψ_n. Similar to the above, the v_n coefficients can be computed by the integral of $p^{(1)}$ over ϕ_p convoluted with the corresponding $\cos(n\phi_p)$. This single-particle probability distribution $p^{(1)}$ is so to say the background of all further signals, since M-particle distributions will always contain contributions from it[4]. As we already saw, the p_t-dependent flow coefficients v_n are precisely measured and investigated in the context of heavy-ion collisions.

4.3. Controlling the background

Before we calculate the two-particle correlation observables, we should again take a detailed look at formula (4.1.4). Two-particle correlations of physical interest would be hidden in the $p_c^{(2)}$ contribution. But this signal will be on top of the background of the two single-particle contribution's product. In other words one will measure a contribution to the two-particle distribution since a pair of particles is already correlated due to the fact that both are correlated to the symmetry planes $\{\psi_n\}$. Such a correlation has to be taken into account, but is not built up by one of the above mentioned motivations for studying several particle correlations. In order to do so let us first concentrate on the following idealized case, where there are no "true" correlations. In addition we will restrict our investigations to particles in the same rapidity-bin, since we are – as the title of this chapter indicates – interested in azimuthally correlations, but not in longitudinal correlations.

$$p^{(2)}_{trivi}(\vec{p}_a, \vec{p}_b|\{\psi_n\}) = p^{(1)}(\phi_a|\{\psi_n\}) \cdot p^{(1)}(\phi_b|\{\psi_n\}) + \cancel{p^{(2)}_c(\vec{p}_a, \vec{p}_b|\{\psi_n\})} \tag{4.3.1}$$

In this case we are just dealing with the already known. Before we compute the product of the two single-particle probability densities we want to combine the two angles ϕ_p of particle a – denoted by ϕ_a – and ϕ_p of particle b – denoted by ϕ_b – into a pair angle ϕ^{pair} and a relative angle $\Delta\phi$. This transformation and its inverse look as follows.

[4] See for example formula (4.1.4) and (4.1.5).

$$\phi_a, \phi_b \Rightarrow \frac{\phi_a + \phi_b}{2} = \phi^{pair}, \quad \frac{\phi_a - \phi_b}{2} = \Delta\phi \tag{4.3.2}$$

$$\Leftrightarrow \phi_a = \phi^{pair} + \Delta\phi, \ \phi_b = \phi^{pair} - \Delta\phi \tag{4.3.3}$$

Figure (4.2) displays the geometrical meaning of transformation (4.3.2).

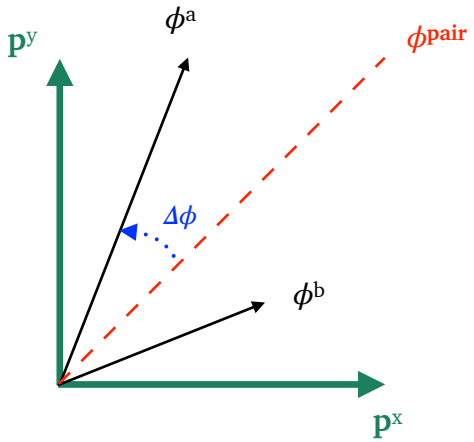

Figure 4.2.: Cartoon of the angles ϕ^{pair} and $\Delta\phi$.

In addition we will employ the usual cos and sin transformations. Please notice that both angles run over an interval from 0 to 2π.

$$\cos(a) + \cos(b) = 2\cos\left(\frac{a+b}{2}\right)\cos\left(\frac{a-b}{2}\right) \tag{4.3.4}$$

$$\cos(a \pm b) = \cos(a)\cos(b) \mp \sin(a)\sin(b) \tag{4.3.5}$$

$$\sin(a \pm b) = \cos(a)\sin(b) \pm \sin(a)\cos(b) \tag{4.3.6}$$

This can be combined to the following transformation.

$$\begin{aligned} \cos(n\phi_a - n\psi_n) &= \cos(n(\phi^{pair} - \psi_n) + n\Delta\phi) \\ &\overset{(4.3.5)}{=} \cos(n(\phi^{pair} - \psi_n))\cos(n\Delta\phi) - \sin(n(\phi^{pair} - \psi_n)\sin(n\Delta\phi) \end{aligned} \tag{4.3.7}$$

The analogous expression for particle b is consequently:

$$\begin{aligned} \cos(n(\phi_b - \psi_n)) &= \cos(n(\phi^{pair} - \psi_n) - n\Delta\phi) \\ &\overset{(4.3.5)}{=} \cos(n(\phi^{pair} - \psi_n))\cos(n\Delta\phi) + \sin(n(\phi^{pair} - \psi_n))\sin(n\Delta\phi) \end{aligned} \tag{4.3.8}$$

Note that we work within the assumption of identical ψ_n for particle a and b, since they are emerging out of the same medium. Since in the following computations we also have to deal with products of the above expressions let us take a look how these can be transformed.

$$
\begin{aligned}
& \cos(n(\phi_a - \psi_n))\cos(m(\phi_b - \psi_m)) \\
= \; & \frac{1}{2}\Big[\cos((n+m)\phi^{pair} - n\psi_n - m\psi_m)\cos((n-m)\Delta\phi) \\
& - \sin((n+m)\phi^{pair} - n\psi_n - m\psi_m)\sin((n-m)\Delta\phi) \\
& + \cos((n-m)\phi^{pair} - n\psi_n + m\psi_m)\cos((n+m)\Delta\phi) \\
& - \sin((n-m)\phi^{pair} - n\psi_n + m\psi_m)\sin((n+m)\Delta\phi)\Big]
\end{aligned} \tag{4.3.9}
$$

With these three transformations (4.3.7), (4.3.8) and (4.3.9), we can now compute expression (4.3.1) while inserting the product of expression (4.2.1). In doing so we neglect all anisotropic single-particle flow coefficients $v_{n>4}$ and the measure of non-centrality v_1. But in principle one could go beyond v_4 at the cost of longer expressions. In addition we label the flow coefficients of particle b with w_n in order to distinguish them from the flow coefficients of particle a. The latter guarantees that we are later able to compute the two-particle density $p^{(2)}_{trivi}(\phi_a, \phi_b)$ for different particles, which may have a different flow pattern due to different masses or charges. However we treat the orientation of the planes $\{\psi_n\}$ to be the same for both particles, since the planes have their origin in the initial state of the collision, which is for one collision of course unique. Performing the product under the above assumptions we end up with the following expression for the two-particle probability distribution.

$$
p^{(2)}_{trivi}(\phi_a, \phi_b|\{\psi_n\}) = p^{(1)}(\phi_a|\{\psi_n\}) \cdot p^{(1)}(\phi_b|\{\psi_n\}) \tag{4.3.10}
$$

$$
\begin{aligned}
p^{(2)}_{trivi}(\phi_a,\phi_b|\{\psi_n\}) &= \tfrac{1}{4\pi^2}\Big[1+2\Big(v_2\cos(2\phi_a-2\psi_2)+v_3\cos(3\phi_a-3\psi_3)+v_4\cos(4\phi_a-4\psi_4)\Big)\Big]\\
&\Big[1+2\Big(w_2\cos(2\phi_b-2\psi_2)+w_3\cos(3\phi_b-3\psi_3)+w_4\cos(4\phi_b-4\psi_4)\Big)\Big]\\
&= \tfrac{1}{4\pi^2}\Big[1+2\Big(v_2\Big\{\cos(2(\phi^{pair}-\psi_2))\cos(2\Delta\phi)-\sin(2(\phi^{pair}-\psi_2))\sin(2\Delta\phi)\Big\}\\
&+w_2\Big\{\cos(2(\phi^{pair}-\psi_2))\cos(2\Delta\phi)+\sin(2(\phi^{pair}-\psi_2))\sin(2\Delta\phi)\Big\}\\
&v_3\Big\{\cos(3(\phi^{pair}-\psi_3))\cos(3\Delta\phi)-\sin(3(\phi^{pair}-\psi_3))\sin(3\Delta\phi)\Big\}\\
&w_3\Big\{\cos(3(\phi^{pair}-\psi_3))\cos(3\Delta\phi)+\sin(3(\phi^{pair}-\psi_3))\sin(3\Delta\phi)\Big\}\\
&v_4\Big\{\cos(4(\phi^{pair}-\psi_4))\cos(4\Delta\phi)-\sin(4(\phi^{pair}-\psi_4))\sin(4\Delta\phi)\Big\}\\
&w_4\Big\{\cos(4(\phi^{pair}-\psi_4))\cos(4\Delta\phi)+\sin(4(\phi^{pair}-\psi_4))\sin(4\Delta\phi)\Big\}\\
&+2v_2w_2\Big\{\cos(4(\phi^{pair}-\psi_2))+\cos(4\Delta\phi)\Big\}+2v_3w_3\Big\{\cos(6(\phi^{pair}-\psi_3))+\cos(6\Delta\phi)\Big\}\\
&+2v_4w_4\Big\{\cos(8(\phi^{pair}-\psi_4))+\cos(8\Delta\phi)\Big\}\\
&+2v_2w_3\Big\{\cos(5\phi^{pair}-2\psi_2-3\psi_3)\cos(\Delta\phi)+\sin(5\phi^{pair}-2\psi_2-3\psi_3)\sin(\Delta\phi)\\
&+\cos(\phi^{pair}+2\psi_2-3\psi_3))\cos(5\Delta\phi)+\sin(\phi^{pair}+2\psi_2-3\psi_3)\sin(5\Delta\phi)\Big\}\\
&+2v_3w_2\Big\{\cos(5\phi^{pair}-3\psi_3-2\psi_2)\cos(\Delta\phi)-\sin(5\phi^{pair}-3\psi_3-2\psi_2)\sin(\Delta\phi)\\
&+\cos(\phi^{pair}-2\psi_2+3\psi_3)\cos(5\Delta\phi)-\sin(\phi^{pair}-3\psi_3+2\psi_2)\sin(5\Delta\phi)\Big\}\\
&+2v_2w_4\Big\{\cos(6\phi^{pair}-2\psi_2-4\psi_4)\cos(2\Delta\phi)+\sin(6\phi^{pair}-2\psi_2-4\psi_4)\sin(2\Delta\phi)\\
&+\cos(2\phi^{pair}+2\psi_2-4\psi_4)\cos(6\Delta\phi)+\sin(2\phi^{pair}+2\psi_2-4\psi_4)\sin(6\Delta\phi)\Big\}\\
&+2v_4w_2\Big\{\cos(6\phi^{pair}-4\psi_4-2\psi_2)\cos(2\Delta\phi)-\sin(6\phi^{pair}-4\psi_4-2\psi_2)\sin(2\Delta\phi)\\
&+\cos(2\phi^{pair}-4\psi_4+2\psi_2)\cos(6\Delta\phi)-\sin(2\phi^{pair}-4\psi_4+2\psi_2)\sin(6\Delta\phi)\Big\}\\
&+2v_3w_4\Big\{\cos(7\phi^{pair}-3\psi_3-4\psi_4)\cos(\Delta\phi)+\sin(7\phi^{pair}-3\psi_3-4\psi_4)\sin(\Delta\phi)\\
&+\cos(\phi^{pair}+3\psi_3-4\psi_4)\cos(7\Delta\phi)+\sin(\phi^{pair}+3\psi_3-4\psi_4)\sin(7\Delta\phi)\Big\}\\
&+2v_4w_3\Big\{\cos(7\phi^{pair}-4\psi_4-3\psi_3)\cos(\Delta\phi)-\sin(7\phi^{pair}-4\psi_4-3\psi_3)\sin(\Delta\phi)\\
&+\cos(\phi^{pair}+3\psi_3-4\psi_4)\cos(7\Delta\phi)-\sin(\phi^{pair}-4\psi_4+3\psi_3)\sin(7\Delta\phi)\Big\}\Big)\Big] \qquad (4.3.11)
\end{aligned}
$$

Please keep in mind that both single-particle flow coefficients v_n, w_n depend on the modulus of their particle momentum, consequently the two-particle probability exhibits this dependence as well. With this expression at hand one can compute flow coefficients just like the way it is done in the single-particle case (2.9.9) via

$$v_{n,c}^{pair}(\Delta\phi, |p_a|, |p_b|) = \frac{\int_0^{2\pi} d\phi^{pair}\ p_{trivi}^{(2)}(\phi^{pair}, \Delta\phi|\{\psi_n\})\cos(n(\phi^{pair} - \psi_n))}{\int_0^{2\pi} d\phi^{pair}\ p_{trivi}^{(2)}(\phi^{pair}, \Delta\phi|\{\psi_n\})} \tag{4.3.12}$$

as well as

$$v_{n,c}^{\Delta\phi}(\phi^{pair}, |p_a|, |p_b|) = \frac{\int_0^{2\pi} d\Delta\phi\ p_{trivi}^{(2)}(\phi^{pair}, \Delta\phi|\{\psi_n\})\cos(n(\Delta\phi))}{\int_0^{2\pi} d\Delta\phi\ p_{trivi}^{(2)}(\phi^{pair}, \Delta\phi|\{\psi_n\})}. \tag{4.3.13}$$

But since there exist $\sin(\phi^{pair})$ and $\sin(\Delta\phi)$ –terms as well in expression (4.3.11), additionally we have to deal with $v_{n,s}$ coefficients, which are defined as follows

$$v_{n,s}^{pair}(\Delta\phi, |p_a|, |p_b|) = \frac{\int_0^{2\pi} d\phi^{pair}\ p_{trivi}^{(2)}(\phi^{pair}, \Delta\phi|\{\psi_n\})\sin(n(\phi^{pair} - \psi_n))}{\int_0^{2\pi} d\phi^{pair}\ p_{trivi}^{(2)}(\phi^{pair}, \Delta\phi|\{\psi_n\})} \tag{4.3.14}$$

and

$$v_{n,s}^{\Delta\phi}(\phi^{pair}, |p_a|, |p_b|) = \frac{\int_0^{2\pi} d\Delta\phi\ p_{trivi}^{(2)}(\phi^{pair}, \Delta\phi|\{\psi_n\})\sin(n(\Delta\phi))}{\int_0^{2\pi} d\Delta\phi\ p_{trivi}^{(2)}(\phi^{pair}, \Delta\phi|\{\psi_n\})} \tag{4.3.15}$$

In the above definitions for the pair-flow coefficients it is governed that they are independent of a reference angle throughout the subtraction of the corresponding ψ_n. This subtraction preserves the invariance of the particle spectrum. For the relative angle this is of course not needed, since an offset of the angle does not contribute in a difference of two angles. Of course one could have started from a two-particle probability distribution $p_{trivi}^{(2)}(\phi^{pair}, \Delta\phi|\{\psi_n\})$ and perform from this on a Fourier expansion in either ϕ^{pair} or $\Delta\phi$, ending up in a series which looks like the following expression.

$$p_{trivi}^{(2)}(\phi^{pair}, \Delta\phi|\{\psi_n\}) \propto \frac{1}{2\pi}\left[1 + 2\sum_{n=1}^{\infty}\left\{v_{n,c}^{pair}(\Delta\phi)\cos(n(\phi^{pair} - \psi_n)) + v_{n,s}^{pair}(\Delta\phi)\sin(n(\phi^{pair} - \psi_n))\right\}\right]$$

or

$$p_{trivi}^{(2)}(\phi^{pair}, \Delta\phi|\{\psi_n\}) \propto \frac{1}{2\pi}\left[1 + 2\sum_{n=1}^{\infty}\left\{v_{n,c}^{\Delta\phi}(\phi^{pair} - \psi_n)\cos(n(\Delta\phi)) + v_{n,s}^{\Delta\phi}(\phi^{pair} - \psi_n)\sin(n(\Delta\phi))\right\}\right]$$

However, with our lengthy computation (4.3.11) we are able to express the "new" two-particle coefficients as a function of the known single-particle coefficients[5]. Computing

[5] At least in the case of no true correlation.

the two-particle flow coefficient, for example for the contribution arising from integrating while weighting with $\cos(4(\phi^{pair} - \psi_4))$ is – after a addition with 0, namely the replacement $4\phi^{pair} \to 4\phi^{pair} - 4\psi_4 + 4\psi_4$ for the corresponding angles in equation (4.3.11) – the next step, we have to work out. While doing so, one ends up with the following contribution for $v_{4,c}^{pair}$

$$v_{4,c}^{pair}(\Delta\phi, |p_a|, |p_b|) \propto \frac{v_4}{2}\cos(4\Delta\phi) + \frac{w_4}{2}\cos(4\Delta\phi) + v_2 w_2 \cos(4(\psi_2 - \psi_4)). \quad (4.3.16)$$

For computing all the $v_{c,s}^{pair}$ and $v_{c,s}^{\Delta\phi}$ coefficients one should use the orthogonality of the sin and cos functions[6] in order to save time.

$$\int_0^{2\pi} d\phi \cos(a\phi)\cos(b\phi) = \int_0^{2\pi} d\phi \sin(a\phi)\sin(b\phi) = \pi\delta_{ab}, \ \int_0^{2\pi} d\phi \cos(a\phi)\sin(b\phi) = 0$$

Another interesting question is of course the co-domain of the two-particle flow coefficients. Since the single-particle coefficients can take values between -1 and 1, the pair flow coefficient can take a value between -1 and 1.

$$v_{n,c/s}^{pair}(\Delta\phi, |p_a|, |p_b|) \in [-1, 1]$$

Another interesting question is about the presence of the sin terms in the Fourier expansion of the pair flow, since they are absent in the single-particle flow expansion. To answer this question figure 4.3 shows for the pair flow what is happening under the transformation $\phi^{pair} \to -\phi^{pair}$. As one can see in definition (4.3.2) this is equivalent to map ϕ_a and ϕ_b to their negative values. This transformation is sketched in figure 4.3, but as one can see the blue indicated angle $\Delta\phi$ is now pointing in the opposite direction (from the long vector to the short one). In order to reestablish a symmetry one needs to transform $\Delta\phi \to -\Delta\phi$ as well. This anti-symmetry is reflected by the emergence of sin terms in the two-particle Fourier expansions.

[6], which one used already in order to perform the Fourier expansion.

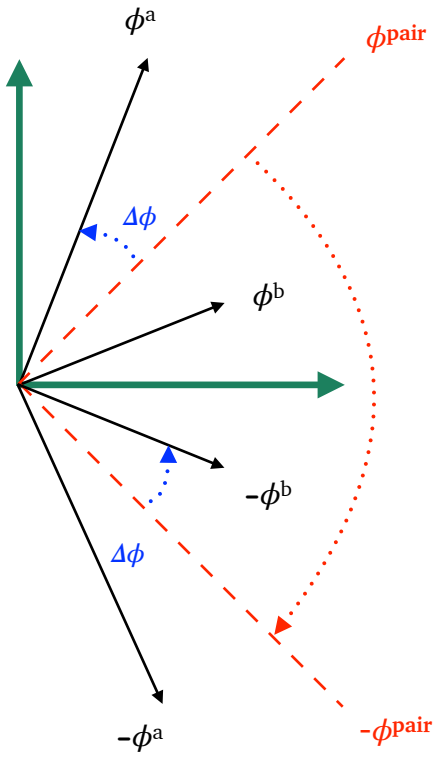

Figure 4.3.: Cartoon illustrating the antisymmetry of the function $p^{(2)}_{trivi}(\phi^{pair}, \Delta\phi|\{\psi_n\})$ with respect to $\phi^{pair} \to -\phi^{pair}$.

Of course one can generalize the contributions for the coefficients $v^{pair}_{c,s}$ and $v^{\Delta\phi}_{c,s}$ to the case, where the expansion of the single-particle spectrum is not stopped after $n = 4$. The most general contribution for the two-particle flow coefficients reads

$$\begin{aligned} v^{pair}_{n,c} \propto & \quad \left(\frac{v_n}{2} + \frac{w_n}{2}\right)\cos(n\Delta\phi) \\ + & \quad \sum_{\substack{i,j \\ i+j=n}} (v_i w_j)\Big[\cos\left((i-j)\Delta\phi\right)\cos(i\psi_i + j\psi_j - (i+j)\psi_{i+j})\Big] \\ + & \quad \sum_{\substack{i,j \\ i-j=n}} (v_i w_j)\Big[\cos\left((i+j)\Delta\phi\right)\cos(i\psi_i - j\psi_j - (i-j)\psi_{i-j})\Big] \end{aligned} \tag{4.3.17}$$

as well as

$$
\begin{aligned}
v_{n,s}^{pair} \propto \quad & \left(-\frac{v_n}{2}+\frac{w_n}{2}\right)\sin(n\Delta\phi) \\
- \quad & \sum_{\substack{i,j \\ i+j=n}} (v_i w_j)\Big[\sin\left((i-j)\Delta\phi\right)\cos(i\psi_i + j\psi_j + (i+j)\psi_{i+j})\Big] \\
- \quad & \sum_{\substack{i,j \\ i-j=n}} (v_i w_j)\Big[\sin\left((i+j)\Delta\phi\right)\cos(i\psi_i - j\psi_j - (i-j)\psi_{i-j})\Big]. \qquad (4.3.18)
\end{aligned}
$$

Equivalently the Fourier expansion in $\Delta\phi$ presented above comes along with the following coefficients in the absence of two-particle cumulants.

$$
\begin{aligned}
v_{n,c}^{\Delta\phi} \propto \quad & \left(\frac{v_n}{2}+\frac{w_n}{2}\right)\cos\left(n(\phi^{pair}-n\psi_n)\right) \\
+ \quad & \sum_{\substack{i,j \\ i+j=n}} (v_i w_j)\Big[\cos\left((i-j)(\phi^{pair}-\psi_{i-j}) + (i-j)\psi_{i-j} + i\psi_i - j\psi_j\right)\Big] \\
+ \quad & \sum_{\substack{i,j \\ i-j=n}} (v_i w_j)\Big[\cos\left((i+j)(\phi^{pair}-\psi_{i+j}) + (i+j)\psi_{i+j} - i\psi_i - j\psi_j\right)\Big] \qquad (4.3.19)
\end{aligned}
$$

and for the sin contributions:

$$
\begin{aligned}
v_{n,s}^{\Delta\phi} \propto \quad & \left(-\frac{v_n}{2}+\frac{w_n}{2}\right)\sin\left(n(\phi^{pair}-\psi_n)\right) \\
- \quad & \sum_{\substack{i,j \\ i+j=n}} (v_i w_j)\Big[\sin\left((i-j)(\phi^{pair}-\psi_{i-j}) + (i-j)\psi_{i-j} - i\psi_i + j\psi_j\right)\Big] \\
- \quad & \sum_{\substack{i,j \\ i-j=n}} (v_i w_j)\Big[\sin\left((i+j)(\phi^{pair}-\psi_{i+j}) + (i+j)\psi_{i+j} - i\psi_i - j\psi_j\right)\Big] \qquad (4.3.20)
\end{aligned}
$$

The above listed n-th order two-particle flow coefficients (4.3.17), (4.3.18), (4.3.19) and (4.3.20) are observables, which can be measured from experimental data as well. But the expressions on the right hand side are just displaying the background built up from the single-particle flow.

Since we know how to compute this background of the two-particle flow coefficients, that is build up from the single-particle flow coefficients, we should be able to compare experimental measured two-particle flow coefficients $v_{n,c/s}^{pair}(\Delta\phi, |p_a|, |p_b|)$ and $v_{n,c/s}^{\Delta\phi}(\phi^{pair}, |p_a|, |p_b|)$ with the above computed ones. In principle a comparison of the measured and the computed ones should give rise to the two-particle cumulants. Figure 4.4 displays this idea of sieving for two-particle cumulants in a sketch.

Figure 4.4.: Cartoon illustrating the subtraction of the computed background from the measurement in order to gain two-particle cumulants.

However the comparison to the experiment comes along with a problem. Up to here we dealt so to say in a 'theorists dream'. Because both, all flow coefficients v_n from particle a and w_n from particle b and the orientation of the symmetry planes ψ_n were just variables or parameters, whose influence on the two-particle observables we investigated. But in the experiment these v_n's, w_n's and ψ_n's are distributed with a certain probability distribution. Which means that the measured values for the flow coefficients fluctuate although one selects similar collision events – for example through a sorting of the collisions via their number of produced particles or centrality of the collision. The fluctuations of the flow coefficient v_2 are measured and can be found in [63].

Therefore we first have to have these fluctuations under control in order to be able to make a reliable statement about two-particle cumulants and the physics hidden in them.

For the fluctuations of the symmetry planes we can assume the following. The different symmetry planes are in general equally distributed. However in one event there is a possibility that for example the planes ψ_2 and ψ_4 are correlated[7]. But we do not expect a correlation between ψ_2 and ψ_3. Investigating these correlations would be an interesting subject for the future, but in this computation we do not deal with them.

4.4. Fluctuations of $\{v_n\}$

4.4.1. Physical origin of $\{v_n\}$ fluctuations

Figure 4.5 illustrates the physical mechanism thought to be the main origin of the v_n's fluctuations. In the heavy-ion collision research, events are classified by their impact parameter, which is experimantally not adjustable. In the upper half of figure 4.5 two such events with the same impact parameter are sketched. Nonetheless, due to the fact that the nuclei are built up by nucleons distributed in average by a certain distribution function, the effective overlap region of the two nuclei is lumpy. The blue dots represent places where a nucleon-nucleon collision took place in this specific event. As a consequence the overlap region's shape differs from event to event, as it is shown in the sketch. In theoretical approaches these initial stages can be modeled by different models, like T$_R$ENTo [64] or Monte Carlo Glauber [65, 66]. The overlap region, which lies in the position space, can be characterized by eccentricities ϵ_n and symmetry plane vectors ψ_n. As it is indicated in figure 4.5, both the amplitude of the anisotropy, basically the size of ϵ_n, and the direction of the symmetry plane ψ_n will fluctuate event-by-event. The fluctuation in the symmetry plane angle is easy to see, the fluctuation in the eccentricity ϵ_2 is reflected in the fact that the left event has a more elliptic shape, than the plane sketched on the right side. In other words for figure 4.5 one would find $\epsilon_2 > \epsilon_2'$.

If one elaborates the initial energy density[8] $\rho(r, \phi)$ arising from nucleon-nucleon collisions,

[7] This is due to the fact that it seem "easier" to built up a quadrangular structure, when there is already an ellipsis.

[8] of course in the mid rapidity region

in a coordinate system whose origin is setteled at the center of energy, one can compute the eccentricities[9] in the following manner [2] for $n \geq 2$.

$$\epsilon_n e^{in\psi_n} := -\frac{\int \rho(r,\phi) r^{n+1} e^{i\ n\phi} dr\ d\phi}{\int \rho(r,\phi) r^{n+1} dr\ d\phi} \tag{4.4.1}$$

A very crucial point for later is the fact, that the eccentricities (4.4.1) are per definition all lying in the interval between $0 \leqslant \epsilon_n \leqslant 1$. Usually the eccentricity $\epsilon_n e^{in\psi_n}$ can be decomposed in the Cartesian contributions.

$$\epsilon_n e^{in\psi_n} = \epsilon_x + i\epsilon_y$$

Assuming that these anisotropies are translated via a (deterministic)[10] hydrodynamical era in a linear way, as it was justified by computations presented in [67] for the case of $n = 2, 3$, we can model the flow coefficients v_n as the linear response to the initial eccentricities ϵ_n. Further in the above publication they found that this linearity holds even for $n = 4$, which is as the authors say "surprising".

$$v_n = \kappa_n \epsilon_n \tag{4.4.2}$$

In equation (4.4.2) κ_n is the linear response coefficient, which depends on the order n. As a matter of fact the anisotropic flow coefficients v_n have to fluctuate in the case the eccentricities ϵ_n fluctuate event by event. Please note that the statement of linear response for ϵ_2 and ϵ_3 holds for kinetic transport as well as the reader can see in [26].

The absolute value of the coefficient κ_n has to be extracted from hydro (or transport) - studies.

Note that the linear response assumption is limiting the range of applicability, since for $n > 3$ the v_n coefficients get multilinear contributions from products of ϵ_m as well, i.e.

$$v_4 = \kappa_4 \epsilon_4 + \kappa_{4,22} \epsilon_2^2 \tag{4.4.3}$$

In this regime the response is neither linear nor completely due to one eccentricity. However the higher order factors $\kappa_{n,ji}$ are measured and can be found in [68][11].

[9] Please note that we are refering to eccentricities for all n, although the name "eccentricity" refers mathematical only to ϵ_2, whereas ϵ_3 is the triangularity and so on.

[10] Deterministic is stressed, since we assume no further sources of fluctuations are at play during the transport regime.

[11] Be aware that in the reference they use a different notation $\kappa_{n,ii} \to \chi_{n,ii}$.

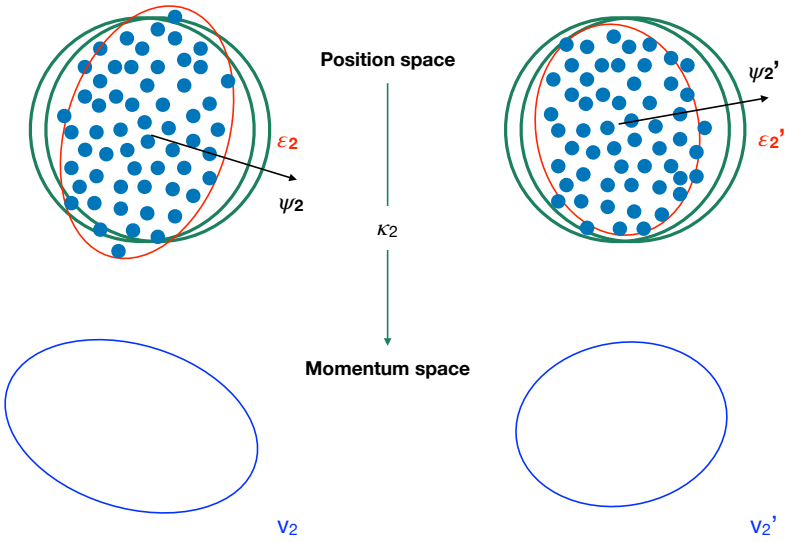

Figure 4.5.: Cartoon illustrating the origin of the fluctuations of v_2.

4.4.2. Linearization of $\{v_n\}$ fluctuations

An often chosen – and rather simple – way to investigate the effect of fluctuations is to investigate the impact of a linear fluctuation. A proper ansatz for such a setup is the following:

$$v_n \to v_n + \delta v_n \tag{4.4.4}$$

Here δv_n is the linear fluctuation of the single-particle flow coefficient. In order to build up a consistent formalism these fluctuations have to be small with respect to the 'mean value' v_n. If one inserts the above ansatz into the expressions for the pair flow coefficients $v^{pair}_{n,c/s}$ or $v^{\Delta\phi}_{n,c/s}$ and linearizes these expressions with respect to the small δv_n, one gets the single-particle flow coefficient fluctuation's impact on the two-particle flow coefficients. For example for $v^{pair}_{4,c}$ this looks as follows.

$$v^{pair}_{4,c}(\Delta\phi|\{\psi_n\}) \propto \left(\frac{v_4+\delta v_4}{2} + \frac{w_4+\delta w_4}{2}\right)\cos(4\Delta\phi) + [\delta v_2\ w_2 + v_2\ \delta w_2]\cos(4(\psi_2-\psi_4))$$

After subtracting equation (4.3.16) from equation (4.4.5), one finds the fluctuation $\delta v^{pair}_{4,c}$. In principle with this mechanism we are able to describe small fluctuations. However demanding δv_n to be small comes along with some problems. First the flow coefficients are by themselves between 0 and 1 so they are on the one hand in some sense already small and on the other hand the fluctuations are limited "at the edges" in order to guarantee the set of realization for v_n.

This problem becomes even bigger if one is interested in the most central collisions, where the eccentricities[12] are only built up due to fluctuations and the mean value for v_n is already

[12] and therefore the flow coefficients.

very small. In this scenario where the mean value of v_n is only fluctuation driven the above mentioned ansatz including a linearization is an ill defined tool.

But in the case of a larger expectation value for v_n this ansatz can be useful within a limited scope of application. A much more general tool to describe and model the fluctuations of v_n will be presented in the following section.

4.4.3. Power law like fluctuations

In order to describe the fluctuations of the v_n in a better way than we did in section 4.4.2, we follow the ideas and concepts presented in [69] and [70]. They studied basically how initial stage eccentricities are fluctuating over many events and how these fluctuations are transformed into fluctuations of the anisotropic flow coefficients in which we are interested. In detail they elaborate two ways to model the fluctuations of the eccentricities. The more intuitive way is built upon the assumption, that the vector $\epsilon_n e^{in\psi_n}$ is fluctuating in magnitude and direction. They parametrize these fluctuations in the two components of the eccentricity vector by a two dimensional Gaussian distribution function. After integrating out the angle one ends up with a one dimensional Bessel-Gaussian distribution $p(\epsilon_n)$, which has the following form[13].

$$p(\epsilon_n) = \frac{\epsilon_n}{\sigma} I_0\left(\frac{\bar{\epsilon}_0 \epsilon_n}{\sigma^2}\right) e^{-\frac{\bar{\epsilon}_0^2+\epsilon_n^2}{2\sigma^2}} \tag{4.4.5}$$

In the above formula $\bar{\epsilon}_0$ is denoting the mean value of the eccentricity ϵ_n and I_0 denotes the modified Bessel function of first kind.

$$I_\alpha(z) = \frac{1}{\pi}\left(\int_0^\pi d\theta \cos(\alpha\theta) e^{x\cos(\theta)}\right) - \frac{\sin(\alpha\pi)}{\pi}\int_0^\infty dt\ e^{-x\cosh(t)-\alpha t}$$

The σ in equation (4.4.5) denotes the standard deviation, which sets the scale for the fluctuations of the ϵ_n. At this point the authors stress that the parameter set ϵ_0 and σ has a dependence on the harmonic n. This distribution shows a good behavior, since it is vanishing for $\epsilon_n = 0$ This assures that the distribution gives no negative ϵ_n contributions, which is important since ϵ_n has to be greater than 0, as above mentioned.

In the limiting case where the mean eccentricity is vanishing ($\bar{\epsilon}_0 = 0$) the distribution (4.4.5) is simplified to a (originally two dimensional) Gaussian distribution. In this scenario the distribution function simplifies to the following form.

$$p(\epsilon_n|\bar{\epsilon}_0 = 0) = \frac{\epsilon_n}{\sigma^2} e^{-\frac{\epsilon_n^2}{2\sigma^2}} \tag{4.4.6}$$

A crucial remark regarding formulas (4.4.5) and (4.4.6) is that they both take into account that the set of realizations of ϵ_n has to be greater than zero, but they do not take into account that ϵ_n is also bounded from above, since the eccentricities have to be smaller than one. In order to incorporate this fact properly, we need a distribution which in addition has the following feature $p(\epsilon_n = 1) = 0$.

A second functional form for the distribution function modelling the fluctuations of the

[13] One can find the computation in [55].

eccentricities was elaborated by the authors in [69]. Namely this is the elliptic power distribution, which reads as follows.

$$p(\epsilon_n) = \frac{2\alpha\epsilon_n}{\pi}\left(1-\bar{\epsilon}_0^2\right)^{\alpha+\frac{1}{2}} \int_0^{\pi} \frac{\left(1-\epsilon_n^2\right)^{\alpha-1}}{\left(1-\bar{\epsilon}_0\epsilon_n\cos(\phi)\right)^{2\alpha+1}} d\phi \tag{4.4.7}$$

This expression simplifies in the case of a vanishing mean eccentricity $\bar{\epsilon}_0$ to the following expression.

$$p(\epsilon_n) = 2\ \alpha\ \epsilon_n \left(1-\epsilon_n^2\right)^{\alpha-1} \tag{4.4.8}$$

This distribution function has the advantage that its support lies between 0 and 1. In addition the distribution is already normalized with respect to this interval. After taking a look at equation (4.4.8) one can realize that this distribution function depends only on the parameter α, which has of course a dependence on n as well. In principle this parameter can be fitted by analyzing histograms of eccentricity ϵ_n generated by a Monte Carlo Glauber simulation.

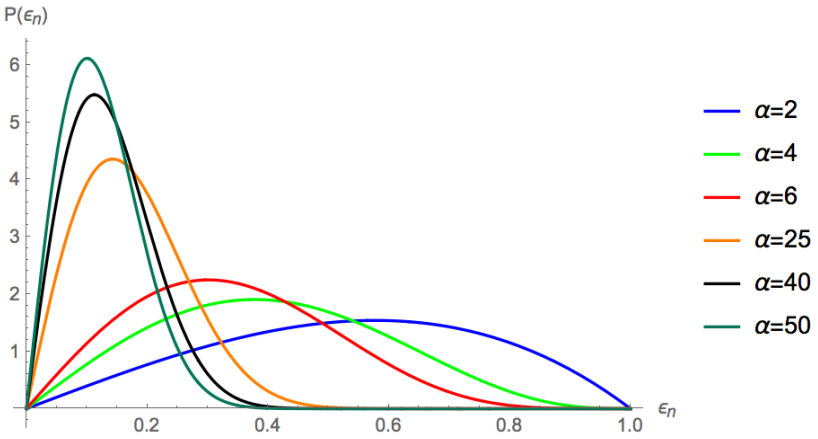

Figure 4.6.: Plot of the power law distribution for different coefficients α.

Figure 4.6 is a plot of the power law distribution for different coefficients α. As one can see the distribution is broad for small values of α. As one increases the parameter α, the distribution becomes sharper and closer to zero. As already mentioned the distribution approaches zero at both ends of the eccentricity's interval.

If we expand the power law distribution (4.4.8) in the (per definition) small parameter ϵ_n^2 and assume in addition that $\alpha \gg 1$ we can recover the Gaussian distribution.

$$
\begin{aligned}
p(\epsilon_n) &= 2\ \alpha\ \epsilon_n \left(1-\epsilon_n^2\right)^{\alpha-1} \\
\Leftrightarrow \frac{p(\epsilon_n)}{2\ \alpha\ \epsilon_n} &= \left(1-\epsilon_n^2\right)^{\alpha-1} \\
&= 1+(1-\alpha)\epsilon_n^2+\frac{1}{2}(\alpha-2)(\alpha-1)\epsilon_n^4-\frac{1}{6}(\alpha-3)(\alpha-2)(\alpha-1)\epsilon_n^6+\mathcal{O}(\epsilon_n^8) \\
&\overset{\alpha>>1}{\approx} 1-\alpha\epsilon_n^2+\frac{\alpha^2}{2}\epsilon_n^4-\frac{\alpha^3}{6}\epsilon_n^6 \\
&\approx e^{-\alpha\epsilon_n^2}
\end{aligned}
\tag{4.4.9}
$$

While comparing the above equation (4.4.9) with distribution (4.4.6) one can identify the two parameters.

$$
\alpha \approx \frac{1}{2\sigma^2} \tag{4.4.10}
$$

So in the case of vanishing mean value ϵ_0 and high α both distributions (4.4.6) and (4.4.8) are converging against each other. As an example figure 4.7 shows the two distribution functions for $\alpha = 30$.

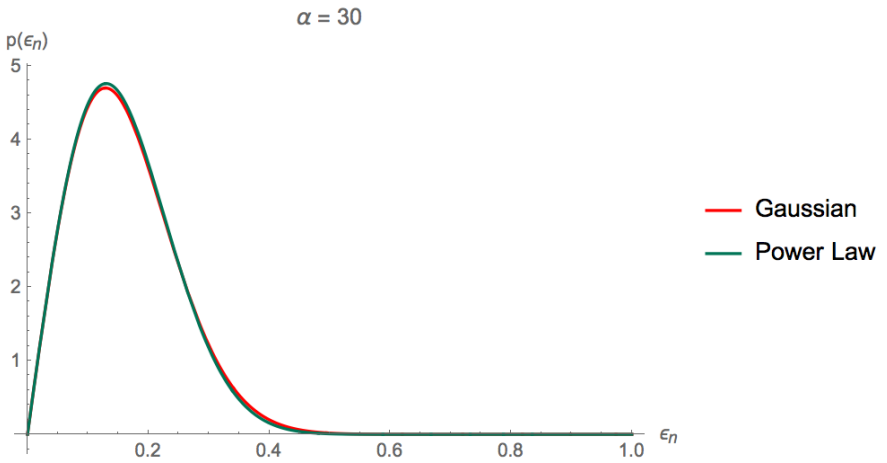

Figure 4.7.: Plot of the Gaussian distribution (red) and the power law distribution (green).

One can easily see that already for such a value of α the two distributions are nearly equivalent. Only after a second look one can identify the power law distribution to be a little bit sharper.

Figure 4.8 shows the difference between the Gaussian distribution and the power law distribution for various values of α.

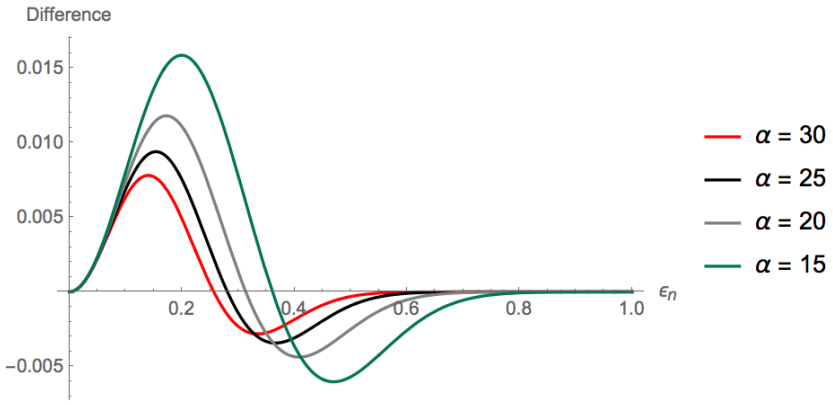

Figure 4.8.: Plot of the difference of power law distribution minus the Gaussian distribution for various α.

As one can see the differences grow with decreasing α, which is clear, since the approximation (4.4.9) works better for high values of α. However for the shown values the difference is small compared to the absolute values of the distribution functions.

If we are now assuming the v_n's to emerge as linear response from the eccentricities like it is written in formula (4.4.2), we are able to parametrize the fluctuations of the flow coefficients, while maintaining the fitted parameter α in the case of power law parametrization or σ in the case of Gaussian distribution.

The fluctuations of $\epsilon_n = {}^{v_n}/_{\kappa_n}$ are transferred to fluctuations in v_n, via the following equation.

$$p(v_n) = \frac{1}{\kappa_n} p\left(\frac{v_n}{\kappa_n}\right) \tag{4.4.11}$$

Here the above already mentioned problem of validity arises, since for higher harmonics one needs to take more care, due to multilinear and additive contributions of eccentricities. However for the case of $n = 2, 3$ and following [67] even $n = 4$ the above model is valid.

4.4.4. Extraction of fluctuations from a Glauber Monte Carlo

As already mentioned above one can extract the fluctuations of the eccentricities ϵ_n from an initial stage model. We did this via the public available program "TGlauberMC"[14] version 3.1. A longer review on the ideas behind this initial stage modelling can be found in [65]. The most recent report is [66]. A detailed description how the values for the ϵ_n where extracted from the simulations can be found in the Master thesis of Hendrik Roch [71].

Basically he simulated 10000 events per impact parameter. In this context an event is a nucleus-nucleus collision. After a conversion process of local number of collisions into local energy density, he computed for every event the different eccentricities from ϵ_2 up to ϵ_6 in a center of mass frame. Figure 4.9 shows a plot of the elaborated energy density distribution.

In order to systematically investigate the simulations for convergence of the averaged value of ϵ_n, he repeated this procedure. Afterwards he compiled from the generated eccentricity data histograms for the different impact parameters.

[14] https://tglaubermc.hepforge.org

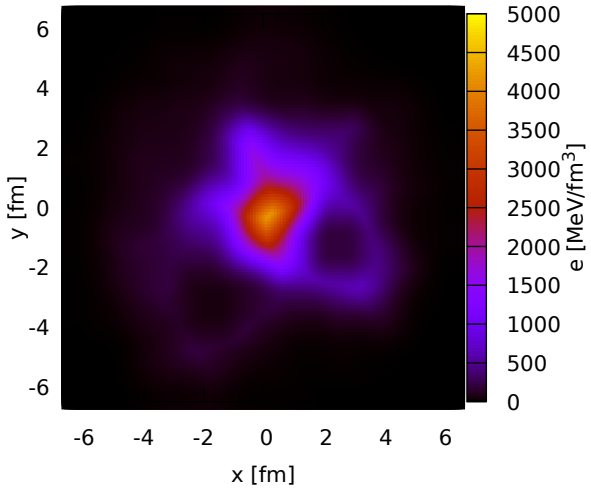

Figure 4.9.: Plot of the energy density distribution of one simulated event.

Figure 4.10 shows as an example such a generated histogram for ϵ_2 and impact parameter $b = 0$. The mean value extracted from this histogram – indicated by the green bar – is $\langle \epsilon_2 \rangle = 0.198$.

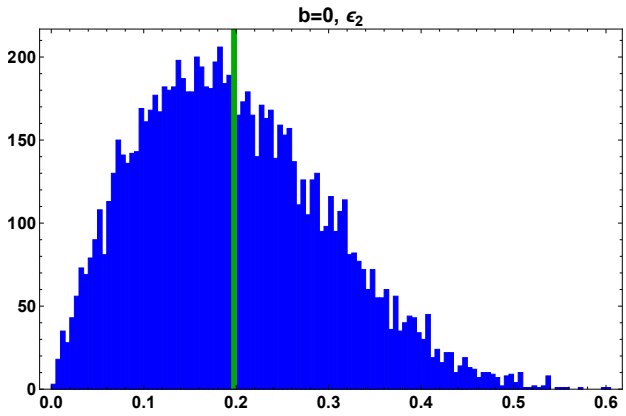

Figure 4.10.: Glauber Monte Carlo generated histogram of ϵ_2 for $b = 0$ with 10000 events.

As a next step he fitted the power law distribution (4.4.8) to the elaborated histograms and extracted the values for the fit parameter α. Such a fit for the above shown histogram is shown in figure 4.11.

As one can see the fit matches the generated data very well. Table 4.1 is the outcome of his work. It shows the gathered values for α emerging for the eccentricities ϵ_2 up to ϵ_6 at eight different impact parameter values. Note that the error intervals are estimated through the fit procedure.

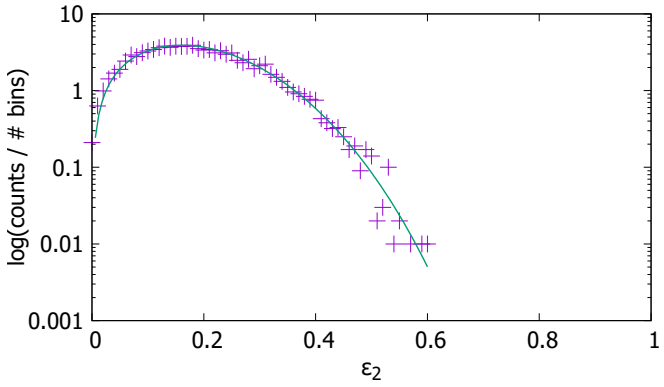

Figure 4.11.: Fit of the histogram figure 4.10 with the power law distribution function.

b	α for ε_2
0	19.98 ± 0.20
3	18.48 ± 0.15
6	13.01 ± 0.12
8	8.30 ± 0.08
9	6.09 ± 0.08
11	2.71 ± 0.04
12	1.83 ± 0.04
14	1.84 ± 0.10

b	α for ε_3
0	24.95 ± 0.20
3	22.77 ± 0.23
6	16.36 ± 0.15
8	10.29 ± 0.10
9	7.85 ± 0.08
11	4.37 ± 0.05
12	3.33 ± 0.04
14	2.89 ± 0.29

b	α for ε_4
0	26.00 ± 0.22
3	23.21 ± 0.16
6	14.86 ± 0.13
8	8.80 ± 0.09
9	6.53 ± 0.07
11	3.20 ± 0.04
12	2.19 ± 0.03
14	1.89 ± 0.10

b	α for ε_5
0	27.70 ± 0.24
3	22.76 ± 0.21
6	13.36 ± 0.11
8	7.66 ± 0.09
9	5.67 ± 0.07
11	3.03 ± 0.04
12	2.28 ± 0.03
14	2.16 ± 0.18

b	α for ε_6
0	28.51 ± 0.22
3	22.66 ± 0.24
6	11.82 ± 0.12
8	6.85 ± 0.08
9	5.12 ± 0.06
11	2.84 ± 0.03
12	2.20 ± 0.04
14	2.48 ± 0.15

Table 4.1.: Tables with the values of α for the different eccentricities and impact parameters.

Investigating the entries of table 4.1 one sees that with increasing impact parameter b the value for α decreases. This corresponds to a wider distribution function. So the fluctuations of the corresponding eccentricity are bigger. The fitted value for α seems to have an "offset"-value around $\alpha \approx 2$. This value corresponds to the blue distribution function plotted in figure 4.6. Another result of these Glauber studies is that the distribution functions for higher eccentricities ϵ_n are sharper, since the values for α are bigger.

4.5. How do the fluctuations of v_n influence fluctuations of $v^{pair}_{n,c/s}$

Now the important question is how the above discussed fluctuations of v_n are transformed into fluctuations of the two-particle flow coefficients $v^{pair}_{n,c/s}$ and $v^{\Delta\phi}_{n,c/s}$. To answer this question

here we present computations for the case of $v^{pair}_{3,c}$ and $v^{pair}_{2,c}$.

For the case of $n = 3$ the distribution $P(v^{pair}_{3,c})$, which describes the fluctuations of the pair flow coefficient, looks as follows.

$$P(v^{pair}_{3,c}) = \int_0^1 dv_3 \int_0^1 dw_3 P(v_3)P(w_3)\delta\left(v^{pair}_{3,c} - \left(\frac{v_3}{2} + \frac{w_3}{2}\right)\cos(3\Delta\phi)\right) \quad (4.5.1)$$

Basically the probability distribution of the two-particle pair flow consists of the product of the two single-particle distributions integrated over the whole support times a delta distribution, which guarantees the functional dependence of the single – and the two-particle flow coefficients.

If we now insert the distribution function for the single-particle fluctuations, which we discussed in the previous sections one can get access to the probability density of the pair flow coefficients. In the case of the Bessel-Gaussian distribution for $P(v_n)$, which was defined in equation (4.4.6) we get the following plot for the probability distribution of $P(v^{pair}_{3,c})$:

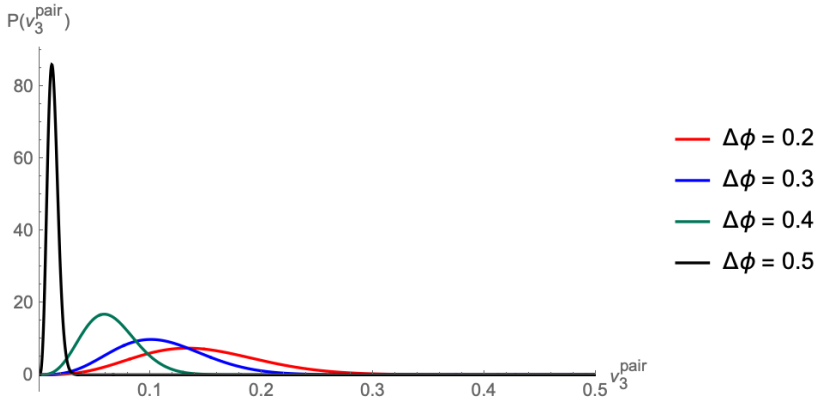

(a)

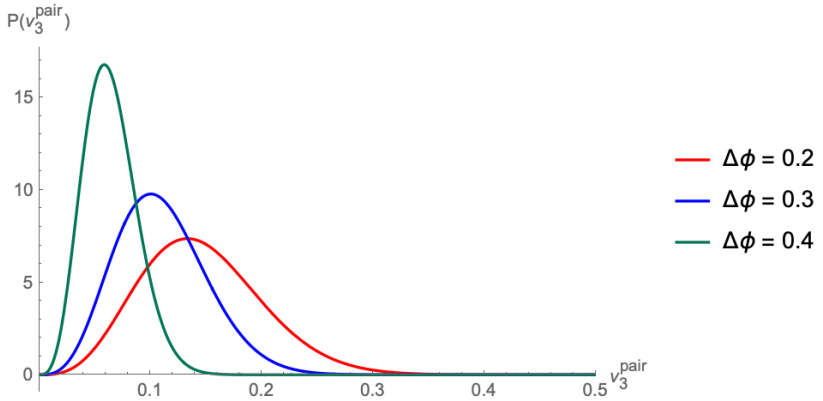

(b)

Figure 4.12.: Plots of the distribution $P(v^{pair}_{3,c})$ over $v^{pair}_{3,c}$ in the case of Bessel-Gaussian single-particle fluctuations for different values of the relative angle $\Delta\phi$.

As one can see in figure 4.12 the fluctuations of the pair flow coefficient $v^{pair}_{3,c}$ gets smaller for increasing relative angle $\Delta\phi$. However even for small relative angles the fluctuations of

the pair flow are in some sense under control. Note that the horizontal axis is plotted only up to 0.5. For the width σ we chose, according to table 4.1 $\sigma \approx 0.2$, which is the extracted value for most central collisions. Of course one could do the same analysis for various impact parameters. Since the value for the coefficient α decreases with increasing impact parameter b, the distributions become wider in this case. But in addition the power law distribution also differs more from the Bessel-Gaussian distribution. Therefore it is more suitable to work only with the power law distribution for small values of α , since the Bessel-Gaussian distribution differs too much, as we saw in figure 4.8.

The distribution function $P(v_{2,c}^{pair})$ for the case of the pair flow coefficient $v_{2,c}^{pair}$ looks like the following.

$$P(v_{2,c}^{pair}) = \int_0^1 dv_2 \int_0^1 dw_2 P(v_2)P(w_2)\delta\left(v_{2,c}^{pair} - \left(\frac{v_2}{2} + \frac{w_2}{2}\right)\cos(2\Delta\phi)\right) \quad (4.5.2)$$

With using formula (4.5.2) we elaborated the following figure 4.13.

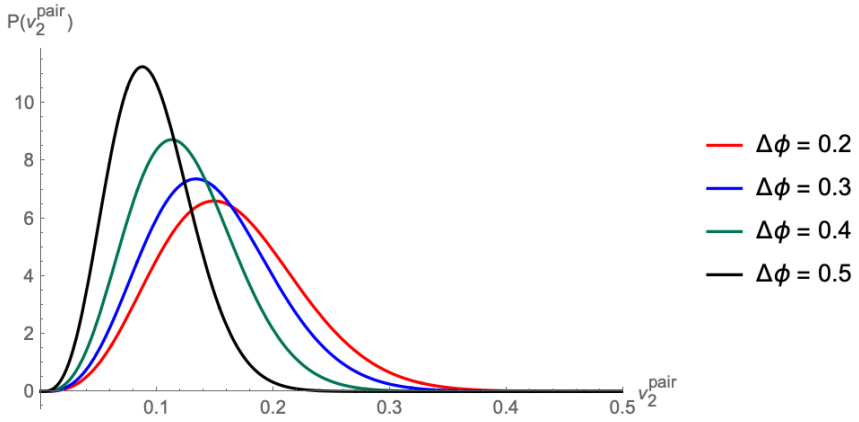

Figure 4.13.: Plot of the distribution $P(v_{2,c}^{pair})$ over $v_{2,c}^{pair}$ in the case of Gaussian single-particle fluctuations for different values of the relative angle $\Delta\phi$.

Here we used according to table 4.1 for the width $\sigma \approx 0.22$, which results in a little bit broader distribution $P(v_{2,c}^{pair})$ compared to the case of $P(v_{3,c}^{pair})$. In addition the strong dependence on the relative angle $\Delta\phi$ is less pronounced, since the peak of the distribution does not vary that much while varying the angle.

In order to investigate the higher pair flow coefficients $P(v_{n>3,c}^{pair})$, we would have to diminish our linear response ansatz 4.4.2, as already mentioned. Compared to formulas (4.5.1) and (4.5.2), this would come along with more integrals to solve, since more eccentricities are feeding in the higher flow coefficients. Besides the more complicated integrals the procedure is the same.

4.6. Summary and Outlook

In chapter 4 we introduced a way to generalize the concept of the single-particle azimuthal flow coefficients in order to gain information about two-particle cumulants. We started with elaborating the observables $v_{n,c,s}^{pair}$ as well as $v_{n,c,s}^{\Delta\phi}$. These observables are indicating two-

particle correlations and are therefore a powerful tool to investigate heavy-ion collision data in the future. In general we want to investigate the effect of the above listed phenomena, like decays of hadrons, on these observables. Later we also presented how the known single-particle correlations to the symmetry plane angles ψ_n are reflected in the pair flow coefficients. This is important in order to be able to subtract these already known correlations, since they do not carry new information. Afterwards we discussed the fact that measurements of these observables is effected by fluctuations in the initial stage of the experiment. This is crucial, since we do not want to misinterpret the effect of fluctuations as a correlation. Therefore we elaborated models, which incorporate the effect of the initial state fluctuations on the fluctuations of $v_{n,c,s}^{pair}$ and $v_{n,c,s}^{\Delta\phi}$. One of these models was the linear fluctuation model, which is limited in the application range. The much more suitable model is the power law model, which we elaborated in detail. Here we needed in addition external parameters α, which we extracted from Glauber-Monte-Carlo studies. With the power law model at hand we presented two cases how the effect of single-particle flow coefficient fluctuations drives fluctuations of the two-particle flow coefficients.

At this point one can now test the model with real measured data in order to measure two-particle flow in the above mentioned scenarios. But of course the model by itself can be improved further. The next step would be to elaborate the effects of fluctuations for the pair flow coefficients for $n \geq 4$. In the case of higher n the functional dependence of the pair flow coefficients comes along with several additional integrals.

Another important step is to compute the theoretical expectation on the values of the pair flow coefficients, arising from the different listed physical origins of correlations.

A

Acknowledgments

First of all I want to thank professor Nicolas Borghini for being a real "Doktorvater" and for guiding me through the fascinating aspects of the ultra relativistic heavy-ion research, starting from the Bachelor up to this thesis. I want to thank him for all the time he invested in lectures, seminars and office discussions in order to give me the opportunity to start doing research. In addition I want to thank Nicolas for sending me to several conferences all over the world, while allowing me to present our recent research status.

I want to thank Nina, Hendrik and Marc for proofreading of this thesis and for discussing about different research aspects. Further I want to thank all the current – and also already gone – members of the heavy-ion research group in Bielefeld for all discussions that took place.

In addition I want to thank all office mates, as well as several other floor neighbors for the wonderful atmosphere during my time in D6-146.

Further I want to thank all the professors and tutors, who taught physics in such a way that I was fascinated and motivated.

I want to thank professor Dominik Schwarz for being the second referee.

Further I want to thank all the CRC-TR211-members. Although the traveling time was long, there were enlightening talks and discussions.

Certainly I want to thank Nina again, but this time for all the out of university aspects and for supporting me throughout the thrilling Bielefeld time.

In addition I want to thank my family for their support during my whole education up to here.

Last I wish all the best for all D6/E6-people in their future endeavors, it was a pleasure to be a part of you.

Declaration of authorship

Hereby I declare that I have written this present thesis on my own. The thesis has not been previously submitted to any examination office. Only the sources and literature indicated have been used.

Bielefeld, November 15, 2018
place, date

Steffen Feld

List of Figures

Bibliography

[1] Wojciech Florkowski. *Phenomenology of ultra-relativistic heavy ion collisions*. World Scientific, Hackensack, NJ [u.a.], 2010.

[2] Asis Kumar Chaudhuri. *A short course on relativistic heavy ion collisions*. Expanding physics. IOP Publ., Bristol, 2014.

[3] Carlos A. Salgado. Lectures on high-energy heavy-ion collisions at the LHC. In *2008 European School of High-Energy Physics, Herbeumont-sur-Semois, Belgium, 8-21 June 2008*, pages 239–280, 2009.

[4] M. A. Lisa. Size matters: Spacetime geometry in subatomic collisions, 2004.

[5] Wit Busza, Krishna Rajagopal, and Wilke van der Schee. Heavy Ion Collisions: The Big Picture, and the Big Questions. 2018.

[6] M. Tanabashi et al. Review of Particle Physics. *Phys. Rev.*, D98(3):030001, 2018.

[7] Patrick Steinbrecher. The QCD crossover at zero and non-zero baryon densities from Lattice QCD. 2018.

[8] Paul Romatschke. Do nuclear collisions create a locally equilibrated quarkgluon plasma? *Eur. Phys. J.*, C77(1):21, 2017.

[9] J. D. Bjorken. Highly Relativistic Nucleus-Nucleus Collisions: The Central Rapidity Region. *Phys. Rev.*, D27:140–151, 1983.

[10] Christoph Blume. Lecture at International school on Quark-Gluon Plasma and Heavy Ion Collisions: past, present future, 2011.

[11] Nicolas Borghini, Steffen Feld, and Christian Lang. Kinetic freeze-out from an anisotropic fluid in high-energy heavy-ion collisions: particle spectra, Hanbury Brown-Twiss radii, and anisotropic flow. *Eur. Phys. J.*, C75(6):275, 2015.

[12] Mubarak Alqahtani, Mohammad Nopoush, and Michael Strickland. Relativistic anisotropic hydrodynamics. *Prog. Part. Nucl. Phys.*, 101:204–248, 2018.

[13] Michael Strickland. Anisotropic Hydrodynamics: Three lectures. *Acta Phys. Polon.*, B45(12):2355–2394, 2014.

[14] Wojciech Florkowski and Radoslaw Ryblewski. Highly-anisotropic and strongly-dissipative hydrodynamics for early stages of relativistic heavy-ion collisions. *Phys. Rev.*, C83:034907, 2011.

[15] Mubarak Alqahtani, Mohammad Nopoush, Radoslaw Ryblewski, and Michael Strickland. Anisotropic hydrodynamic modeling of 2.76 TeV Pb-Pb collisions. *Phys. Rev.*, C96(4):044910, 2017.

[16] Fred Cooper and Graham Frye. Comment on the Single Particle Distribution in the Hydrodynamic and Statistical Thermodynamic Models of Multiparticle Production. *Phys. Rev.*, D10:186, 1974.

[17] S. Feld, N. Borghini, and C. Lang. Momentum anisotropy at freeze out. *J. Phys. Conf. Ser.*, 832(1):012053, 2017.

[18] Aleksi Kurkela. Some topics in heavy-ion physics, 2016.

[19] F. Debbasch and W. van Leeuwen. General relativistic Boltzmann equation I: Covariant treatment. *Physica A*, 388(7):1079–1104, 2009.

[20] F. Debbasch and W. van Leeuwen. General relativistic Boltzmann equation II: Manifestly covariant treatment. *Physica A*, 388(9):1818–1834, 2009.

[21] Carlo Cercignani and Gilberto Medeiros Kremer. *The relativistic Boltzmann equation*, volume 22 of *Progress in mathematical physics*. Birkhuser, Basel [u.a.], [nachdr.] edition, 2010.

[22] James L. Anderson. Relativistic Boltzmann Theory and the Grad Method of Moments. In *Relativity - Proceedings, Relativity Conference in the Midwest: Cincinnati, USA, June 2-6, 1969*, pages 109–124, 1970.

[23] Luciano Rezzolla and Olindo Zanotti. *Relativistic hydrodynamics*. Oxford Univ. Press, Oxford, 1. ed. edition, 2013.

[24] Ying-Xun Zhang et al. Comparison of heavy-ion transport simulations: Collision integral in a box. *Phys. Rev.*, C97(3):034625, 2018.

[25] Nicolas Borghini and Clément Gombeaud. Anisotropic flow far from equilibrium. *The European Physical Journal C*, 71(4):1612, Apr 2011.

[26] Nicolas Borghini, Steffen Feld, and Nina Kersting. Scaling behavior of anisotropic flow harmonics in the far from equilibrium regime. *Eur. Phys. J.*, C78(10):832, 2018.

[27] Aleksi Kurkela, Urs Achim Wiedemann, and Bin Wu. Nearly isentropic flow at sizeable η/s. *Phys. Lett.*, B783:274–279, 2018.

[28] Aleksi Kurkela, Urs Achim Wiedemann, and Bin Wu. Kinetic transport is needed to reliably extract shear viscosity from pA and AA data. 2018.

[29] Paul Romatschke. Azimuthal Anisotropies at High Momentum from Purely Non-Hydrodynamic Transport. *Eur. Phys. J.*, C78(8):636, 2018.

[30] D. Bazow, G. S. Denicol, U. Heinz, M. Martinez, and J. Noronha. Analytic solution of the Boltzmann equation in an expanding system. *Phys. Rev. Lett.*, 116(2):022301, 2016.

[31] G. S. Denicol, H. Niemi, E. Molnar, and D. H. Rischke. Derivation of transient relativistic fluid dynamics from the Boltzmann equation. *Phys. Rev.*, D85:114047, 2012. [Erratum: Phys. Rev.D91,no.3,039902(2015)].

[32] Paul Romatschke and Michael Strickland. Collective modes of an anisotropic quark gluon plasma. *Phys. Rev.*, D68:036004, 2003.

[33] Lev Davidovi Landau and Evgenij M. Lific. *Hydrodynamik*, volume 6 of *Lehrbuch der theoretischen Physik ; 6*. Akad.-Verl., Berlin, 5., berarb. aufl. edition, 1991.

[34] Sangyong Jeon and Ulrich Heinz. Introduction to Hydrodynamics. *Int. J. Mod. Phys.*, E24(10):1530010, 2015.

[35] Pasi Huovinen. Hydrodynamics at RHIC and LHC: What have we learned? *Int. J. Mod. Phys.*, E22:1330029, 2013.

[36] Carl Eckart. The Thermodynamics of Irreversible Processes. III. Relativistic Theory of the Simple Fluid. *Phys. Rev.*, 58:919–924, Nov 1940.

[37] A. Bazavov et al. Equation of state in (2+1)-flavor QCD. *Phys. Rev.*, D90:094503, 2014.

[38] Paul Romatschke and Ulrike Romatschke. Viscosity Information from Relativistic Nuclear Collisions: How Perfect is the Fluid Observed at RHIC? *Phys. Rev. Lett.*, 99:172301, 2007.

[39] Etele Molnar, Harri Niemi, and Dirk H. Rischke. Closing the equations of motion of anisotropic fluid dynamics by a judicious choice of a moment of the Boltzmann equation. *Phys. Rev.*, D94(12):125003, 2016.

[40] Dennis Bazow, Ulrich W. Heinz, and Michael Strickland. Second-order (2+1)-dimensional anisotropic hydrodynamics. *Phys. Rev.*, C90(5):054910, 2014.

[41] Chun Shen and Bjorn Schenke. Dynamical initial state model for relativistic heavy-ion collisions. *Phys. Rev.*, C97(2):024907, 2018.

[42] Chun Shen and Bjorn Schenke. Dynamical initialization and hydrodynamic modeling of relativistic heavy-ion collisions. 2018.

[43] Lipei Du, Ulrich Heinz, and Gojko Vujanovic. Hybrid model with dynamical sources for heavy-ion collisions at BES energies. 2018.

[44] M. Bleicher et al. Relativistic hadron hadron collisions in the ultrarelativistic quantum molecular dynamics model. *J. Phys.*, G25:1859–1896, 1999.

[45] H. Niemi, E. Molnar, and D. H. Rischke. The right choice of moment for anisotropic fluid dynamics. *Nucl. Phys.*, A967:409–412, 2017.

[46] Wojciech Florkowski, Radoslaw Ryblewski, Michael Strickland, and Leonardo Tinti. Leading-order anisotropic hydrodynamics for systems with massive particles. *Phys. Rev.*, C89(5):054909, 2014.

[47] Tetsufumi Hirano, Pasi Huovinen, Koichi Murase, and Yasushi Nara. Integrated Dynamical Approach to Relativistic Heavy Ion Collisions. *Prog. Part. Nucl. Phys.*, 70:108–158, 2013.

[48] Kang Seog Lee, U. Heinz, and E. Schnedermann. Search for collective transverse flow using particle transverse momentum spectra in relativistic heavy-ion collisions. *Zeitschrift für Physik C Particles and Fields*, 48(3):525–541, Sep 1990.

[49] Philip J. Siemens and John O. Rasmussen. Evidence for a blast wave from compressed nuclear matter. *Phys. Rev. Lett.*, 42:880–883, Apr 1979.

[50] F. Grassi. Particle emission in hydrodynamics: A Problem needing a solution. *Braz. J. Phys.*, 35:52–69, 2005.

[51] D. Oliinychenko, P. Huovinen, and H. Petersen. Cooper-Frye Negative Contributions in a Coarse-Grained Transport Approach. *J. Phys. Conf. Ser.*, 599(1):012017, 2015.

[52] Derek Teaney. The Effects of viscosity on spectra, elliptic flow, and HBT radii. *Phys. Rev.*, C68:034913, 2003.

[53] Shreyasi Acharya et al. Measurement of deuteron spectra and elliptic flow in PbPb collisions at $\sqrt{s_{\rm NN}} = 2.76$ TeV at the LHC. *Eur. Phys. J.*, C77(10):658, 2017.

[54] Jean-Yves Ollitrault. Anisotropy as a signature of transverse collective flow. *Phys. Rev.*, D46:229–245, 1992.

[55] S. Voloshin and Y. Zhang. Flow study in relativistic nuclear collisions by Fourier expansion of Azimuthal particle distributions. *Z. Phys.*, C70:665–672, 1996.

[56] N. Borghini and J. Y. Ollitrault. Azimuthally sensitive correlations in nucleus-nucleus collisions. *Phys. Rev.*, C70:064905, 2004.

[57] Matthew Luzum. Flow fluctuations and long-range correlations: elliptic flow and beyond. *J. Phys.*, G38:124026, 2011.

[58] Ante Bilandzic. Anisotropic flow measured from multi-particle azimuthal correlations for Pb-Pb collisions at 2.76 TeV by ALICE at the LHC. *Nucl. Phys.*, A904-905:515c–518c, 2013.

[59] Jaroslav Adam et al. Anisotropic flow of charged particles in Pb-Pb collisions at $\sqrt{s_{\rm NN}} =$ 5.02 TeV. *Phys. Rev. Lett.*, 116(13):132302, 2016.

[60] H. K. Cheng and R. H. Edwards. Steady expansion of a gas into a vacuum. *AIAA Journal*, 4(3):558–561, 1966.

[61] Gordon Baym. The Physics of Hanbury Brown-Twiss intensity interferometry: From stars to nuclear collisions. *Acta Phys. Polon.*, B29:1839–1884, 1998.

[62] Nicolas Borghini. Momentum conservation and correlation analyses in heavy-ion collisions at ultrarelativistic energies. *Phys. Rev. C*, 75:021904, Feb 2007.

[63] S. Acharya et al. Energy dependence and fluctuations of anisotropic flow in Pb-Pb collisions at $\sqrt{s_{\rm NN}} = 5.02$ and 2.76 TeV. *JHEP*, 07:103, 2018.

[64] J. Scott Moreland, Jonah E. Bernhard, and Steffen A. Bass. Alternative ansatz to wounded nucleon and binary collision scaling in high-energy nuclear collisions. *Phys. Rev.*, C92(1):011901, 2015.

[65] Michael L. Miller, Klaus Reygers, Stephen J. Sanders, and Peter Steinberg. Glauber modeling in high energy nuclear collisions. *Ann. Rev. Nucl. Part. Sci.*, 57:205–243, 2007.

[66] Constantin Loizides, Jason Kamin, and David d'Enterria. Improved Monte Carlo Glauber predictions at present and future nuclear colliders. *Phys. Rev.*, C97(5):054910, 2018.

[67] H. Niemi, G. S. Denicol, H. Holopainen, and P. Huovinen. Event-by-event distributions of azimuthal asymmetries in ultrarelativistic heavy-ion collisions. *Phys. Rev.*, C87(5):054901, 2013.

[68] Shreyasi Acharya et al. Linear and non-linear flow modes in Pb-Pb collisions at $\sqrt{s_{\mathrm{NN}}} =$ 2.76 TeV. *Phys. Lett.*, B773:68–80, 2017.

[69] Li Yan, Jean-Yves Ollitrault, and Arthur M. Poskanzer. Eccentricity distributions in nucleus-nucleus collisions. *Phys. Rev.*, C90(2):024903, 2014.

[70] Li Yan, Jean-Yves Ollitrault, and Arthur M. Poskanzer. Azimuthal Anisotropy Distributions in High-Energy Collisions. *Phys. Lett.*, B742:290–295, 2015.

[71] Hendrik Roch. Monte carlo glauber investigations of the fluctuations in the initial state geometry of high-energy heavy-ion collisions. *Master Thesis*, 2018.